

Université de Montréal

**Effet de la microstructure sur les propriétés excitoniques des  
polymères semi-conducteurs semi-cristallins**

par  
Francis Paquin

Département de Physique  
Faculté des arts et des sciences

Thèse présentée à la Faculté des études supérieures  
en vue de l'obtention du grade de Philosophiæ Doctor (Ph.D.)  
en Faculté des Arts et Sciences

Le 24 janvier, 2014

© Francis Paquin, 2014.

Université de Montréal  
Faculté des études supérieures

Cette thèse intitulée:

**Effet de la microstructure sur les propriétés excitoniques des  
polymères semi-conducteurs semi-cristallins**

présentée par:

Francis Paquin

a été évaluée par un jury composé des personnes suivantes:

Yves Lépine,	président-rapporteur
Carlos Silva,	directeur de recherche
Richard Leonelli,	membre du jury
Greg Scholes,	examinateur externe
Christian Reber,	représentant du doyen de la FES

Thèse acceptée le: .....

## RÉSUMÉ

Les polymères semi-conducteurs semicristallins sont utilisés au sein de diodes électroluminescentes, transistors ou dispositifs photovoltaïques organiques. Ces matériaux peuvent être traités à partir de solutions ou directement à partir de leur état solide et forment des agrégats moléculaires dont la morphologie dicte en grande partie leurs propriétés optoélectroniques. Le poly(3-hexylthiophène) est un des polymères semi-conducteurs les plus étudiés. Lorsque le poids moléculaire ( $M_w$ ) des chaînes est inférieur à 50 kg/mol, la microstructure est polycristalline et composée de chaînes formant des empilements- $\pi$ . Lorsque  $M_w > 50$  kg/mol, la morphologie est semicristalline et composée de domaines cristallins imbriqués dans une matrice de chaînes amorphes.

À partir de techniques de spectroscopie en continu et ultrarapide et appuyé de modèles théoriques, nous démontrons que la cohérence spatiale des excitons dans ce matériau est légèrement anisotrope et dépend de  $M_w$ . Ceci nous permet d'approfondir la compréhension de la relation intime entre le couplage inter et intramoléculaire sur la forme spectrale en absorption et photoluminescence. De plus, nous démontrons que les excitations photogénérées directement aux interfaces entre les domaines cristallins et les régions amorphes génèrent des paires de polarons liés qui se recombinent par effet tunnel sur des échelles de temps supérieures à 10 ns. Le taux de photoluminescence à long temps de vie provenant de ces paires de charges dépend aussi de  $M_w$  et varie entre  $\sim 10\%$  et  $\sim 40\%$  pour les faibles et hauts poids moléculaires respectivement. Nous fournissons un modèle permettant d'expliquer le processus de photogénération des paires de polarons et nous éludions le rôle de la microstructure sur la dynamique de séparation et recombinaison de ces espèces.

**Mots-clés :** polymères semi-conducteurs, dynamique d'excitons, microstructure, séparation de charge, agrégats H et J.



## ABSTRACT

Microstructure plays a crucial role in defining the optoelectrical properties of conjugated polymeric semiconductors which can be used in light harvesting and generating devices such as organic light emitting diodes, field effect transistors or photovoltaic devices. These polymers can be processed from solution or solid-state and form photophysical aggregates, consequently providing a complex network which controls the fate of any photogenerated species. poly(3-hexylthiopene) is one of the most studied polymeric semiconductor. In this material, the molecular weight ( $M_w$ ) of the polymer governs the microstructure and highly impact the optical and electronic properties. Below  $M_w \approx 50$  kg/mol, the polymer chains forms polycrystalline domains of  $\pi$ -stacked molecules while high  $M_w$  ( $>50$  kg/mol) consists of a two-phase morphology of molecularly ordered crystallites that are embedded in amorphous regions. Such morphology provides a bidimensionnal network hosting both neutral excitations, known as Frenkel excitons, and polarons.

By means of steady-state and ultrafast spectroscopy experiment and backed up theoretical modeling, we demonstrate that the spatial coherence of such excitations are anisotropic in the lattice and depends on the  $M_w$  of the polymer, providing a deep understanding of the interplay between interchain (excitonic) and intrachain coupling in polymer aggregates. Moreover, we show that direct excitation at the interface between molecularly ordered and amorphous regions generates tightly-bound charge pairs which decay via quantum tunneling over  $>10$  ns. The yield of delayed photoluminescence arising from the recombination of those charge pairs varies between  $\sim 10\%$  and  $\sim 40\%$  for low and high  $M_w$  films respectively. We provide a quantitative model that describes the photogeneration process of those geminate polaron pairs and determine the role of the microstructure in the charge separation and recombination processes.

**Keywords:** semiconducting polymers, exciton dynamics, solid-state

microstructure, charge separation, H and J aggregates.



## TABLE DES MATIÈRES

RÉSUMÉ . . . . .	iii
ABSTRACT . . . . .	v
TABLE DES MATIÈRES . . . . .	viii
LISTE DES TABLEAUX . . . . .	xiv
LISTE DES FIGURES . . . . .	xvi
LISTE DES ANNEXES . . . . .	xix
LISTE DES SIGLES . . . . .	xxi
DÉDICACE . . . . .	xxiii
REMERCIEMENTS . . . . .	xxv
<b>CHAPITRE 1 : INTRODUCTION . . . . .</b>	<b>1</b>
1.1 Mise en contexte . . . . .	1
1.1.1 Morphologie du rr-P3HT . . . . .	2
1.2 De l'oligomère au polymère de haute masse molaire . . . . .	4
1.3 Influence de la microstructure sur les propriétés optoélectroniques .	5
1.4 Nos objectifs . . . . .	7
1.5 Format de ce document . . . . .	9
<b>CHAPITRE 2 : CADRE THÉORIQUE . . . . .</b>	<b>12</b>
2.1 Propriétés des matériaux $\pi$ -conjugués . . . . .	12
2.2 Procédés optiques dans les matériaux organiques . . . . .	14
2.2.1 Perturbation optique d'un système . . . . .	14

2.2.2	L'approximation de Born-Oppenheimer . . . . .	15
2.2.3	Influence du couplage électrons-phonons sur la forme spectrale en photoluminescence . . . . .	16
2.2.4	Transitions optiques radiatives et non radiatives . . . . .	20
2.2.5	Excitons singulets et triplets . . . . .	23
2.3	Excitons dans des agrégats moléculaires . . . . .	24
2.3.1	Largeur de bande de l'exciton . . . . .	26
2.4	Interactions dans les agrégats moléculaires . . . . .	28
2.4.1	Interactions dipôle-dipôle : Agrégats de type H et J . . . . .	28
2.4.2	Propriétés optiques des agrégats de types H et J . . . . .	30
2.4.3	Comportement hybride des agrégats HJ . . . . .	33
2.5	Introduction aux excitons polaroniques . . . . .	33
2.6	Excitations intrachaine . . . . .	37
2.7	Les paires de polarons . . . . .	38

**CHAPITRE 3 : TWO-DIMENSIONAL SPATIAL COHERENCE OF  
EXCITONS IN SEMICRYSTALLINE POLYMERIC  
SEMICONDUCTORS : EFFECT OF MOLECULAR  
WEIGHT . . . . .** 40

3.1	Contexte de l'article . . . . .	40
3.1.1	Sonde spectroscopique ultrarapide et en continu . . . . .	42
3.2	Contribution originale de chaque coauteurs . . . . .	43
3.3	Abstract . . . . .	45
3.4	Introduction . . . . .	47
3.5	Experimental Methods . . . . .	51
3.6	Results and Analysis . . . . .	52
3.6.1	Relationship between exciton signatures and solid-state microstructure . . . . .	52

3.6.2	The HJ-aggregate model . . . . .	61
3.6.3	Exciton coherence . . . . .	72
3.7	Discussion . . . . .	80
3.8	Conclusion . . . . .	82

**CHAPITRE 4 : CHARGE SEPARATION IN SEMICRYSTALLINE  
POLYMERIC SEMICONDUCTORS BY PHOTOEX-  
CITATION : IS THE MECHANISM INTRINSIC  
OR EXTRINSIC ? . . . . .** 85

4.1	Contexte de l'article . . . . .	85
4.2	Techniques de photoluminescence résolue en temps . . . . .	87
4.3	Contribution originale de chaque coauteurs . . . . .	88
4.4	Abstract . . . . .	90
4.5	Introduction . . . . .	91
4.6	Experimental Methods . . . . .	92
4.7	Results and Discussion . . . . .	92

**CHAPITRE 5 : MULTI-PHASE SEMICRYSTALLINE MICROSTRUC-  
TURES DRIVE EXCITON DISSOCIATION IN NEAT  
PLASTIC SEMICONDUCTORS . . . . .** 100

5.1	Contexte de l'article . . . . .	100
5.2	Contribution originale de chaque coauteurs . . . . .	100
5.3	Abstract . . . . .	102
5.4	Introduction . . . . .	103
5.5	Results and analysis . . . . .	104
5.6	Discussion . . . . .	112
5.7	Conclusions . . . . .	117
5.8	Experimental Methods . . . . .	117
5.8.1	Polymer processing . . . . .	117

5.8.2	Photoluminescence spectroscopy . . . . .	118
5.8.3	Wide-angle X-ray scattering . . . . .	118
<b>CHAPITRE 6 : INFLUENCE OF MICROSTRUCTURE ON GE- MINATE POLARON SPATIAL DISTRIBUTION IN SEMICRYSTALLINE POLYMERIC SEMICONDUC- TORS . . . . .</b>		<b>121</b>
6.1	Contexte de l'article . . . . .	121
6.2	Contribution originale de chaque coauteurs . . . . .	121
6.3	Abstract . . . . .	124
6.4	Introduction . . . . .	125
6.5	Results . . . . .	127
6.5.1	Absorption . . . . .	127
6.5.2	Steady-state photoinduced absorption . . . . .	128
6.5.3	Transient-absorption spectroscopy . . . . .	130
6.6	Discussion . . . . .	132
6.7	Conclusion . . . . .	135
6.8	Experimental Methods . . . . .	135
6.8.1	Polymer processing . . . . .	135
6.8.2	Absorption measurement . . . . .	136
6.8.3	Photoinduced absorption measurement . . . . .	136
6.8.4	Transient absorption measurement . . . . .	136
<b>CHAPITRE 7 : CONCLUSION . . . . .</b>		<b>138</b>
<b>BIBLIOGRAPHIE . . . . .</b>		<b>144</b>
I.1	Determination of $W$ for arbitrary Huang-Rhys parameter obtained from the PL spectrum . . . . .	xxvii
I.2	Huang-Rhys parameter of a single thiophene unit . . . . .	xxviii

II.1	Absorption and photoluminescence spectra . . . . .	xxxii
II.2	Time-resolved PL dynamics . . . . .	xxxiii
II.2.1	Fluence dependence . . . . .	xxxiii
II.2.2	Temperature dependence . . . . .	xxxiii
II.2.3	Delayed PL spectral bandshape . . . . .	xxxiv
II.3	Phase-sensitive photomodulation . . . . .	xxxv
II.4	Transient absorption Dynamics . . . . .	xxxvii
II.4.1	Comparison of TA and PL dynamics . . . . .	xxxviii
III.1	Continuous-wave photoinduced absorption spectroscopy . . . . .	xli
IV.1	Articles publiés . . . . .	xliii
IV.2	Autres . . . . .	xliv
IV.3	Articles soumis ou en préparation . . . . .	xliv



## LISTE DES TABLEAUX

3.I	Values of $\beta$ and $ J_{\text{intra}} $ (eV) from fig.3.5 along with values of $ J_{\text{inter}} $ (eV) which maintain the 0-0/0-1 PL ratio at 0.56 in films of high- $M_w$ P3HT and 0.30 in low- $M_w$ films. . . . .	70
I.I	B3LYP-EXX50 . . . . .	xxx
I.II	B3LYP . . . . .	xxx



## LISTE DES FIGURES

1.1	Schématisation de l'arrangement supramoléculaire du P3HT cristallin	3
1.2	Schématisation de la microstructure à l'état solide du P3HT de faible et haut poids moléculaire . . . . .	4
1.3	Mobilité de charge dans des transistors à effet de champ de P3HT, en fonction du poids moléculaire du matériau . . . . .	6
1.4	Mobilité de charge observée par spectroscopie par temps de vol pour des films de P3HT. . . . .	7
2.1	Phénomène d'hybridation et conjugaison de la molécule de benzène	12
2.2	Représentation schématique d'une transition vibronique dans une molécule . . . . .	17
2.3	Influence du paramètre Huang-Rhys sur la forme de la photoluminescence d'une molécule isolée . . . . .	19
2.4	Représentation schématique des transitions électroniques possibles dans une molécule . . . . .	22
2.5	Illustration schématique de l'étendue spatiale des excitons de type Wannier-Mott et Frenkel dans un cristal . . . . .	24
2.6	Schématisation de l'effet du couplage intermoléculaire sur les niveaux énergétiques . . . . .	28
2.7	Effet de l'interaction dipôle-dipôle sur les niveaux énergétiques d'un dimère . . . . .	29
2.8	Orientation moléculaire et relation de dispersion dans les agrégats H, J et HJ. . . . .	31
2.9	Illustration schématique de la distorsion d'un cristal générée par un exciton de Frenkel polaronique. . . . .	34
2.10	Excitations fondamentales dans les structures supramoléculaires. . .	35

3.1	Absorption and photoluminescence spectra in thin films of neat P3HT of low and high molecular weight. . . . .	53
3.2	Free-exciton bandwidth, 0–0 Intensity in PL, Huang-Rhys parameter, Melting temperature and enthalpy of fusion as a function of molecular weight. . . . .	55
3.3	Time-resolved photoluminescence up-conversion measurements at room temperature. . . . .	60
3.4	Calculated effective Huang-Rhys parameter as a function of intra- molecular and intermolecular coupling. . . . .	66
3.5	Intramolecular coupling values for high and low molecular weight fims as a function of the correlated disorder parameter, $\beta$ . . . . .	68
3.6	Calculated PL spectra for materials of molecular weights in the low and high $M_w$ limits . . . . .	69
3.7	The 0-0/0-1 PL ratio as a function of temperature for both high and low molecular weight films. . . . .	72
3.8	Coherence function for low- and high- $M_w$ samples. . . . .	74
3.9	Coherence size defined in as a function of disorder parameter, $\beta$ . . .	77
4.1	Time-resolved PL spectrum and anisotropy at T=10 K. . . . .	93
4.2	Quantum molecular dynamic snapshot of an aggregate architecture, Average site excitation energy, Absorption spectrum for one config- uration of the full stack superimposed to the corresponding CT character and Transition densities for excitations of increasing energy.	98
5.1	Schematic of different solid-state microstructures adopted by the films of low and high molecular weight. . . . .	105
5.2	Prompt and delayed spectra of the time-gated photoluminescence for solution and solid-state-processed films of different molecular weight.	106

5.3	Time-resolved photoluminescence intensity measured at 10 K for films of different molecular weight and processing. . . . .	108
5.4	Power-law decay parameter $\mu$ and delayed PL relative intensity versus $M_w$ . . . . .	110
6.1	Room temperature absorption spectra of thin films of neat P3HT for different molecular weight. . . . .	127
6.2	Quasi-steady-state photoinduced absorption spectra at T=10 K in thin films of neat P3HT of different molecular weight . . . . .	129
6.3	Transient absorption spectrum of neat P3HT of $M_w=48$ kg/mol measured at T=10 K . . . . .	131
I.1	Free-exciton bandwidth, $W$ , extracted from the absorption spectrum using $\lambda^2 = 1$ (red squares) and arbitrary $\lambda^2$ obtained from the PL spectra (blue circles) as a function of molecular weight. . . . .	xxviii
II.1	Absorption (room-temperature) and PL (10 K) spectra of P3HT. . .	xxxi
II.2	Spectrally integrated PL intensity as a function of time following excitation at 2.33 eV, at two different fluences . . . . .	xxxiii
II.3	Time-resolved PL intensity following 2.33-eV photoexcitation at two temperatures . . . . .	xxxiv
II.4	PL spectra at two temporal gates . . . . .	xxxv
II.5	PL spectrum measured at 10 K by phase-sensitive detection upon modulated excitation at 2.33 eV. . . . .	xxxvi
II.6	Transient absorption spectrum measured at 10 K . . . . .	xxxvii
II.7	Comparison of the photoinduced absorption signal probing at 1.88 eV, derived from the spectrum in Fig. II.6(a), and the time-resolved PL data at lower fluence shown in Fig. II.2(a). . . . .	xxxviii



## LISTE DES ANNEXES

Annexe I :	Two-dimensional spatial coherence of excitons in semicrystalline polymeric semiconductors : The effect of molecular weight . . . . .	xxvii
Annexe II :	Charge separation by photoexcitation in semicrystalline polymeric semiconductors : An intrinsic or extrinsic mechanism ? . . . . .	xxxii
Annexe III :	Influence of microstructure on geminate polaron spatial distribution in semicrystalline polymeric semiconductors. . . . .	xli
Annexe IV :	Articles publiés ou en attente de publication . . .	xliii



## LISTE DES SIGLES

DSC	Differential Scanning Calorimetry
EQE	Efficacité Quantique Externe
eV	Électron-Volt
HOMO	Highest Occupied Molecular Orbital
HR	Huang-Rhys
LUMO	Lowest Unoccupied Molecular Orbital
P3HT	poly(3-hexylthiophène)
PIA	Photoinduced Absorption
PL	Photoluminescence
TA	Transient Absorption
UV	Ultraviolet
<i>W</i>	Largeur de bande de l'exciton



À mes parents, Nicole et Guy.



## REMERCIEMENTS

En tout premier lieu, j'aimerais remercier mon directeur de recherche Carlos Silva pour m'avoir pris sous son aile et avoir eu confiance en moi durant toutes ces années. Non seulement tu as été un directeur de recherche hors pair, mais tu as aussi été un ami et un confident. Je n'oublierai jamais les conversations au bureau, au pub ou lors de notre séjour à Londres. Merci de m'avoir aidé aussi dans les moments les plus difficiles.

J'aimerais aussi remercier tous les membres de mon groupe de recherche présents et passés pour les moments de folies spontanées qui ont souvent allégé l'ambiance du bureau et du laboratoire. Sans ordre d'importance : Simon Gélinas, Paul-Ludovic Karsenti, Collin Nadeau Brosseau, Houssem Kallel, Carine Bertelli Cardoso, Mathieu Robert, Françoise Provencher, Benoit Gosselin, Elham Soltani, Laura-Isabelle Dion Bertrand, Olivier Paré-Labrosse, Eleonora Vella, Pascal Grégoire, Félix Thouin ainsi que ceux qui font en quelque sorte parti de notre groupe : T-Hawk (Charles Alexandre Désilets-Benoit) et Guillaume Gélinas. Un énorme merci à Natalie Stingelin pour m'avoir invité à travailler dans son laboratoire à Imperial College et aux membres exceptionnels de son groupe : Christoph Hellmann, Paul Westacott, Ester Butxaca Domingo, Emanuella, Alberto Davide Scaccabarozzi et tous les autres que j'oublie. Merci à nos techniciens qui rendent certaines tâches beaucoup moins lourdes : Robert Rinfret, Jean-Sébastien Mayer. Un gros merci à mes parents pour leur support moral constant. Finalement, merci à ma copine Carole pour ta présence durant toutes ces années. Merci pour ton appui constant, pour avoir partagé les plus beaux moments et ceux qui ont été difficiles.



# CHAPITRE 1

## INTRODUCTION

### 1.1 Mise en contexte

La découverte des polymères ayant des propriétés semi-conductrices a fait l'objet d'une révolution scientifique à la fin des années 1970 et a notamment valu le prix Nobel de chimie à Allan Heeger, Alan MacDiarmid et Hideki Shirakawa en octobre 2000. [1] Ces matériaux organiques offrent certains avantages comparativement aux matériaux inorganiques : ils ont un coût relativement faible de production et ce sont des matériaux polyvalents qui démontrent une flexibilité au niveau de leur fabrication et leur traitement. Leur utilisation au sein de dispositifs optoélectroniques est multiple : diodes électroluminescentes [2–6], transistors [7, 8] ou encore cellules solaires organiques. [9–11] De plus, ils ont fait leur entrée dans la charte des meilleurs dispositifs photovoltaïques répertoriés par le "National Renewable Energy Laboratory" (NREL) au début du millénaire. [12] Au moment de l'écriture de cette thèse, l'efficacité de conversion de puissance énergétique des meilleures cellules solaires organiques recensées par le NREL se situe aux alentours de  $\eta \sim 11\%$  [12]. Bien que ce taux est en croissance perpétuelle depuis les 10 dernières années, leur efficacité n'arrive pas à la moitié de ce qui est standard pour les cellules conventionnelles à base de silicium cristallin où  $\eta \sim 25\%$  [12]. Cet écart subsiste en partie par le fait qu'il existe toujours une incompréhension sur la relation entre la microstructure des polymères semi-conducteurs semi-cristallins et certaines de leurs propriétés optoélectroniques.

Dans ce type de matériau, les excitations primaires générées suite à l'absorption de photons jouent un rôle fondamental dans tout processus optique. En effet, l'interaction des polymères semi-conducteurs avec une radiation optique permet

de créer initialement des paires électrons-trous liées par une force coulombienne. Ces quasi-particules appelées excitons (onde d'excitation) peuvent se recombiner radiativement, donnant lieu à la photoluminescence. Ce processus est à la base des diodes électroluminescentes, suite à l'injection d'électrons et trous dans le matériau. En contre-partie, l'efficacité de leur dissociation en paires électron-trou libres limite les performances des dispositifs photovoltaïques où l'on tente d'en tirer un courant électrique. Ainsi, l'analyse du comportement intrinsèque de cette quasi-particule est fondamentale à la compréhension et l'amélioration des propriétés optoélectroniques des matériaux et dispositifs dans lesquels ils sont utilisés.

Dans cette thèse, nous utilisons des expériences à sondes optiques et structurales qui nous permettent d'étudier l'évolution temporelle du comportement des excitons, de cibler leur caractère intrinsèque et d'établir une relation entre la microstructure et les propriétés optoélectroniques dans des films de polymères semi-conducteurs. Nous varions la morphologie de ces films en modifiant le poids moléculaire ainsi que les procédés de fabrication. Notre contribution principale aux connaissances du milieu scientifique actuel est d'étendre la compréhension de la dépendance complexe entre la forme spectrale en absorption et photoluminescence et le couplage excitonique inter et intramoléculaire dans les agrégats de polymères. De plus, nous détaillons la dynamique de formation et recombinaison des paires de polarons qui sont responsables du taux significatif de charges présent dans ce type de matériau. Nos résultats permettent de cibler l'importance de l'agencement des chaînes de polymères sur la formation de ces paires de charges.

### 1.1.1 Morphologie du rr-P3HT

Les polymères semi-conducteurs peuvent former des arrangements supramoléculaires complexes caractérisés par une stabilité qui est limitée par les forces non covalentes de van der Waals, de Coulomb, des interactions  $\pi-\pi$  et des liaisons hydrogènes. Lorsqu'ils forment des couches minces de l'ordre de la centaine de nano-

mètres, leur degré de cristallisation dépend d'une multitude de paramètres (solvant, masse molaire, température, etc.) à tel point qu'à ce jour il est très difficile, voire impossible, pour les chimistes qui font la synthèse de nouveaux matériaux de prévoir leur morphologie à l'état solide.

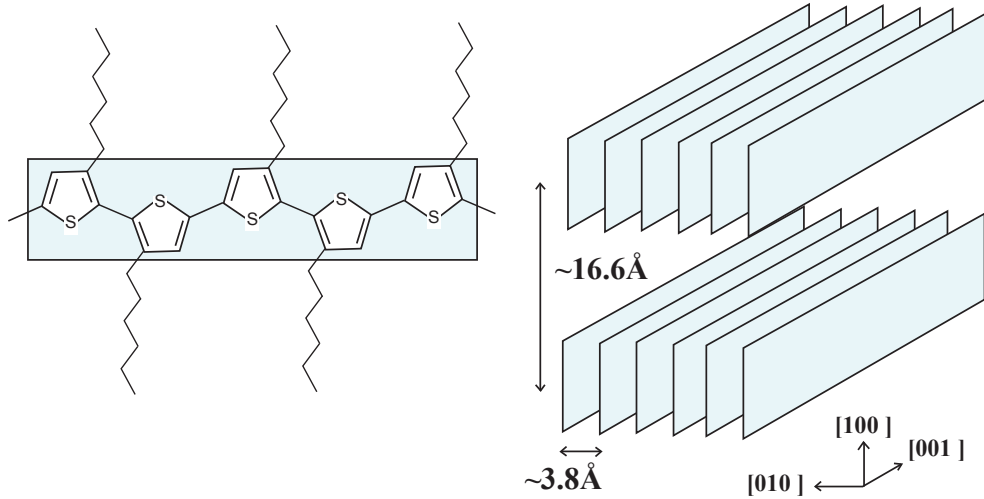


Figure 1.1 – Arrangement supramoléculaire du rr-P3HT. Les chaînes s’empilent de façon cofaciale, provoquant un chevauchement des orbitales- $\pi$  responsables de la délocalisation des électrons dans le matériau.

Un des polymères semi-conducteurs les plus étudiés est le poly(3-hexylthiophène), communément appelé P3HT. Il est constitué d'une chaîne de polythiophène  $\pi$ -conjuguée formant le squelette de la molécule à laquelle sont attachées des chaînes latérales (groupements hexyl) qui assurent la solubilité du matériau. L'incompatibilité entre le squelette et les chaînes latérales fait en sorte que ce matériau s'auto-assemble en une structure complexe. En effet, lorsque déposées sur un substrat à partir d'une solution dans laquelle les chaînes de polymère sont dispersées, les molécules s'agglomèrent pour former des domaines microcristallins caractérisés par un *empilement- $\pi$*  des chaînes. [13, 14] Ce type d'empilement dont la signature caractéristique peut être obtenue par spectroscopie par rayons-X est représenté à la Fig.1.1. Les chaînes de polymère se superposent de façon cofaciale, permettant ainsi aux orbitales  $p$  (orientées dans la direction [010]) des molécules avoisinantes de se

chevaucher partiellement. C'est ce type d'arrangement moléculaire qui permet la formation du réseau bidimensionnel dans lequel peuvent se mouvoir les espèces photogénérées suite à l'absorption de photons (excitons, polarons). Ces empilements de chaînes sont caractérisés par une distance intermoléculaire de  $\sim 3.8 \text{ \AA}$  contrairement à la distance entre les agrégats qui est de  $\sim 16.6 \text{ \AA}$ , en conséquence de la présence des longues chaînes latérales. Ainsi, la courte distance interchaîne permet un couplage intermoléculaire significatif dans la direction [010], tandis que les interactions inter agrégats sont négligeables. [7, 15] La taille des lamelles de P3HT dans la direction [010] peut avoisiner les 7-8 nm, dépendamment du poids moléculaire et des méthodes de fabrication. [16, 17]

## 1.2 De l'oligomère au polymère de haute masse molaire

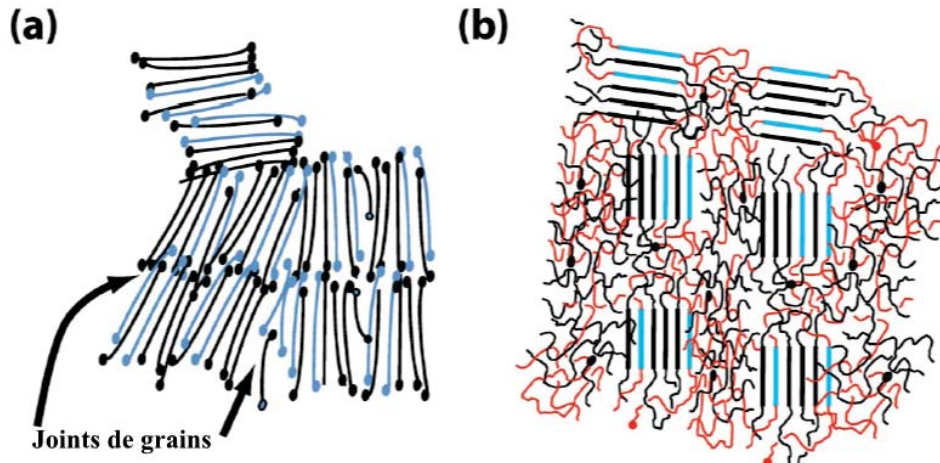


Figure 1.2 – Microstructure à l'état solide du P3HT de faible (a) et haut (b) poids moléculaires. Les chaînes de P3HT de faible poids moléculaire ( $M_w < 50 \text{ kg/mol}$ ) forment une microstructure polycristalline caractérisée par des chaînes étendues, tandis que les films formés avec  $M_w > 50 \text{ kg/mol}$  sont plutôt semi-cristallins, i.e composés de domaines cristallins entourés de régions amorphes. Ces dernières comprennent un amas de chaînes intermêlées. (Image tirée de la Réf. [18])

Dans cette thèse, nous nous intéressons majoritairement à l'influence du poids moléculaire des polymères semi-conducteurs semi-cristallins sur la microstructure

et sur les propriétés optiques dans des films minces de P3HT. Il est connu que les petites molécules comportant quelques unités monomériques (oligomères) forment des cristaux dans lesquels les chaînes sont étendues (droites), avec une longueur de conjugaison fondamentalement plus faible que dans les matériaux de plus haut poids moléculaire. [19] À la Fig.1.2(a), les régions cristallines sont alors délimitées par des frontières granuleuses. Les films produits avec des polymères de plus haut poids moléculaire ont une microstructure qui s'apparente aux plastiques, formés d'agrégats dont les chaînes sont plus flexibles et planaires . [19–21] Tel que schématisé à la Fig.1.2(b), dans la limite de haut poids moléculaire, la microstructure est composée de lamelles cristallines intercalées par des régions amorphes composées de chaînes désordonnées et intermêlées. Les longues chaînes de polymères peuvent alors servir à lier les domaines cristallins, augmentant par le fait même de façon significative les performances mécaniques ainsi que la percolation des charges entre les agrégats. [19, 22] Dans cette limite, le matériau est beaucoup plus robuste, fiable et stable chimiquement. Ce sont des caractéristiques que l'on tente continuellement d'optimiser dans le domaine de l'électronique plastique.

### 1.3 Influence de la microstructure sur les propriétés optoélectroniques

Dans les films de P3HT, la mobilité de charge la plus élevée répertoriée avoisine les  $0.1 \text{ cm}^2\text{V}^{-1}\text{s}^{-1}$  [7, 23], s'approchant de la mobilité des charges dans le  $\alpha$ -Si. De plus, lorsque mélangé avec le [6,6]-phényl-C61-butanoate de méthyle (un semi-conducteur organique dérivé du fullerène, aussi connu sous le nom de PCBM), l'efficacité typique est de 5% [24] et la maximale jamais recensée de 6.5%. [25, 26] Il est alors un candidat de prédilection pour les dispositifs optoélectroniques organiques. Cependant, ces valeurs dépendent largement de la morphologie du matériau. Par exemple, pour du RRa-P3HT<sup>1</sup>, le fort désordre configurationnel abaisse la mobilité

---

<sup>1</sup>P3HT régioaléatoire : faible % de la répétition de la conformation tête-à-queue des unités de thiophène le long de la molécule.

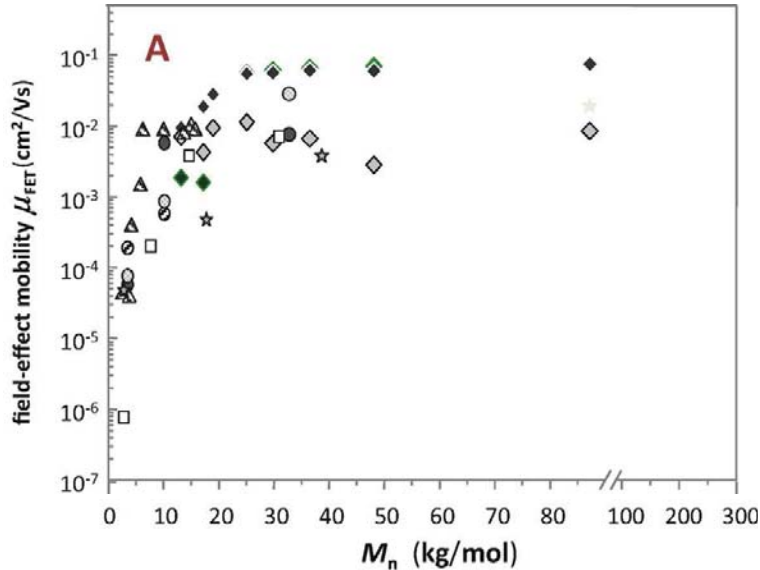


Figure 1.3 – Mobilité de charge dans des transistors à effet de champ de P3HT, en fonction du poid moléculaire du matériau. Les données sont cumulatives des travaux de plusieurs groupes. (Image tirée de la Réf. [19])

des charges à  $\sim 10^{-5} \text{ cm}^2\text{V}^{-1}\text{s}^{-1}$ , [7] soit 6 ordres de grandeur plus faible que le rr-P3HT et caractéristique des polymères désordonnés. [22]

Un autre comportement important est relié à la masse molaire des molécules, qui elle aussi influence aussi largement les propriétés mécaniques et électroniques. Spécifiquement, les résultats de la Fig.1.3 tirés de la Réf. [19] démontrent que la mobilité des charges dans des transistors à effet de champ à base de P3HT dépend de la microstructure conférée par le poids moléculaire du matériau et augmente jusqu'à environ 40 kg/mol où ces valeurs plafonnent ensuite pour les poids moléculaires plus élevés. [19, 27–31]. Pour ce qui est des mobilités de charge dans le volume du matériau, le comportement est plus complexe. La Fig.1.4 montre les résultats de spectroscopie par temps de vol de la réf. [19]. Les résultats affichent une mobilité volumique plus faible à haut poids moléculaire, et un maximum à environ 5 kg/mol. [19, 32] Cependant, ces mobilités volumiques diffèrent entre certaines études et il est difficile de réconcilier la disparité entre les valeurs publiées en raison

des procédés de fabrication qui diffèrent largement d'un groupe à un autre. Néanmoins, il est clair que la microstructure conférée par la masse molaire du matériau a un impact majeur sur les propriétés optoélectroniques et c'est sur cet aspect que sont basés les travaux de cette thèse.

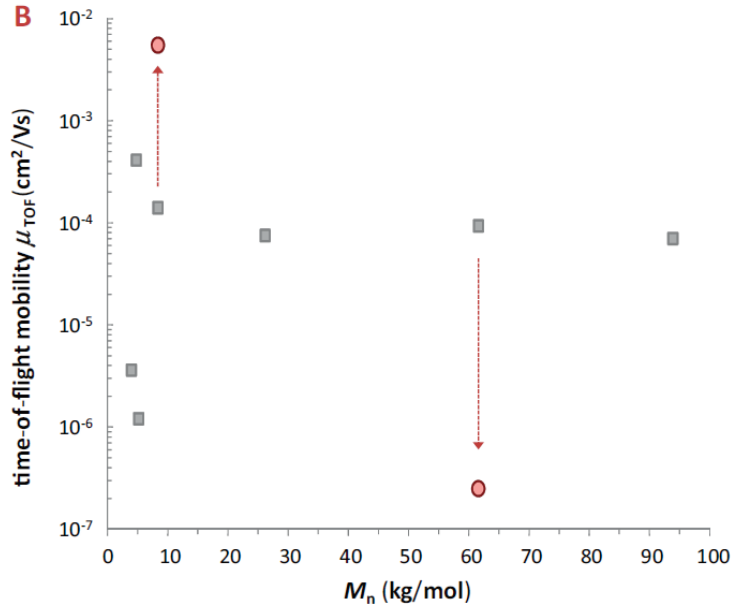


Figure 1.4 – Mobilité de charge observée par spectroscopie par temps de vol pour des films de P3HT déposés à partir d'une solution à température pièce (carrés) et à  $T=115^\circ\text{C}$  (cercles). (Image tirée de la Réf. [19])

## 1.4 Nos objectifs

Les objectifs principaux de cette thèse sont d'acquérir une compréhension détaillée des propriétés des excitons dans les polymères semi-conducteurs semi-cristallins. Plus spécifiquement, nous nous penchons sur l'influence de la microstructure qu'engendre une variation du poids moléculaire du P3HT sur les propriétés excitoniques dans des films minces. Via une multitude de techniques spectroscopiques et de sondes structurelles qui seront décrites dans le corps de ce document, nous explorons la dynamique des excitations primaires et leur évolution temporelle sur des échelles

de temps allant de quelques femtosecondes jusqu'à la microseconde. Sans dispositif pour récolter les charges créées, toute excitation photogénérée doit ultimement revenir à l'état fondamental via une relaxation radiative ou non radiative, avec une signature caractéristique de la microstructure. Le couplage excitonique résultant de l'agrégation de molécules tel que schématisé à la Fig.1.1 prône la délocalisation de la fonction d'onde des excitons dans les domaines cristallins. Cependant, cette délocalisation est concurrente avec la nature localisatrice du désordre énergétique inhérent dans les polymères et du couplage entre les électrons et les modes de vibration du réseau. Avec nos mesures spectroscopiques et en nous appuyant sur un modèle théorique qui tient compte des interactions excitoniques le long de la chaîne, entre les chaînes, du couplage électron-phonons et du désordre énergétique, nous élucidons l'influence de la microstructure sur la cohérence spatiale bidimensionnelle des excitons dans cette classe de matériau.

De plus, nous nous penchons aussi sur le processus de séparation de ces excitons, dont le mécanisme exact fait toujours objet de vifs débats scientifiques. Lorsque séparés spatialement sur deux molécules, les excitons forment des paires de polarons (électron ou trou habillés du champ de polarisation dans le réseau). La formation de ces derniers a été observée sur des échelles de temps ultrarapides ( $\sim 150$  fs). [33–35] Les expériences que nous avons développées nous permettent de sonder le mécanisme de dissociation des excitons en paires de polarons ainsi que leur recombinaison radiative successive et nous permettent de décrire la morphologie des sites où le processus prend naissance. Nous démontrons ainsi que la photogénération de polarons se produit dans des domaines morphologiquement plus désordonnés, et spéculons que ces régions sont caractéristiques des interfaces entre les domaines cristallins et les régions amorphes. Ce type d'étude est central à la compréhension exhaustive de la relation entre la morphologie et les propriétés optoélectroniques dans cette vaste classe de matériau.

## 1.5 Format de ce document

La partie centrale de cette thèse est constituée de 4 articles scientifiques. L'information supplémentaire de chaque article, lorsque de mise, est fournie en annexe. La contribution de chaque coauteur à la forme finale des articles est aussi incluse en annexe.

Le premier chapitre expose les caractéristiques principales des matériaux  $\pi$ -conjugués, les principes physiques d'interaction entre la lumière et la matière ainsi que les propriétés reliées à l'agrégation de molécules.

Le second chapitre porte sur la cohérence spatiale des excitons dans les agrégats de P3HT. Nous démontrons que cette cohérence est bidimensionnelle, anisotrope et dépend du poids moléculaire du polymère. Ce chapitre sert à faire le pont entre la théorie des excitations dans les agrégats moléculaires désordonnés et les observations expérimentales par spectroscopie d'absorption et de photoluminescence.

Le troisième chapitre traite du mécanisme de séparation d'excitons en paires géminales de polarons dans les agrégats moléculaires en s'appuyant sur des méthodes de spectroscopie ultrarapides. Nous appliquons aussi un modèle théorique à multi niveaux pour expliquer l'origine de la photoluminescence à court et à long temps de vie. Ces mesures nous permettent de conclure que la séparation se produit aux interfaces entre les domaines cristallins et les régions amorphes.

Le quatrième chapitre fait un suivi des résultats du chapitre 3. Nous étalons ainsi notre recherche sur le mécanisme de séparation de charge pour différents types de microstructures. Dans ce chapitre, nous démontrons que le taux de formation, recombinaison ainsi que la distance moyenne des paires de charges dépend largement du procédé de fabrication et du poids moléculaire.

Le cinquième chapitre porte sur l'origine de la formation des paires de charges dans les films de différents poids moléculaires et permet une conclusion descriptive de la morphologie des sites qui accueillent ces espèces.

Finalement, une conclusion générale des travaux de cette thèse permet de mettre en perspective les résultats obtenus avec la vision globale du milieu scientifique sur le sujet présenté dans le corps de ce document.



## CHAPITRE 2

### CADRE THÉORIQUE

#### 2.1 Propriétés des matériaux $\pi$ -conjugués

Les polymères semi-conducteurs utilisés dans le domaine de l'optoélectronique sont majoritairement composés de carbone, une des briques essentielles des matériaux organiques. Le carbone porte la configuration électronique  $1s^22s^22p^2$  dans son état fondamental. Des quatre électrons de valences, les deux électrons  $s$  forment une paire sur une même orbitale moléculaire tandis que les deux électrons  $p$  sont positionnés sur des orbitales différentes. Certaines structures moléculaires forcent les orbitales  $s$  et  $p$  à se combiner pour former des orbitales hybrides. Ces orbitales hybrides ont une orientation spatiale et des énergies qui diffèrent largement des orbitales non hybridées.

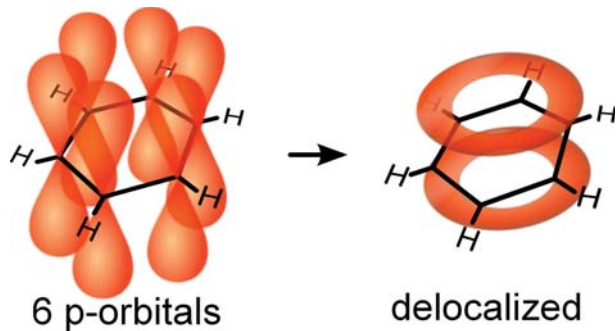


Figure 2.1 – Illustration du phénomène d'hybridation  $sp^2$  du benzène. Les électrons- $\pi$  sont délocalisés sur la molécule.

Par exemple, la molécule de benzène ( $C_6H_6$ ) est formée par hybridation de type  $sp^2$ . En effet, il est possible d'obtenir un mélange des deux orbitales  $s$  et deux orbitales  $p$  de sorte à former trois orbitales  $sp^2$ , tout en laissant une orbitale  $p$  inchangée. Dans ce cas, les trois orbitales  $sp^2$  sont coplanaires et dirigées à  $120^\circ$  les unes par rapport aux autres et servent à former les liens  $\sigma$  tandis que l'orbitale  $p$

restante se trouve perpendiculaire aux orbitales  $sp^2$  et sert à former des liens  $\pi$  avec les orbitales  $p$  avoisinantes. Une conséquence fondamentale de ce type d'hybridation est que la densité électronique des électrons occupant les orbitales  $\sigma$  est fortement localisée dans l'espace entre les atomes de carbone et ces derniers ne contribuent pas à la conductivité de tels types de matériau puisque leur énergie d'ionisation est très élevée ( $\sim 11\text{eV}$ ). [36] En contre-partie, les liens  $\sigma$  ont une contribution essentielle à la formation du squelette de la molécule. Puisque les orbitales  $p$  des molécules avoisinantes se chevauchent et sont dirigées perpendiculairement au plan de la molécule, les électrons- $\pi$  qui les occupent sont alors délocalisés de part et d'autre de cette dernière tel que démontré à la Fig.2.1. Conséquemment, ces derniers sont responsables de la conductivité des matériaux organiques et sont à l'origine des transitions électroniques décrites dans ce document.

Les polymères semi-conducteurs formés à partir de molécules conjuguées similaires au benzène ont des propriétés électroniques qui s'apparentent à celles des matériaux inorganiques. De façon analogue aux bandes de valence et de conduction, ces derniers ont des orbitales moléculaires remplies et vides. Les orbitales moléculaires qui sont remplies forment l'équivalent de la bande de valence dans les semiconducteurs inorganiques et l'orbitale moléculaire remplie de plus haute énergie est appelée HOMO ("Highest Occupied Molecular Orbital"). Les orbitales vides forment l'équivalent de la bande de conduction et celle de plus basse énergie est nommée LUMO ("Lowest Unoccupied Molecular Orbital"). Ainsi, les transitions électroniques se produisant suite à l'absorption d'un photon se font entre la bande HOMO et LUMO et leur espacement énergétique (bande interdite) est typiquement de l'ordre de quelques électrons-volts. Puisque l'énergie de cette bande interdite correspond à l'énergie des photons dans la région visible du spectre électromagnétique ( $\sim 1.60\text{-}3.25\text{ eV}$ ), on dit que les matériaux  $\pi$ -conjugués sont des matériaux "colorés". Bien que leur bande interdite reste bien inférieure à celle du silicium (1.1 eV), ils occupent tout de même une place importante au sein des dispositifs optoélec-

troniques puisqu'ils absorbent dans une région du spectre électromagnétique où le soleil émet son maximum de radiation.

## 2.2 Procédés optiques dans les matériaux organiques

Les outils qui nous permettent de sonder les états électroniques des matériaux sont multiples. Une grande partie des travaux de cette thèse se base sur l'étude de phénomènes reliés à l'interaction entre la lumière et la matière, un principe largement étudié par spectroscopie optique. L'utilisation d'une sonde optique non destructrice nous permet de questionner l'état électronique d'un système. Nous pouvons étudier le système à l'état d'équilibre ou encore sonder l'évolution temporelle des états électroniques. Ces informations sont nécessaires à la compréhension de la relation fondamentale entre la microstructure et les processus optiques observables.

### 2.2.1 Perturbation optique d'un système

Les électrons- $\pi$  peuvent interagir avec une radiation électromagnétique dont l'énergie est supérieure à l'énergie de la bande interdite du matériau, i.e  $\hbar\omega \geq E_{\text{LUMO}} - E_{\text{HOMO}}$ . L'absorption d'un photon a pour effet d'exciter un électron- $\pi$  de la bande HOMO vers la bande LUMO d'une molécule. Cette interaction est considérée comme étant une perturbation de l'état fondamental de la molécule et peut être évaluée à l'aide de la théorie des perturbations au premier ordre. Ainsi, le taux de transition est directement tiré à partir de la valeur attendue d'un hamiltonien perturbatif dans l'état fondamental. Cette perturbation électromagnétique est gouvernée par l'hamiltonien dipolaire électrique [36] :

$$H_{\text{dip}} = \vec{\mu} \cdot \vec{E}. \quad (2.1)$$

Cet hamiltonien décrit le couplage entre le champ électrique perturbatif d'une radiation incidente,  $\vec{E} = E_0 \cos(\omega t) \hat{k}$ , au moment dipolaire ( $\vec{\mu} = -e \sum_j \vec{r}_j$ ) de la mo-

lécule. Ici, nous négligeons l'étendue spatiale de  $\vec{E}$  puisque la longueur d'onde de l'excitation  $\lambda$  est beaucoup plus grande que les distances typiques intermoléculaires. Le taux de transition d'électrons entre l'état initial (fondamental) et final (excité)  $\psi_i$  et  $\psi_f$  est donné par la règle d'or de fermi [37] :

$$T_{i \rightarrow f} = \frac{2\pi}{\hbar} |\langle \Psi_f | \hat{H}_{dip} | \Psi_i \rangle|^2 \rho_f \delta(E_f - E_i - \hbar\omega), \quad (2.2)$$

où  $\rho_f$  est la densité d'états finaux accessibles.  $E_i$  et  $E_f$  sont les énergies des états initiaux et finaux et  $\hbar\omega$  l'énergie de la radiation incidente. Le terme  $|\langle \Psi_f | \hat{H}_{dip} | \Psi_i \rangle|^2$  peut être nul en raison de la symétrie particulière des états initiaux et finaux. Dans ce cas, on dit qu'une transition électronique est non permise.

### 2.2.2 L'approximation de Born-Oppenheimer

La distribution des niveaux d'énergie d'un système moléculaire est complexe et peut être déterminée, en principe, en résolvant l'équation de Schrödinger indépendante du temps :

$$H_{\text{mol}} \Psi = E_{\text{mol}} \Psi. \quad (2.3)$$

L'hamiltonien moléculaire,  $H_{\text{mol}}$ , comprend les termes d'énergie cinétique des électrons et noyaux ainsi que les interactions électrons-électrons, électrons-noyaux et noyaux-noyaux. Puisque les électrons participant aux transitions électroniques sont beaucoup plus légers que les protons ( $m_p/m_e \approx 1800$ ), leur réponse suite à une excitation optique est pratiquement instantanée ( $\sim 10^{-15}$  s) contrairement à la réponse beaucoup plus lente du noyau de la molécule ( $\sim 10^{-13}$  s). [38] Une approximation généralement utilisée en modélisation consiste à découpler le comportement des électrons de celui des noyaux en termes indépendants dans l'hamiltonien. Dans cette approximation adiabatique,  $H_{\text{mol}}$  prend la forme :

$$\hat{H}_{\text{mol}} = H_{\text{el}} + H_{\text{el-nuc}} + V_{\text{nuc-nuc}}. \quad (2.4)$$

Les états propres du système,  $|\Psi\rangle$ , deviennent alors un simple produit des fonctions d'ondes électronique,  $\phi$ , et vibrationnelle,  $\chi$  avec la forme :  $|\Psi\rangle = |\phi\rangle|\chi\rangle$ . [39] Le taux de transition en absorption de l'Éq.2.2 prend alors la forme

$$T_{i \rightarrow f} = \frac{2\pi}{\hbar} |\langle \phi_f | \hat{H}_{dip} | \phi_i \rangle|^2 |\langle \chi_f | \chi_i \rangle|^2 \rho_f \delta(E_f - E_i - \hbar\omega). \quad (2.5)$$

Le terme  $|\langle \phi_f | \hat{H}_{dip} | \phi_i \rangle|^2$  est relié au moment dipolaire de transition purement électronique.  $|\langle \chi_f | \chi_i \rangle|^2$  est appelé *facteur Franck-Condon* et représente le chevau-chement entre les fonctions d'ondes vibrationnelles de l'état fondamental et excité. Ce dernier est responsable de la forte modulation en intensité des différentes transitions électroniques observables dans les spectres d'absorption et photoluminescence de films de P3HT.

### 2.2.3 Influence du couplage électrons-phonons sur la forme spectrale en photoluminescence

Les états initiaux,  $|i\rangle$ , et finaux,  $|f\rangle$ , d'un système dépendent de plusieurs degrés de liberté liés aux coordonnées des électrons et du noyau. Il est alors conventionnel de représenter les degrés de liberté nucléaire comme des modes normaux de la molécule. Chaque mode normal étant associé à une coordonnée normale  $Q_\alpha$  (phonons d'Einstein) avec une fréquence caractéristique  $\omega_\alpha$ . Ces modes de vibration intramoléculaires peuvent se coupler aux transitions électroniques. Dans la majorité des molécules conjuguées, un mode de vibration intramoléculaire associé à l'étirement des atomes de carbones C=C avec une fréquence caractéristique  $\omega_\alpha \approx 180$  meV prédomine. L'approximation de Franck-Condon est essentiellement une reformulation plus restrictive de l'approximation de Born-Oppenheimer, i.e. on assume que les transitions électroniques se font si rapidement que les coordonnées nucléaires res-

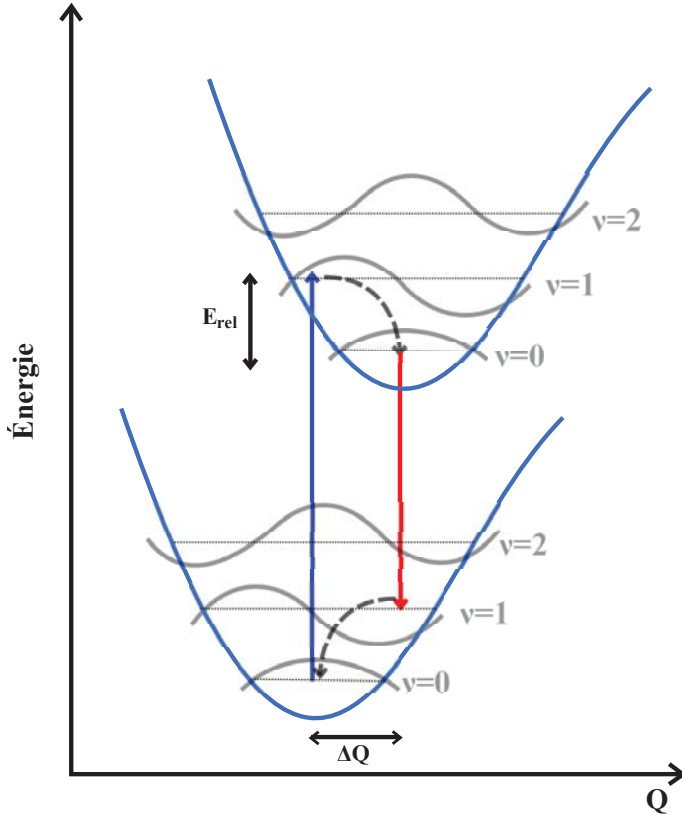


Figure 2.2 – Représentation schématique d'une transition vibronique dans la situation où la géométrie d'équilibre diffère entre l'état fondamental et l'état excité. Les puits de potentiel quadratiques sont équivalents à ceux d'oscillateurs harmoniques.  $E_{rel}$  désigne l'énergie de relaxation suivant la transition électronique. Les niveaux vibrationnels sont indiqués par les indices  $v$ . Dans cette figure, nous observons la transition 0–2 en absorption (bleu) et photoluminescence (rouge).

tent stationnaires pendant la transition. D'autre part, les fréquences de vibration sont typiquement 1 ordre de grandeur plus faible que les énergies des transitions électroniques qui se font verticalement.

La transition optique entre l'état fondamental et l'état excité d'une molécule est schématisée à la Fig.2.2. De façon générale, le minimum d'énergie du puits de potentiel de l'état excité se situe à une position  $Q$  qui diffère de celle de l'état fondamental en conséquence de la différente distribution électronique. Ainsi, une transition verticale termine sur un état excité ayant le même  $Q$  que l'état fonda-

mental. Puisque le temps de vie de l'état excité est beaucoup plus grand que le temps associé au mouvement du noyau, il se produit une relaxation non radiative en  $\sim 10^{-13}$  s vers le bas de la courbe énergétique. Le retour de l'électron vers l'état fondamental se fait aussi verticalement, signature caractéristique des matériaux à bande interdite directe, avec une énergie d'émission plus faible que celle associée à l'absorption. La différence énergétique entre le photon de plus basse énergie absorbé et celui de plus haute énergie réémis est appelée *décalage de Stokes*. Plus la molécule est "rigide", plus ce décalage est faible. Une conséquence fondamentale du couplage des modes de vibration nucléaires aux transitions électroniques est qu'il apparaît une progression linéaire d'oscillateurs harmoniques pour chaque état électronique. Ces transitions équidistantes énergétiquement sont schématisées par les lignes verticales dans les puits de potentiels de la Fig.2.2. D'après l'Eq.2.5, le poids porté par chaque transition vibronique est donné par le facteur Franck-Condon, qui lui dépend de l'intégrale de superposition des fonctions d'ondes nucléaires de l'état initial et final :

$$F_{i,f} = |\langle \chi_i | \chi_f \rangle|^2 \quad (2.6)$$

Suite à la thermalisation ultrarapide des électrons, seulement l'état vibrationnel nul de l'état excité ( $v = 0$ ) est occupé. Ici,  $v$  représente le nombre de quanta de vibration impliqués dans la transition. Le facteur Franck-Condon à T=0 K pour une transition  $v = 0$  vers un  $v$  non nul est alors donné par l'expression suivante [38] :

$$F_{0,v} = \langle 0 | v \rangle^2 = \frac{\exp(-S) S^v}{v!}. \quad (2.7)$$

$S$  est le facteur *Huang-Rhys* défini comme :

$$S = \frac{k(\Delta Q)^2}{2\hbar\omega_p}, \quad (2.8)$$

où  $k$  est la constante de rappel de l'oscillateur,  $\omega_p$  est la fréquence du phonon d'énergie  $E_p$  et  $\Delta Q$  décrit le changement de coordonnées configurationnelles entre l'état  $S_0$  et  $S_1$ . L'éq.2.7 démontre alors que pour une molécule isolée couplée à un mode de vibration, la progression en intensité des transitions électroniques suit une distribution poissonienne. Le facteur  $S$  est aussi défini comme étant la constante du couplage électron-phonon et renseigne sur l'étendue de la déformation géométrique de l'état excité par rapport à l'état fondamental. Le paramètre de Huang-Rhys correspond physiquement aux nombres moyens de phonons impliqués dans le processus de relaxation. Il est à noter que lorsque  $S = 0$ , seule la transition entre le niveau vibronique nul ( $v = 0$ ) de l'état fondamental et le niveau vibronique nul ( $\tilde{v} = 0$ ) de l'état excité est accessible (transition notée 0–0). De plus,  $F_{0,v}$  doit satisfaire la règle de sommation,  $\sum_v F_{0,v} = 1$ . Il en résulte que lorsque  $S$  augmente, la force d'oscillateur est transférée de la transition 0–0 vers les transitions 0– $v$ .

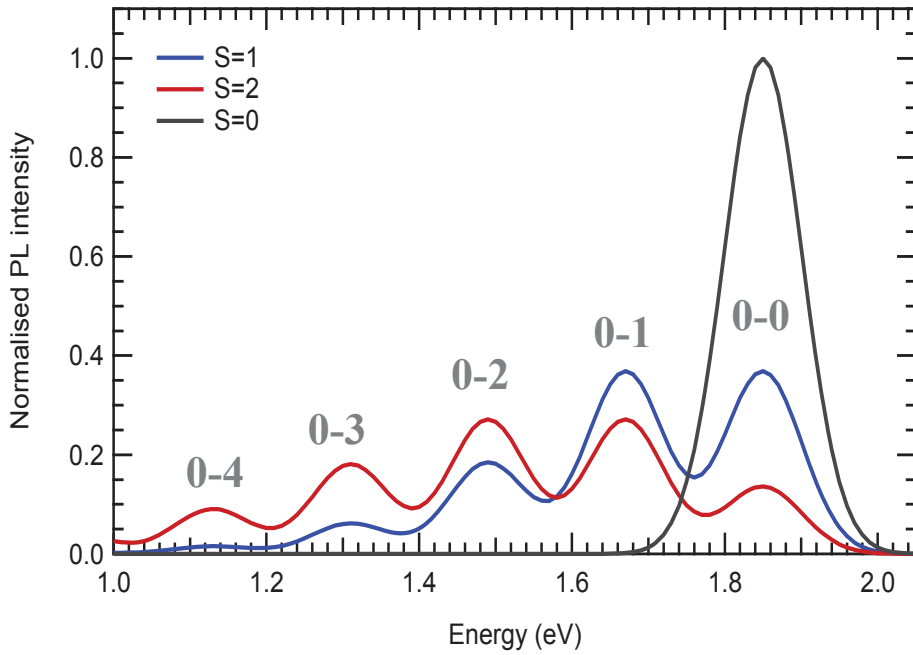


Figure 2.3 – Forme spectrale de la photoluminescence d'une molécule isolée en fonction du paramètre Huang-Rhys,  $S$ , pour différentes valeurs définies dans la légende.  $\omega_p=180$  meV ,  $\sigma = 0.4\omega_p$  (largeur de la transition),  $E_0=1.85$  eV .

À partir de l'Éq.2.7, il en découle que la forme spectrale en absorption et photoluminescence d'une molécule isolée peut être décrite par la sommation sur toutes les transitions électroniques accessibles. Notamment, en photoluminescence on trouve la forme typique suivante [36] :

$$I_{PL}(\omega) \propto \sum_m \frac{S^m \exp(-S)}{m!} \Gamma(E_0 - mE_p - \hbar\omega) \quad (2.9)$$

où  $\Gamma$  est une gaussienne centrée à l'énergie de la transition électronique.  $E_0$  est l'énergie de la transition de plus haute énergie (0–0),  $E_p = 180$  meV est l'énergie du mode de vibration principal couplé aux transitions et  $\hbar\omega$  l'énergie du photon émis. La fonction  $I_{PL}(\omega)$  est présentée à la Fig.2.3 pour différentes valeurs de  $S$ . L'élargissement des transitions provient principalement du couplage à une multitude de modes vibrationnels moléculaires de plus basse énergie ainsi qu'à ceux du réseau. Le facteur Huang-Rhys peut être déterminé expérimentalement en prenant le ratio entre l'intensité des transitions 0–2 et 0–1 de la progression vibronique de la photoluminescence. À partir de l'Éq.2.9 on obtient :

$$S = 2 \frac{I_{PL}^{0-2}}{I_{PL}^{0-1}} \quad (2.10)$$

Dans les agrégats moléculaires, la distribution en intensité des différentes transitions électroniques s'éloigne de la distribution poissonienne de l'Éq.2.7. L'étude de la distorsion de cette progression est un outil précieux pour extraire de l'information sur l'assemblage des molécules, le désordre énergétique et moléculaire ainsi que sur certaines propriétés excitoniques.

#### 2.2.4 Transitions optiques radiatives et non radiatives

La fig.2.4 couvre les différentes transitions électroniques entre les niveaux d'énergies qui peuvent être observées par spectroscopie d'absorption et photoluminescence. L'état fondamental est singule (S<sub>0</sub> : S=singule, 0=état fondamental) et les deux

électrons occupant la HOMO sont de spins opposés suite au principe d'exclusion de Pauli. L'absorption d'un photon peut alors propulser un électron- $\pi$  vers un niveau vibrationnel non nul de l'état excité. Puisque cette interaction avec la radiation électromagnétique n'affecte pas le spin de l'électron, celui-ci occupera un état excité aussi de caractère singulet, i.e. un niveau  $S_n$ . L'état  $S_1$  est généralement celui qui est directement accessible avec une excitation optique dans la région visible du spectre électromagnétique tandis que les états singulets d'énergie supérieure,  $S_2$ ,  $S_3$  etc., sont généralement accessibles à l'aide d'une seconde excitation d'énergie  $\hbar\omega = E_{S_2} - E_{S_1}$  qui peut, par exemple, amener un électron de l'état  $S_1$  à  $S_2$ . Ce type de transition est facilement observable par spectroscopie d'absorption et absorption transitoire. L'absorption d'un photon est ainsi décrite par le processus :  $S_0 + \hbar\omega \rightarrow S_1$  où  $\hbar\omega$  est l'énergie du photon absorbé.

Suite à l'excitation optique, l'exciton généré est "chaud". Ceci désigne que l'électron a un excès d'énergie par rapport au minimum de la bande LUMO. Il s'en suit alors une relaxation vibrationnelle vers le bas de la bande, un processus qui se fait très rapidement ( $\sim 100$  fs) [40] comparativement au temps de vie radiatif de l'exciton qui varie de quelques centaines de picosecondes à quelques nanosecondes dépendamment du système. La quantité d'énergie moyenne impliquée dans cette relaxation est donnée par : [36]

$$E_{rel} = SE_p. \quad (2.11)$$

Dans la majorité des molécules conjuguées, y compris le P3HT, l'étirement des liens C=C avec une énergie de  $\sim 1400$  cm $^{-1}$  est le principal responsable de la réorganisation nucléaire. Avec un facteur Huang-Rhys de l'ordre de  $S \approx 1$ ,  $E_{rel}$  est de l'ordre de  $\sim 180$ -200 meV. Le processus de thermalisation non radiative et ultrarapide de l'exciton vers le bas de la bande est appelé *conversion interne*. Par la suite, la fluorescence se produit à partir du niveau vibrationnel nul de l'état

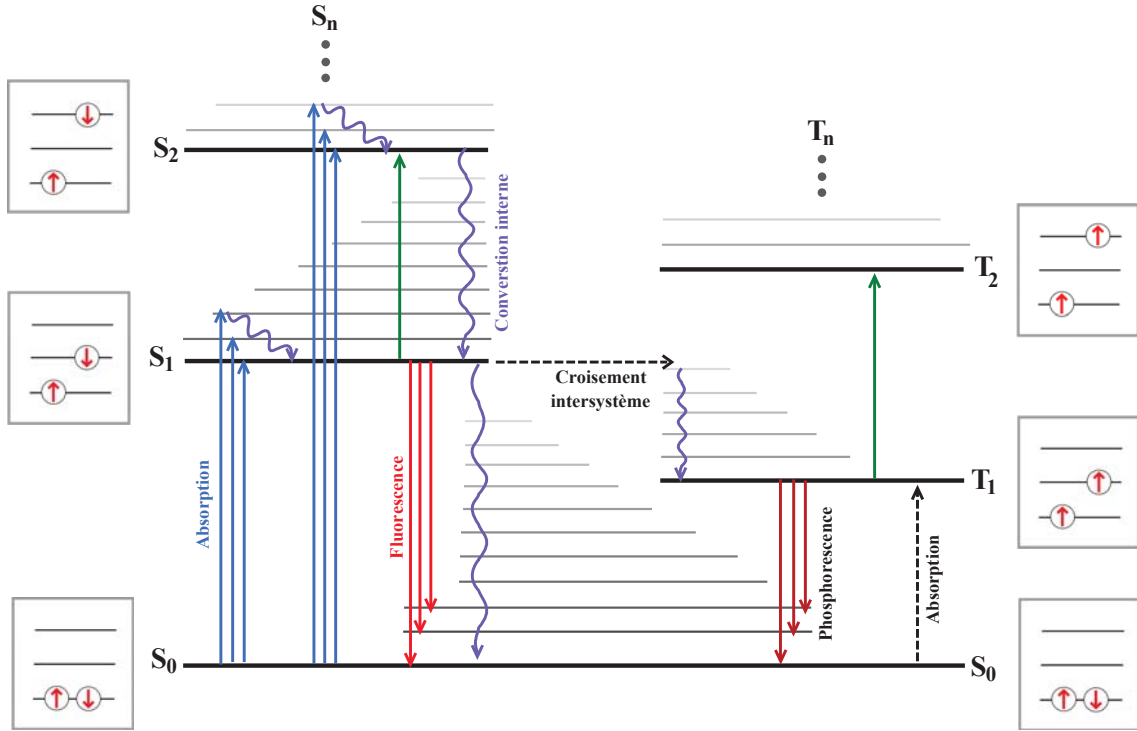


Figure 2.4 – Transitions électroniques d'une molécule : L'absorption d'un photon (ligne bleue) se fait entre l'état fondamental  $S_0$  et un niveau vibrationnel de l'état singulet excité  $S_n$ . Par la suite, il y a thermalisation de l'exciton vers le bas de la bande (ligne ondulée mauve) et recombinaison vers un niveau vibrationnel de l'état fondamental (ligne rouge). Un électron occupant un l'état singulet peut changer d'orientation de spin pour générer un exciton triplet par croisement inter système (ligne pointillée horizontale). L'absorption directe vers l'état triplet  $T_n$  est non permise (ligne pointillée verticale) et la recombinaison vers l'état fondamental donne lieu à la phosphorescence. Les orientations du spin des électrons participant aux transitions sont montrées dans les boîtes encadrées.

excité vers l'état fondamental, en accord avec la loi de Kasha. Cette loi empirique est fondée sur la disparité entre l'échelle temporelle de la relaxation vibrationnelle ( $\sim$  fs) versus le temps de vie de l'exciton ( $\sim$  ns). Ainsi la relaxation de l'excitation vers le bas de la bande se fait beaucoup plus rapidement que la désexcitation vers l'état fondamental. La molécule peut aussi transférer de l'énergie à des modes de vibrations de façon non radiative. [41]

### 2.2.5 Excitons singulets et triplets

L'hamiltonien dipolaire de l'Éq.2.1 n'influence pas le spin de l'électron- $\pi$  participant à la transition électronique. Ainsi, la fonction d'onde électronique de la molécule,  $\phi$  peut alors être exprimée comme étant le produit d'une fonction d'onde purement électronique,  $\Phi$ , et une fonction d'onde portant l'information de spin  $S$  (à ne pas confondre avec le paramètre de Huang-Rhys). Ainsi, l'Éq.2.5 peut finalement être écrite comme :

$$T_{i \rightarrow f} = \frac{2\pi}{\hbar} |\langle \Phi_f | \hat{H}_{dip} | \Phi_i \rangle|^2 |\langle \chi_f | \chi_i \rangle|^2 |\langle S_f | S_i \rangle|^2 \rho_f \delta(E_f - E_i - \hbar\omega). \quad (2.12)$$

où  $|\langle S_f | S_i \rangle|^2$  exprime la projection de l'état de spin de l'état fondamental (singulet) sur l'état final. Puisque les fonctions d'ondes de spins sont orthogonales,  $T_{i \rightarrow f} \neq 0$  seulement lorsque le niveau final est de type singulet. Pour cette raison, les excitons *triplets* (spins totaux unitaires) ne peuvent être générés directement par une excitation (ligne pointillée verticale à la Fig.2.4). Cependant, il est possible qu'un électron occupant un état singulet change de spin sous l'influence d'une interaction secondaire (généralement due au couplage spin-orbite, une interaction non négligeable dans les matériaux comportant des atomes lourds). On appelle *croisement intersystème* cette transition non radiative entre l'état singulet et triplet. Les excitons triplets ainsi formés ont un temps de vie pouvant aller jusqu'à la milliseconde dû à la nature interdite de leur recombinaison vers l'état fondamental singulet. Le décalage énergétique entre les niveaux énergétiques des états singulets et triplets est donné par le terme d'énergie d'échange.

$$S_1 - T_1 = 2J = \int \int \psi_i^*(\vec{r}_1) \psi_j^*(\vec{r}_2) V_{e-e}(\vec{r}_1 - \vec{r}_2) \psi_j(\vec{r}_1) \psi_i(\vec{r}_2) dr_1 dr_2. \quad (2.13)$$

où  $\vec{r}_1$  et  $\vec{r}_2$  sont la position des électrons 1 et 2 et  $\psi_i$ ,  $\psi_j$  la fonction d'onde décrivant la position de ces électrons. Ainsi le décalage entre l'état singulet et triplet vaut deux fois l'énergie d'échange électronique. Puisque nous formons ainsi un système de fermions, la fonction d'onde totale du système doit nécessairement être symétrique sous échange de particules. Pour un exciton singulet dont la fonction d'onde de spin est anti-symétrique sous échange de particules, la fonction d'onde spatiale doit être symétrique. L'inverse est vrai pour les excitons triplets. Ainsi, le terme d'échange a pour effet d'augmenter l'énergie de l'état singulet et rabaisser celui de l'état triplet. [42] La valeur typique de ce décalage est d'environ 0.7 eV dans les matériaux  $\pi$ -conjugués. [39, 43] Par exemple, la recombinaison d'excitons triplets est observable dans le rra-P3HT et le rr-P3HT en solution et est caractérisée par une émission à long temps de vie et décalée vers le rouge comparativement à l'émission de l'exciton singulet. [44, 45]

### 2.3 Excitons dans des agrégats moléculaires

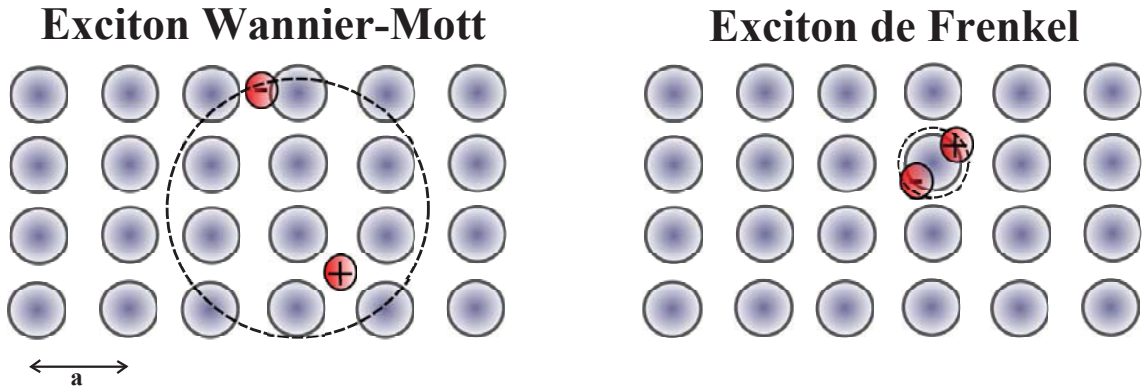


Figure 2.5 – Illustration schématique du rayon de Bohr,  $a_0$ , d'un exciton Wannier-Mott et Frenkel.  $a$  désigne le paramètre de maille du cristal. L'exciton Wannier-Mott est caractérisé par  $a_0 \gg a$  contrairement à l'exciton de Frenkel où  $a_0 \sim a$ .

La nature des excitons dans les matériaux organiques diffère largement de ceux présents dans les matériaux inorganiques. En effet, la constante diélectrique plus

faible dans ces premiers empêche l'écrantage partiel des paires électron-trou dont l'attraction coulombienne mutuelle engendre une énergie de liaison décrite par :

$$E_b = \frac{1}{2} \frac{e^2}{4\pi\epsilon_r\epsilon_0 r_n}. \quad (2.14)$$

avec  $r_n = n^2 a_0$  le rayon de l'orbite de la paire électron-trou,  $n$  le nombre quantique principal et  $a_0$  le rayon de bohr excitonique.  $\epsilon_r$  est la constante diélectrique du milieu,  $\epsilon_0$  la permittivité du vide et  $r$  la distance de séparation entre l'électron et le trou. Ainsi, le rayon de bohr est donné par :

$$a_0 = \frac{4\pi\epsilon_r\epsilon_0\hbar^2}{\mu e^2},$$

avec  $\mu$  la masse réduite de la quasi-particule. Par exemple, dans le GaAs  $\epsilon_r \approx 12.8$  et l'énergie de liaison de l'exciton dans ce système est d'environ 4.2 meV et la distance électron-trou moyenne de l'ordre de 13 nm. [46] Dans la plupart des matériaux organiques,  $\epsilon_r$  est  $\approx 2 - 4$ . [47] Conséquemment, le rayon de Bohr de l'exciton "inorganique" est beaucoup plus grand que le paramètre de maille du réseau tandis que l'exciton "organique" est généralement localisé sur un monomère tel que schématisé à la Fig.2.5. La relaxation structurelle due aux interactions entre les électrons et le réseau force aussi la localisation de l'onde d'excitation. [47] On peut alors trier les excitons en deux classes : Excitons de Wannier-Mott et excitons de Frenkel. Ces premiers sont caractérisés par une énergie de liaison relativement faible (de l'ordre de  $\sim 10$  meV) par rapport à l'énergie thermique du système, [48] contrairement aux excitons de Frenkel qui ont une énergie de liaison qui peut aller de quelques centaines de meV jusqu'à  $\sim 1$  eV. [46] Il va de soi que la dissociation des excitons Wannier-Mott est beaucoup plus efficace et se fait généralement très rapidement à température pièce où  $k_B T > E_{\text{liaison}}$ , expliquant en partie la disparité entre l'efficacité de conversion énergétique entre les matériaux organiques et inorganiques.

Dans les agrégats moléculaires formés à partir de structures supramoléculaires composées de longues chaînes planaires, les excitons peuvent afficher un comportement hybride entre celui des excitons Wannier-Mott en Frenkel. En d'autres termes, le long de la chaîne, la paire électron-trou peut se séparer sur quelques unités monomériques tandis que le long de l'axe de l'agrégat, l'exciton est plutôt de type Frenkel, avec une séparation qui s'étale généralement sur la chaîne avoisinante la plus près. [49, 50]

### 2.3.1 Largeur de bande de l'exciton

La réponse optique d'un agrégat moléculaire diffère largement de celle de molécules isolées puisque les interactions entre molécules permettent la délocalisation des excitations dans le réseau cristallin, un phénomène qui a été constaté par Yakov Frenkel en 1931. Pour expliquer le concept d'exciton de Frenkel, supposons un cristal linéaire composé de  $N$  molécules identiques espacées d'une distance  $d$ . Supposons qu'une molécule absorbe un photon et devient excitée électroniquement (état  $S_1$ ). Si l'on néglige les interactions intermoléculaires, la fonction d'onde de l'agrégat de  $N$  molécules est un simple produit de l'état excité de cette molécule avec les  $N - 1$  autres molécules dans leur état fondamental. Puisque la probabilité d'exciter chaque molécule est identique, les énergies des états du cristal ont une dégénérescence de  $N$ .

Dans le cas plus physique, on permet une interaction intermoléculaire (couplage excitonique),  $J_0$ , entre voisins les plus près. Cette interaction lève ainsi la dégénérescence du système et permet une délocalisation de l'excitation sur toute la chaîne (en négligeant le désordre énergétique). En d'autres termes, ce paquet d'excitation est partagé de façon cohérente par chaque molécule. Une excitation électronique localisée sur une molécule  $i$  du cristal peut être décrite de la façon suivante :

$$|n\rangle = |g\rangle_1 |g\rangle_2 \dots |E\rangle_n \dots |g\rangle_{N-1} |g\rangle_N, \quad (2.16)$$

où  $|E\rangle_n$  désigne que l'état excité ( $S_1$ ) de la  $n^{ime}$  molécule tandis que les  $N-1$  autres sont dans leur état fondamental,  $|g\rangle$ . L'état total du cristal est alors une combinaison linéaire des fonctions d'onde exprimée à l'Éq. (2.16) :

$$\Psi = \sum_{n=1}^N C_n |n\rangle. \quad (2.17)$$

Les coefficients  $C_n$  sont déterminés en minimisant l'énergie  $\langle \Psi | H_{\text{mol}} | \Psi \rangle$ . En supposant un espacement  $d$  équidistant entre les molécules, les conditions périodiques imposent la forme suivante à la fonction d'onde excitonique :

$$\Psi_k = \sum_{n=1}^N e^{iknd} |n\rangle \quad (2.18)$$

où  $k = 0, \pm 2\pi/Nd, \pm 4\pi/Nd$  etc. Une telle onde d'excitation est appelée exciton de Frenkel. Lorsqu'on introduit l'interaction intermoléculaire entre voisins les plus près,

$$H_{ex} = J_0 \sum_{n=1}^{N-1} \{|n\rangle\langle n+1| + |n+1\rangle\langle n|\}, \quad (2.19)$$

l'hamiltonien d'interaction 2.19 agit sur  $\Psi_k$  et on trouve :

$$\begin{aligned} H\Psi_k &= \sum_n e^{inkd} \left[ \epsilon + J_0(e^{-ikd} + e^{+ikd}) \right] |n\rangle \\ &= [\epsilon + 2J_0 \cos(kd)] \Psi_k \end{aligned}$$

Ici,  $\epsilon$  est l'énergie de la transition électronique de la molécule isolée et  $J_0$  le couplage entre les molécules, représentant le taux de transfert d'énergie entre deux molécules adjacentes. L'interaction intermoléculaire fait alors apparaître une bande énergétique nommée largeur de bande de l'exciton libre ( $W$ ). Cette largeur de bande vaut,  $W = 4J_0$ , et décrit la différence énergétique entre le haut et le bas de la bande

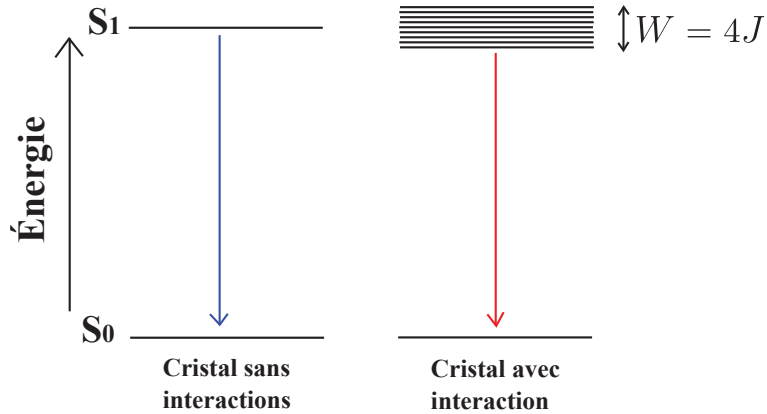


Figure 2.6 – Schématisation de l'effet du couplage intermoléculaire sur les niveaux énergétiques du cristal moléculaire. Le couplage excitonique,  $J_0$ , entre les molécules avoisinantes lève la dégénérescence des niveaux d'énergie d'un cristal sans interaction, créant une bande de largeur  $W = 4J_0$ .

excitonique tel que schématisé à la Fig.2.6.  $W$  est la largeur de bande purement électronique lorsqu'on néglige le couplage aux modes de vibrations.

## 2.4 Interactions dans les agrégats moléculaires

Les matériaux qui sont au cœur des dispositifs optoélectroniques mentionnés à la section 1.1 sont largement plus complexes que de simples molécules isolées. En effet, ces amas de molécules liées par des forces de van der Waals faibles forment des structures supramoléculaires complexes (agrégats moléculaires) dans lesquels l'orientation des molécules les unes par rapport aux autres joue un rôle prépondérant sur les propriétés optiques.

### 2.4.1 Interactions dipôle-dipôle : Agrégats de type H et J

D'un point de vue purement électronique, l'impact de l'agrégation de molécules sur la réponse optique d'un système a été déterminé en grande partie par Kasha. [51] En effet, dans les agrégats moléculaires, le couplage  $J_0$  de l'Eq.2.19 est une interaction électronique résonante de type coulombienne (dipôle-dipôle). La

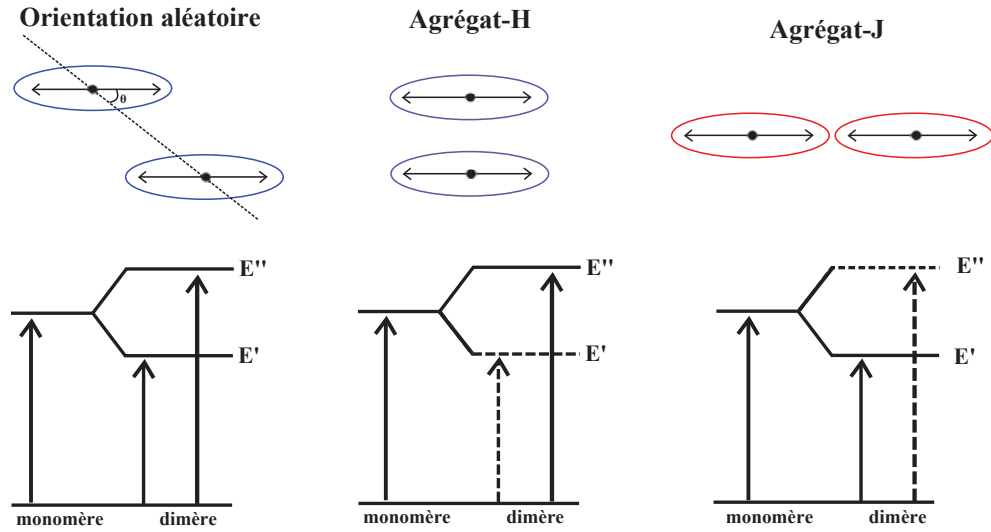


Figure 2.7 – Effet de l’interaction dipôle-dipôle sur les niveaux énergétiques d’un dimère. Pour une orientation cofaciale des dipôles, l’énergie de l’état  $S_1$  est surélevée lorsque les dipôles pointent dans la même direction. Pour une orientation tête-à-tête, l’état  $S_1$  se situe à plus basse énergie et pour une orientation aléatoire, les deux transitions permises correspondent à la projection du dipôle sur les deux axes x et y.

force de ce couplage a un impact profond sur la délocalisation et le transport des excitons dans le matériau [7, 52] et modifie substantiellement l’énergie des états électroniques du cristal. Prenons le cas simplifié de deux dipôles ponctuels dont l’interaction est donnée par l’expression :

$$J_{\text{dip-dip}} = \frac{\mathbf{M}_u \cdot \mathbf{M}_v}{r^3} - \frac{3(\mathbf{M}_u \cdot \mathbf{r})(\mathbf{M}_v \cdot \mathbf{r})}{r^5}, \quad (2.20)$$

avec  $\mathbf{M}_u$  et  $\mathbf{M}_v$ , le moment de transition dipolaire de deux molécules,  $u$  et  $v$ . Sous cette forme,  $\mathbf{r}$  représente la position vectorielle du dipôle de la molécule  $v$  en référence à celui de la molécule  $u$ . Pour une orientation aléatoire des dipôles,  $J_{\text{dip-dip}}$  prends la valeur de l’Eq.2.20. Puisque le moment de transition du dimère est donné par :

$$\mathbf{M}_{\pm} = \frac{1}{\sqrt{2}}(\mathbf{M}_u \pm \mathbf{M}_v), \quad (2.21)$$

$M_{\pm}$  sera non nul seulement lorsque les moments de transition de dipôles individuels pointent dans la même direction. Lorsque deux molécules sont positionnées face à face tel que schématisé à la Fig.2.7(b) ( $\theta = 90^\circ$ ), les produits  $\mathbf{M}_u \cdot \mathbf{r}$  et  $\mathbf{M}_v \cdot \mathbf{r}$  sont nuls et  $J_{\text{dip-dip}} = \frac{\mathbf{M}_u \cdot \mathbf{M}_v}{r^3} > 0$ . Dans ce cas, l'énergie de l'état  $S_1$  est plus élevée que celle de la molécule isolée et correspond au cas où les dipôles sont orientés parallèlement ( $E''$ ). Lorsque  $\theta = 0^\circ$ , tel que schématisé à la Fig.2.7(c),  $J_{\text{dip-dip}} = -2 \frac{\mathbf{M}_u \cdot \mathbf{M}_v}{r^3} < 0$  et le niveau  $S_1$  est situé à plus basse énergie que dans le cas de la molécule isolée et correspond à une orientation tête-à-queue des dipôles ( $E'$ ).

La grandeur de  $|J_0|$  dicte le taux de transfert d'énergie résonante entre molécules et est beaucoup plus faible pour les polymères que pour les oligomères. [15, 53–55]. Ceci découle du fait que les chaînes plus longues permettent le confinement de la fonction d'onde excitonique sur deux segments séparés de deux chaînes en interaction. Lorsque  $|J_0|$  est plus petit que l'énergie des phonons du système (ce qui est généralement le cas pour les polymères), nous sommes dans un régime de couplage excitonique faible ou de façon équivalente, dans un régime de couplage fort entre les électrons et phonons. [56] Bien que l'expression 2.20 n'est généralement pas valide lorsque la taille de la molécule dépasse la distance intermoléculaire (ce qui est le cas pour les polymères), le comportement de  $|J_0|$  sur les niveaux d'énergies de la molécule est le même. Dans ces cas, des approximations plus détaillées, tel que celles de dipôles linéaires peuvent être utilisées. [57, 58]

#### 2.4.2 Propriétés optiques des agrégats de types H et J

La courbure de la relation de dispersion des excitons dans les agrégats de polymères dépend largement de la conformation des molécules et de la force de leur interaction. Au panneau gauche de la Fig.2.8, on remarque que la courbure de  $E(k)$  pour les agrégats J comportant N molécules agencées en conformation tête-à-queue est négative et montre un minimum au bas de la bande, correspondant aux excitons dont  $k = 0$ . Ceci découle du fait que  $E(k)$  est minimal lorsque les  $N$  moments de

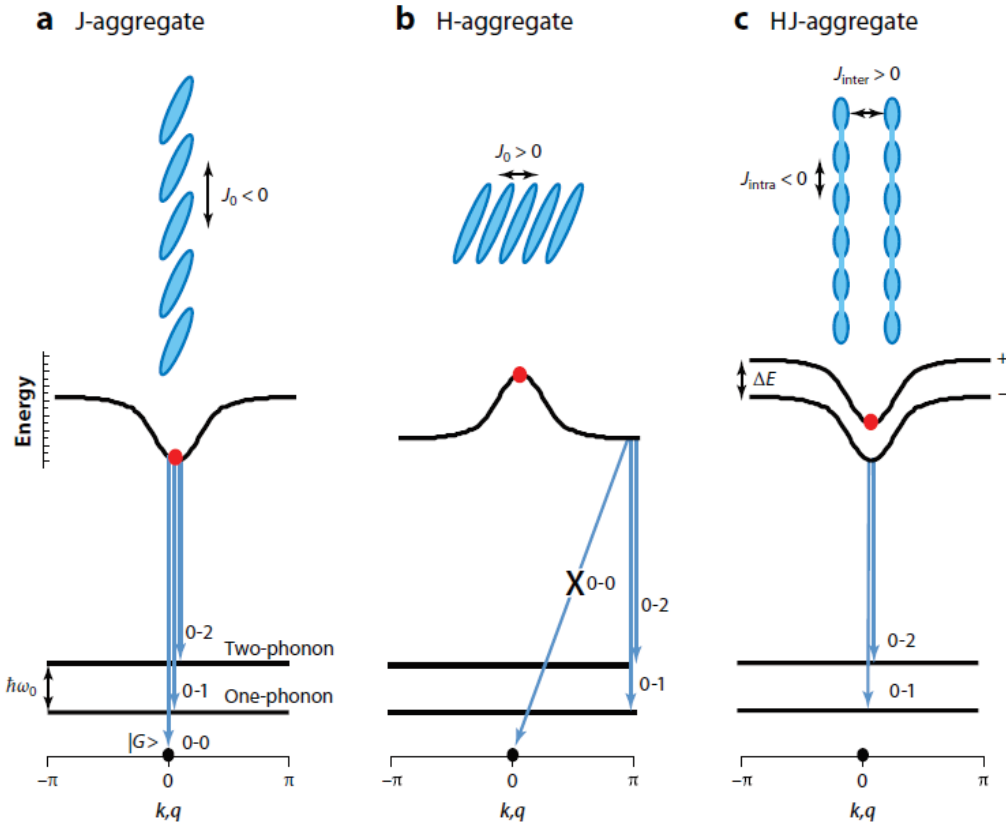


Figure 2.8 – Orientation moléculaire et relation de dispersion dans les agrégats H, J et HJ. Dans les agrégats J, le couplage excitonique  $J_0$  est négatif et engendre une courbure négative de la relation de dispersion. L'exciton  $k=0$  se trouve alors au bas de la bande et la recombinaison se fait vers les niveaux vibroniques de l'état fondamental. Dans les agrégats-H,  $J_0 > 0$  et l'exciton sombre ( $k = 0$ ) se trouve au haut de la bande. Ceci empêche la recombinaison vers l'état vibronique nul de l'état fondamental. Dans les agrégats H-J, la bande de l'agrégat-J est séparée du couplage intermoléculaire. De façon similaire aux agrégats-H, la transition 0-0 est seulement activée thermiquement ou par le désordre énergétique. (Image tirée de la Réf. [50])

transition dipolaire sont parfaitement alignés et la fonction d'onde de l'exciton 2.18 ne comporte aucun noeud. L'état à partir duquel l'exciton est émis,  $|em\rangle$  correspond à  $k = 0$  et l'émission peut se faire vers tous les niveaux vibrationnels de l'état fondamental. Pour les agrégats-H, la courbure de la relation de dispersion est inversée. Ceci découle du fait que  $k = 0$  correspond au cas où les  $N$  moments de transition

dipolaire cofaciaux pointent dans la même direction, donnant une conformation énergétiquement plus élevée comparativement au cas où les  $N$  moments alternent de molécule en molécule ( $k = \pi$ ).

Tel que décrit à la section 2.5, seules les excitons dont la fonction d'onde présentée à l'Eq.2.18 ne comporte pas de noeuds ( $k = 0$ ) peuvent être excités optiquement à partir de l'état fondamental. Dans les agrégats de type J, l'exciton  $k = 0$  réside au bas de la bande alors que l'exciton sombre ( $k = \pi$ ) dont la fonction d'onde comporte  $N - 1$  noeuds réside au sommet de la bande (cf. Fig.2.8). Dans les agrégats-H, le comportement est inversé. Ceci a une conséquence fondamentale sur la forme spectrale de la photoluminescence des excitons dans les agrégats-H : En absence de désordre énergétique, la transition 0–0 en photoluminescence est non permise. Ce résultat découle du fait que la phase de l'état de plus basse énergie duquel l'exciton est émis,  $|em\rangle$ , alterne de molécule en molécule. Pour cette raison, les molécules formant des agrégats-H ont un taux d'efficacité de photoluminescence beaucoup plus faible que les agrégats-J, faisant d'eux de meilleurs candidats pour les dispositifs photovoltaïques.

L'observation des spectres d'absorption et de photoluminescence des agrégats H et J démontre les comportements suivants :

1. Dans les agrégats-H, le ratio entre l'intensité des deux premiers pics en absorption,  $A^{0-0}/A^{0-1}$ , décroît lorsque le couplage intermoléculaire augmente ( $W$  augmente), un phénomène lié au mélange entre les bandes excitoniques. En photoluminescence, le ratio entre les deux premiers pics,  $I_{PL}^{0-0}/I_{PL}^{0-1}$ , croît avec le désordre énergétique (structurel) et une augmentation de la température. L'effet du désordre est de briser la symétrie du système et conséquemment réduire la longueur de cohérence de l'exciton.
2. Dans les agrégats-J, le ratio entre l'intensité des deux premiers pics en absorption croît lorsque le couplage intermoléculaire augmente ( $W$  augmente).

En photoluminescence, le ratio entre les deux premiers pics décroît avec le désordre énergétique et une augmentation de la température. De façon similaire aux agrégats-H, le désordre énergétique engendre une réduction de la longueur de cohérence de l'exciton et conséquemment une baisse de l'intensité 0-0 dont la force d'oscillateur est proportionnelle au nombre de molécules connectées de façon cohérente.

Ces signatures spectrales explicites permettent alors d'obtenir une compréhension sur la nature des excitons dans les agrégats moléculaires en faisant une étude exhaustive de la forme spectrale de l'absorption et photoluminescence.

#### **2.4.3 Comportement hybride des agrégats HJ**

Les interactions le long de la chaîne d'un polymère isolé lui confèrent un comportement de type agrégats-J. Dans le cas où l'on obtient un agencement cofacial des chaînes de polymère, l'exciton est délocalisé non seulement le long de la chaîne, mais aussi dans la direction de l'empilement. Conséquemment, la courbure de la relation de dispersion suit la forme affichée à la Fig.2.8(c), i.e typique d'un agrégat-J avec un décalage lié aux interactions interchaînes. De façon similaire aux agrégats-H, la transition vers l'état fondamental est interdite à T=0 K et sans désordre énergétique. [50, 59] Ainsi, la photophysique de ce type de matériau dépend largement de la compétition entre le couplage intrachaîne, permettant à l'exciton de "surfer" le long du squelette de la molécule et le couplage interchaîne, à travers l'espace entre les chaînes agencées cofacialement.

### **2.5 Introduction aux excitons polaroniques**

Les polymères sont plus déformables que leurs confrères inorganiques et les effets reliés à la relaxation structurelle d'une molécule suite à une excitation, notamment le réarrangement des noyaux, force la localisation de l'exciton. Ainsi, l'exciton de

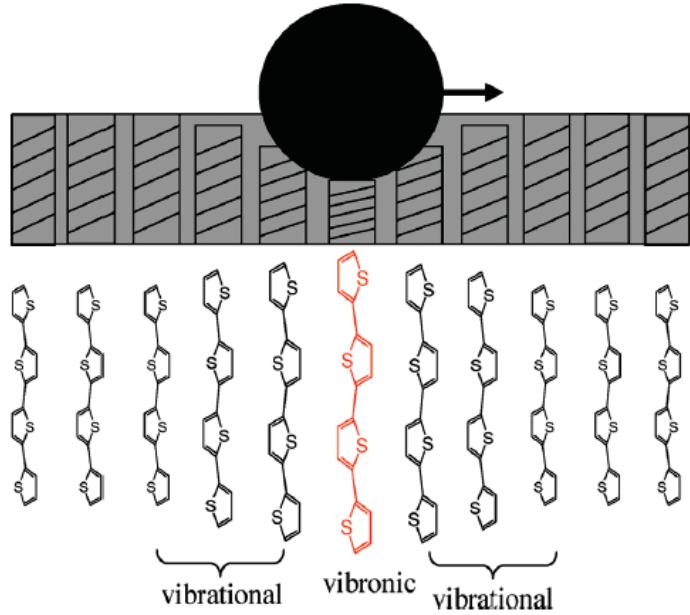


Figure 2.9 – Illustration schématique de la distorsion d'un cristal suite à une excitation de Frenkel polaronique. Telle une boule de quilles déformant les ressorts d'un matelas, l'exciton polaronique engendre une distorsion des molécules avoisinantes. Schéma tiré de la Réf. [56].

Frenkel dans les matériaux  $\pi$ -conjugués est aussi appelé exciton polaronique. Il peut être vu comme le produit d'une molécule centrale  $i$  excitée ( $S_1$ ) sur une chaîne de polymère accompagnée de molécules avoisinantes excitées vibrationnellement, mais pas électroniquement. Ce caractère provient du couplage significatif entre les modes de vibrations intramoléculaires et l'excitation électronique. Les molécules avoisinantes du centre de masse de l'exciton subissent alors une déformation géométrique en conséquence de la réponse de la molécule à cette excitation primaire. Le produit final est une excitation entourée d'un champ vibrationnel avec une étendue spatiale qui dépend notamment de la structure du cristal et du désordre énergétique.

Schématisé à la Fig.2.9, cet exciton "vibronique" est analogue à une boule de quilles circulant sur un matelas à ressorts. Cette dernière comprime les ressorts localement, mais aussi ceux qui sont adjacents au centre de masse. Simplement, dans les matériaux conjugués, les molécules subissent une élongation plutôt qu'une

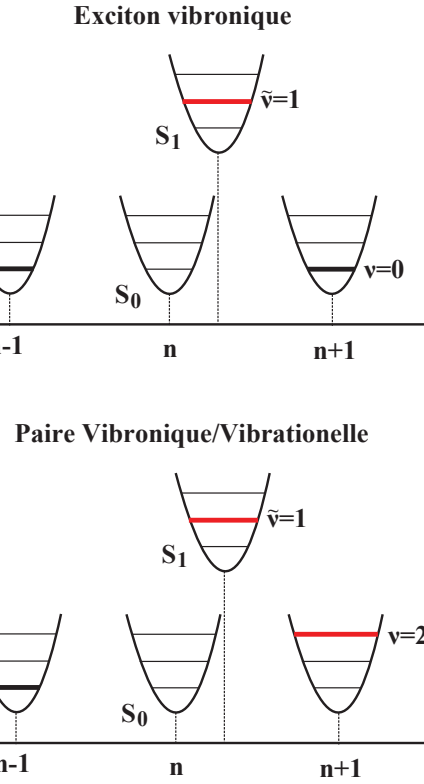


Figure 2.10 – Exemple d’excitations fondamentales dans les structures supramoléculaires. L’état de l’excitation vibronique à 1 particule est noté  $|n, \tilde{v} = 1\rangle$  et l’excitation d’une paire vibronique/vibrationnelle est notée  $|n, \tilde{v} = 1; n+1, v = 2\rangle$ . Image basée sur la fig.3 de la réf. [60].

compression. Un formalisme rigoureux doit tenir compte de ce phénomène de déformation vibrationnelle du réseau entourant l’excitation vibronique pour expliquer les propriétés optiques de plusieurs matériaux  $\pi$ -conjugués. La fonction d’onde des excitons de Frenkel polaroniques peut être décrite théoriquement à l’aide d’une base à multi particules, généralement tronquée à 2 particules. La Fig.2.10 schématise ces excitations. Chaque chromophore de l’agrégat (segment de polymère) est défini comme étant un système électronique comportant deux niveaux :  $S_0$  et  $S_1$ . L’excitation à 1 particule,  $|n, \tilde{v}\rangle$  désigne un chromophore excité (vibroniquement et vibrationnellement) à un site  $n$  donné avec  $\tilde{v}$  quanta de vibration dans l’état excité alors que toutes les autres molécules sont dans leur état fondamental et non excitées

vibrationnellement ( $\nu = 0$ ).

Une paire vibronique/vibrationnelle est un état à 2 particules désigné  $|n, \tilde{v}; n', v'\rangle$ . Ainsi, en plus d'avoir une excitation vibronique sur un site  $n$ , cet état comprend aussi une excitation vibrationnelle au site  $n'$  qui contient  $v'$  quanta de vibration dans le potentiel nucléaire de l'état fondamental. Dans cette base à multi particules introduite par Philpott [61], le  $i$ ème état propre de l'hamiltonien de l'agrégat est exprimé comme un développement des états à 1 et 2 particules :

$$|\psi^{(i)}\rangle = \sum_{n, \tilde{v}} C_{n, \tilde{v}}^{(i)} |n, \tilde{v}\rangle + \sum_{n, \tilde{v} n', v'} C_{n, \tilde{v}; n', v'}^{(i)} |n, \tilde{v}; n', v'\rangle \quad (2.22)$$

Sans la contribution du deuxième terme de l'Éq.2.22, la fonction d'onde aurait la forme de l'éq.2.18. La réponse des excitations décrites par cette équation suit alors les propriétés suivantes :

- Seuls les états à 1 particule sont optiquement atteignables via l'état fondamental où  $\nu = 0$ . Ils sont alors responsables de l'émission 0–0.
- Les états à 1 et 2 particules peuvent se coupler radiativement à l'état fondamental où  $\nu \neq 0$ . Ils sont alors tous deux responsables de l'émission des répliques vibroniques (0–1,0–2 etc.)
- En absence de désordre énergétique, seuls les excitons dont la fonction d'onde ne comporte pas de noeuds ( $k = 0$ ) sont accessibles à partir de l'état fondamental où  $\nu = 0$  de façon consistante avec la règle de transition :  $\Delta k=0$ .

Les coefficients  $C_{n, \tilde{v}}^{(i)}$ ,  $C_{n, \tilde{v}; n', v'}^{(i)}$  de l'Éq.2.22 peuvent être évalués en diagonalisant l'hamiltonien de la chaîne dont la forme dépend du système et des approximations utilisées. L'hamiltonien d'interaction excitonique entre les chaînes avoisinantes

$$H_{ex} = J_0 \sum_{n=1}^{N-1} \{ |n\rangle\langle n+1| + |n+1\rangle\langle n| \}, \quad (2.23)$$

sert à coupler les états à 1 particule, permettant par le fait même le transfert d'énergie résonant entre différentes molécules. Ce couplage est donné par l'élément :

$$\langle n, \tilde{v} | H_{ex} | m, \tilde{v}' \rangle = J_0 f_{\tilde{v},0} f_{\tilde{v}',0} \delta_{m,n\pm 1}, \quad (2.24)$$

où l'intégrale de chevauchement des fonctions d'onde vibrationnelles  $f_{\tilde{v},0}$  est donnée par l'Éq.2.7 .  $H_{ex}$  sert aussi à coupler les états à 2 particules et ceux à 1 et 2 particules via l'élément :

$$\langle m, \tilde{v} | H_{ex} | n, \tilde{v}'; n', v' \rangle = J_0 f_{\tilde{v},v'} f_{\tilde{v}',0} \delta_{m,n'} \delta_{n',n\pm 1}. \quad (2.25)$$

Conséquemment, les états à 2 particules empruntent une partie de la force d'oscillateur associée aux états à 1 particule. En absence de désordre énergétique, les états décrits par l'Éq.2.22 sont délocalisés dans tout le cristal. En pratique, le désordre énergétique diagonal qui est reflété par une fluctuation des énergies des sites de la molécule sert à localiser l'excitation vibrationnelle et à réduire la cohérence de l'exciton. [60] Théoriquement, ce désordre énergétique est décrit par une distribution gaussienne d'énergie des bandes HOMO et LUMO dont la déviation standard peut avoisiner les 50-100 meV. [22, 62] Ce formalisme est nécessaire pour décrire l'étendue spatiale de la fonction d'onde de l'exciton vibrationnel et est un concept clé pour décrire la relation entre les propriétés optiques et la microstructure des matériaux formant des arrangements supramoléculaires.

## 2.6 Excitations intrachaine

Les excitons générés en réponse à une excitation optique peuvent être délocalisées le long de la chaîne via deux mécanismes : premièrement, via le mécanisme d'interaction dipôle-dipôle à travers l'espace tel que décrit à l'éq.2.20. Deuxièmement, les excitons sont susceptibles à un mécanisme de superéchange. L'origine de ce mécanisme à deux étapes réside dans la fluctuation virtuelle de l'exciton de

Frenkel localisé sur un monomère en un exciton à transfert de charge localisé sur deux monomères adjacents et finalement un exciton de Frenkel sur le second monomère. La force de cette interaction peut être dérivée en théorie des perturbations du deuxième ordre et varie comme : [63]

$$J_{SE} \propto -\frac{t(\phi)^2}{\Delta E}, \quad (2.26)$$

où  $t(\phi)^2$  est l'intégrale de transfert proportionnel à l'enchevêtrement des orbitales- $\pi$  des monomères adjacents sur une chaîne et  $\Delta E$  est la différence d'énergie entre l'exciton de Frenkel et l'exciton à transfert de charge. Pour deux monomères orientés à 90 ° l'un par rapport à l'autre, il y a un bris de conjugaison des orbitales  $\pi$  et  $t(\phi)$  est nul. Le signe négatif de l'éq.2.26 confère alors un comportement de type agrégat-J aux chaînes de polymères isolées. [63] Lorsqu'on inclut le couplage intermoléculaire entre les chaînes avoisinantes, la forme spectrale en photoluminescence révèle alors que la cohérence de l'exciton est bidimensionnelle, légèrement anisotrope le long de la chaîne et le long de l'axe de l'agrégat et porte une signature typique de la microstructure que lui confère le poids moléculaire des chaînes. [64]

## 2.7 Les paires de polarons

Les paires de polarons sont les espèces intermédiaires entre l'exciton de Frenkel et les électrons et trous indépendants. En ce sens, ils ont une énergie de liaison plus faible que l'exciton de Frenkel et leur présence est détectable par des méthodes de type pompe-sonde (déttection directe) ou encore photoluminescence (déttection indirecte, lorsqu'ils reforment des excitons). Puisqu'il n'y a pas de recouvrement entre la fonction d'onde de l'électron et du trou qui forme cette paire, ces espèces peuplent des états sombres et leur recombinaison vers l'état fondamental ne peut se faire directement. La recombinaison des paires de polarons compétitionne alors avec leur séparation en électron et trou indépendants.



## CHAPITRE 3

# TWO-DIMENSIONAL SPATIAL COHERENCE OF EXCITONS IN SEMICRYSTALLINE POLYMERIC SEMICONDUCTORS : EFFECT OF MOLECULAR WEIGHT

### 3.1 Contexte de l'article

Le présent article traite de la nature intrinsèque des excitons créés dans des films de P3HT et sert à faire le pont entre la théorie qui permet de déduire le rôle des interactions dans les agrégats (H-J) moléculaires à partir de la forme spectrale en absorption et photoluminescence observée expérimentalement. On s'intéresse principalement à la cohérence de l'exciton, ou plus spécifiquement la longueur de cohérence définissant l'étendue spatiale de la fonction d'onde de l'exciton vibronique dont la forme est donnée à l'Éq.2.22. Dans un cristal sans désordre énergétique et sans couplage aux modes de vibrations, la longueur de cohérence de l'exciton s'étend sur tout le cristal et est limitée par la taille des molécules. En réalité, le désordre énergétique et le couplage aux modes de vibrations intramoléculaires forcent la localisation de l'exciton, [65, 66] un comportement qui compétitionne avec la nature délocalisatrice du couplage intermoléculaire.

La photophysique des polymères conjugués formant des agrégats moléculaires relève généralement d'une compétition entre les interactions intrachaine qui donnent un comportement de type agrégat-J et interchaine, qui leur confère un comportement de type agrégat-H. Dans plusieurs systèmes, l'une de ces interactions domine sur l'autre. Par exemple, un cas spécifique d'agrégat-J est celui de cristaux parfait de polydiacetylene (PDA). En effet, dans ce matériau formant de longs agrégats-J unidimensionnels, il a été observé une cohérence spatiale macroscopique et unidimensionnelle de l'ordre de quelques micromètres, limitée par la longueur des

chaînes. [67]. Cette observation a été réalisée en regardant l’interférence entre l’émission de l’état excitonique  $k = 0$  pour deux segments de chaînes espacés spatialement. Cette cohérence macroscopique peut donner lieu à de la superradiance, [68, 69] un phénomène exploitable dans les lasers organiques. Dans certains matériaux, les interactions inter/intrachaine sont du même ordre de grandeur, engendrant ainsi un comportement hybride de type agrégat-HJ. La photophysique du P3HT est généralement décrite selon un formalisme d’agrégats-H avec un hamiltonien de type Holstein qui tient compte du couplage électron-phonons et du couplage excitonique résultant de l’interaction cofaciale entre les chaînes de polymères dans l’empilement- $\pi$ . [62] Ce modèle d’agrégat-H est un modèle unidimensionnel, i.e on néglige totalement les interactions intrachaines et chaque segment de polymère dans l’empilement- $\pi$  est traité comme un chromophore unique qui est couplé aux voisins le plus près par un terme de couplage excitonique. Bien que ce modèle unidimensionnel permette de distinguer certaines subtilités des propriétés optiques dans la majorité des films de P3HT étant donné les faibles poids moléculaires commercialement accessibles et les traitements standards avec des solvants à faible point d’ébullition par enduction centrifuge, de récents travaux démontrent que le P3HT peut aussi former de longues nanofibres qui lui confère des propriétés optiques qui ressemblent largement à celles des agrégats-J. [70] Nous avons aussi dernièrement observé ce comportement dans un complexe de P3HT :PEO. Un résultat important de nos travaux est que l’addition de PEO affecte positivement le degré de planarisation des chaînes de P3HT de haut poids moléculaire, ce qui donne lieu à une signature d’absorption typique aux agrégats-J. [71] Dans ces cas spécifiques, la force d’oscillateur de la transition 0–0 en absorption et photoluminescence est supérieure à celle des répliques vibroniques et l’émission est décalée vers le rouge.

### 3.1.1 Sonde spectroscopique ultrarapide et en continu

Plusieurs techniques s'offrent à nous pour sonder la dynamique des états excités sur de courtes et longues échelles temporelles. Ici, nous nous intéressons aux courtes échelles de temps (quelques picosecondes) puisque c'est sur cette échelle de temps qu'on peut observer l'influence de la réorientation géométrique qui tend à rendre les chaînes plus planaires suite à une excitation optique ainsi que la relaxation torsionnelle qui s'en suit. [72] Puisque le désordre énergétique responsable de la localisation de l'exciton provient majoritairement du degré de torsion des chaînes, nous utilisons une technique de photoluminescence par somme de fréquence pour sonder l'évolution de la transition 0-0 qui est sensible à la cohérence de l'exciton et au désordre énergétique. Cette technique consiste à séparer une impulsion ultrarapide ( $\sim 150$  fs) en deux impulsions. L'une sert à exciter l'échantillon tandis que l'autre est une impulsion servant d'interrogation du système. La photoluminescence émise par l'échantillon est alors envoyée sur un cristal de bêta borate de baryum (BBO). Il en est de même pour l'impulsion d'interrogation dont le délai d'arrivée peut être balayé. On détecte alors les photons réémis à la sortie du cristal, à la somme de fréquence entre celle de la PL et celle de la seconde impulsion. Cette technique permet alors d'obtenir une résolution temporelle de l'ordre de la centaine de fs. La nécessité d'une telle résolution est cruciale puisque la réorganisation géométrique des chaînes de polymère, suite à une excitation, se fait très rapidement ( $\sim 10$  ps). [72]

Lorsqu'on excite le polymère à l'aide d'un laser continu (mais modulé à basse fréquence par un hacheur mécanique), nous sondons principalement l'émission des excitons de plus basse énergie, à leur état de quasi-équilibre. Ces derniers proviennent des domaines de P3HT cristallins et leur recombinaison radiative porte une signature caractéristique de la morphologie des agrégats. Nous utilisons cette méthode spectroscopique pour quantifier la cohérence des excitons de plus basse

énergie tandis que les sondes optiques ultrarapides nous permettent de quantifier le degré de désordre torsionnel inhérent des chaînes.

### 3.2 Contribution originale de chaque coauteurs

Francis Paquin a initié les travaux de cette article via les mesures de photoluminescence à basse température. Les spectres de photoluminescence par somme de fréquence ont été pris par Luke X. Reynolds et Francis Paquin. L'analyse des mesures expérimentales a été faite par Francis Paquin. Les mesures de DSC ont gracieusement été fournies par Natalie Stingelin. Le calcul du paramètre Huang-Rhys a été fait par Nicolas Bérubé. Le modèle d'agrégat-H a entièrement été pris en compte par Hajime Yagamata, Nicholas J. Hestand et Frank C. Spano. La partie expérimentale du manuscript a été écrite par Carlos Silva et Francis Paquin tandis que la section théorique provient de Hajime Yamagata, Nicholas Hestand et Frank C. Spano. Tous les auteurs ont apportés leurs commentaires avant la version finale.

Two-dimensional spatial coherence of excitons in  
semicrystalline polymeric semiconductors : Effect of  
molecular weight

Francis Paquin,<sup>1</sup> Hajime Yamagata,<sup>2</sup> Nicholas J. Hestand,<sup>2</sup> Maciej Sakowicz,<sup>1</sup>  
Nicolas Bérubé,<sup>1</sup> Michel Côté,<sup>1</sup>, Luke X. Reynolds,<sup>3</sup> Saif A. Haque,<sup>3</sup>, Natalie  
Stingelin,<sup>4</sup> Frank C. Spano,<sup>2</sup> and Carlos Silva,<sup>1</sup>

<sup>1</sup>*Département de physique & Regroupement québécois sur les matériaux de pointe,  
Université de Montréal, C.P.6128, Succursale centre-ville, Montréal (Québec)  
H3C 3J7, Canada*

<sup>2</sup>*Department of Chemistry, Temple University, Philadelphia, PA 19122, United  
States*

<sup>3</sup>*Department of Chemistry and Centre for Plastic Electronics, Imperial College  
London, South Kensington Campus, London SW7 2AZ, United Kingdom*

<sup>4</sup>*Department of Materials and Centre for Plastic Electronics, Imperial College  
London, South Kensington Campus, London SW7 2AZ, United Kingdom*

Phys. Rev. B 88, 155202 (2013)

### 3.3 Abstract

The electronic properties of macromolecular semiconductor thin films depend profoundly on their solid-state microstructure, which in turn is governed, among other things, by the processing conditions selected and the polymer's chemical nature and molecular weight. Specifically, low-molecular-weight materials form crystalline domains of cofacially  $\pi$ -stacked molecules, while the usually entangled nature of higher molecular-weight polymers leads to microstructures comprised of molecularly ordered crystallites interconnected by amorphous regions. Here, we examine the interplay between extended exciton states delocalized along the polymer backbones and across polymer chains within the  $\pi$ -stack, depending on the structural development with molecular weight. Such two-dimensional excitations can be considered as Frenkel excitons in the limit of weak intersite coupling. We combine optical spectroscopies, thermal probes, and theoretical modeling, focusing on neat poly(3-hexylthiophene) (P3HT) - one of the most extensively studied polymer semiconductors - of weight-average molecular weight ( $M_w$ ) of 3-450 kg/mol. In thin-film structures of high-molecular-weight materials ( $M_w > 50$  kg/mol), a balance of intramolecular and intermolecular excitonic coupling results in high exciton coherence lengths along chains ( $\sim 4.5$  thiophene units), with interchain coherence limited to  $\sim 2$  chains. In contrast, for structures of low- $M_w$  P3HT ( $< 40$  kg/mol), the interchain exciton coherence is dominant ( $\sim 30\%$  higher than in architectures formed by high-molecular-weight materials). In addition, the spatial coherence within the chain is significantly reduced (by nearly 25%). These observations give valuable structural information; they suggest that the macromolecules in aggregated regions of high-molecular-weight P3HT adopt a more planar conformation compared to low-molecular-weight materials. This results in the observed increase in intrachain exciton coherence. In contrast, shorter chains seem to lead to torsionally more disordered architectures. A rigorous, fundamental description of primary

photoexcitations in  $\pi$ -conjugated polymers is hence developed : two-dimensional excitons are defined by the chain-length dependent molecular arrangement and interconnectivity of the conjugated macromolecules, leading to interplay between intramolecular and intermolecular spatial coherence.

### 3.4 Introduction

'Plastic' semiconductors are often regarded as complex systems as the conjugated macromolecules they are made of can adopt different arrangements and packing, leading to a diverse range of microstructures. These define their electronic properties. For instance, the chain conformation of conjugated polymers and the resulting microstructure has been shown to have a profound impact on the nature of intra- and interchain dispersion of  $\pi$ -electrons. [16, 18, 62, 73–79] Therefore, it is essential to learn how to manipulate these structural features. One option is to select materials of different molecular weight. From a perspective of classical polymer science, it is well established that polymers of low weight-average molecular weight ( $M_w$ ) form unconnected, extended-chain crystals, usually of a paraffinic-like arrangement. Due to the non-entangled nature of these relatively short-chain macromolecules, this leads to a polycrystalline, one-phase morphology. In contrast, with high- $M_w$  materials of molecular weight larger than the molecular weight between entanglements ( $M_e$ ), typically two-phase morphologies are obtained, which are comprised of crystalline moieties embedded in largely unordered (amorphous) regions, whereby individual macromolecules bridge multiple domains of order. [80]

Perhaps the central objective and challenge in the broad field of plastic electronics is to relate the electronic properties to the molecular order and thin-film architectures of the constituting materials; hence, significant research efforts have been devoted to that endeavor. Regioregular poly(3-hexylthiophene) (P3HT) has emerged as a model material to investigate the relationship between macromolecular configuration, microstructure and electronic properties. For example, charge transport in P3HT has been found to display clear trends with molecular weight and whether the film displays one-phase (polycrystalline) or two-phase (entangled) morphologies. In field-effect transistors, Kline et al. observed a systematic increase in field-effect mobilities up to a weight-average molecular weight of 40 kg/mol; [81–

83] in agreement with reports by Zhang et al. [30] and Koch et al. [19] On the other hand, bulk mobilities display more complex trends with molecular weight, and depend sensitively on film processing routes. Ballantyne et al. found, for instance, an order-of-magnitude decrease in bulk charge mobilities for P3HT of molecular weight  $M_w > 18$  kg/mol. [84] Koch et al. reported maximum bulk mobilities for P3HT of  $M_w \sim 4$  kg/mol. For materials of higher molecular weight, the time-of-flight mobility was found to be again reduced, leveling at a value of  $\sim 10 - 4$   $\text{cm}^2\text{V}^{-1}\text{s}^{-1}$ . [19] However, when films were cast at  $115^\circ\text{C}$ , the mobility increased by over an order of magnitude for materials of  $M_w < 10$  kg/mol, and decreased by over two orders of magnitude for P3HT of  $M_w \approx 60$  kg/mol. [19]

In this contribution, we focus on the nature of excitons in regioregular P3HT with molecular weights ranging from 3-450 kg/mol, where the microstructure changes from chain-extended crystals to a semicrystalline morphology where amorphous and crystalline domains are interconnected. [17, 79] This structural transition occurs at a molecular weight of around 25 to 35 kg/mol. [17, 79] Our strategy is to exploit the intricate influence of electronic structure and spatially correlated energetic disorder on the spectral line shapes in order to extract the microstructure-dependent information on exciton coherence. [56, 60, 85–88] More specifically, our objective is to explore how the exciton coherence lengths, measured along the polymer backbone and across the  $\pi$ -stack, vary with molecular weight and, in particular, with the structural change occurring above the entanglement limit. (The third dimension, which is directed along the lamellar axis, is neglected, as excitonic interactions are negligible between the well-separated  $\pi$ -stacks.) Although exciton coherence lengths have been defined in various ways, [56, 60, 86–88] we adapt the definition from Ref. [60] and generalize it to two dimensions. In short, we seek the two-dimensional exciton coherence function as a function of polymer structure.

Conjugated polymers are structurally complex and can, among other things, feature torsional disorder along the backbone, which translates into site energy

disorder. Furthermore, the  $\pi$ -electron coupling leading to electronic dispersion is highly anisotropic; dispersion along the chain is present due to intramolecular coupling between adjacent monomer motifs, but interchain coupling also clearly plays a role, leading to two-dimensional dispersion. [7, 52] As a consequence, neutral excitations (containing an electron and hole) in this class of materials can be considered to be in the Frenkel limit with respect to interchain interactions, highly localized to a few lattice sites across the lamellar lattice, spanning  $\sim 1$  nm, and highly influenced by energetic disorder. [60]

Spano has previously described excitons in regioregular P3HT by invoking a weakly coupled H-aggregate model, in which weak excitonic coupling (compared to molecular reorganization energies) between neighboring polymer chains within the  $\pi$ -stack leads to electronic dispersion of the vibronic molecular levels to form vibronic bands, with the bandwidth strongly dependent on microstructure. [66, 89] However, the importance of intra-chain coupling on optical spectral signatures has become evident by a recent report of J-aggregate like behavior in P3HT nanofibres [73] and in a P3HT :PEO complex [71] in which head-to-tail interactions of transition dipole moments of chromophores along the chain influence spectral line shapes. The limiting case of through-bond, intrachain excitonic coupling leads to what can be considered as Wannier-Mott-type excitons in one-dimensional lattices. [36, 90] In such excitons, the electron and hole are bound over several unit cells. A compelling example of this limit is provided by isolated, extended chains of red-phase polydiacetylene derivatives, [90] which show ultra narrow photoluminescence linewidths and superradiance [67, 91, 92] characteristic of J-aggregates at low temperature. [49] The work by Niles et al. [73] demonstrates that in regioregular P3HT films, there is a competition between J-like (intrachain) and H-like (interchain) excitonic coupling. [59] This interplay between through-bond and through-space excitonic coupling of adjacent chromophores must be strongly influenced by energetic disorder and hence the macromolecular conformation and packing in the

solid state.

In what follows, we combine steady-state and time-resolved optical spectroscopy, thermal analysis and theoretical modeling based on an effective Frenkel exciton Hamiltonian introduced in Ref. [59] in order to unravel the interplay between through-bond excitonic coupling within polymer chains, and Coulombic coupling between adjacent chains within a  $\pi$ -stack. Thus far, the result of such intrachain/interchain exciton coupling has been analyzed theoretically for the case of ordered aggregates with a thermal Boltzmann distribution of emitting excitons. [59] In this work we find that the influence of intrachain vs interchain coupling on the photophysical response is strongly dependent on the microstructure imposed by processing and materials parameters such as molecular weight. In order to interpret such effects theoretically we extend the analysis of Ref. [59] to the case of disordered aggregates. In the low molecular-weight regime, the paraffinic-like, chain extended structures seems to lead to short chromophores that produce more strongly coupled H-aggregates, very likely due to torsional disorder along the polymer backbone introduced, for example, through end-group effects. [81] On the other hand, films prepared with P3HT of molecular weight above the entanglement limit feature weaker interchain coupling but stronger intrachain coupling. We attribute this to the presence of longer-chain chromophore segments originating from torsionally more ordered (i.e. more planar) macromolecules. We thus find that the intrachain and interchain spatial coherence of excitons evolve with opposite trends with molecular weight, with longer intrachain coherence being observed for materials of high  $M_w$ , but longer interchain coherence in low-molecular weight materials. The photophysical properties arise from the competition between intrachain (through-bond) electronic coupling characteristic of Wannier-Mott excitons, and interchain (through-space) electronic coupling leading to Frenkel excitons, which generally dominate the photophysical properties of plastic semiconductors.

### 3.5 Experimental Methods

P3HT films of weight-average molecular weight ( $M_w$ ) in the range of 3-450 kg/mol were wire-bar-coated from p-xylene solution (1 wt% solid content) onto glass substrates. The solution temperature was 70 °C, and the substrate was also kept at 70 °C. Absorption spectra were measured using a commercial UV-Vis spectrophotometer (Perkin Elmer, Lambda25). The photoluminescence experiments were carried out by excitation with a continuous-wave laser (Ultralasers Inc., 200 mW maximum, 532 nm) modulated at a frequency of 100 Hz with a mechanical chopper (Terahertz Technologies), and detection with a 300-mm spectrometer (Princeton Instruments SP300 with EOS model S/PBS-025/020-TE2-H photoreceiver), and phase-sensitive detection (SR830 lock-in amplifier). The sample was housed in a closed-cycle, temperature controlled, sample-in-vapor cryostat (CryoIndustries of America).

The ultrafast time-resolved PL measurements were performed by femtosecond fluorescence upconversion. The samples were excited by the frequency-doubled output from an ultrafast mode-locked Ti :Sapphire oscillator (Newport Spectra-Physics Broadband MaiTai). Excitation and gate wavelengths were fixed at 400 and 800 nm, respectively. Both the gate and excitation beams were independently compressed using prism-pair compressors. The excitation intensity was adjusted to be below the onset of intensity dependent kinetics. Photoluminescence from the sample was focused on a 200- $\mu$ m-thick BBO crystal along with the 800-nm gate beam. Sum frequency generated photons (corresponding to photoluminescence at either 650 or 720 nm) were detected using a photomultiplier tube (R7207-01, Hamamatsu). The temporal resolution of the system was less than 150 fs. Sample degradation was avoided by performing the measurements under flowing nitrogen and using a translation stage to constantly move the sample within the beam, removing the effect of photo-bleaching and providing data averaged across the whole of the sample.

Melting temperatures,  $T_m$ , and enthalpies of fusion,  $\Delta H_f$ , were determined with a Mettler DSC822e differential scanning calorimeter (DSC), calibrated with indium and zinc. Samples of 1 - 5 mg (obtained from thin-film structures cast from solution following an identical protocol as for optical measurements) were sealed in aluminum crucibles and then heated under nitrogen at a scanning rate of 10 °C /min. Enthalpies of fusion were deduced from the surface area underneath the melting endotherms.

### 3.6 Results and Analysis

#### 3.6.1 Relationship between exciton signatures and solid-state microstructure

In this section, we explore the dependence of steady-state absorption and photoluminescence (PL) spectral line shapes of P3HT films with  $M_w$ . Fig.3.1(a) displays the room-temperature absorption spectra of films of P3HT of two different  $M_w$ ; one prepared with P3HT of low  $M_w$  (12.4 kg/mol) and one made of high- $M_w$  material (264 kg/mol). We discern two distinct differences in the spectral line shapes of these samples. The first concerns the relative absorbance of the origin of the vibronic progression at 2.0 eV. As mentioned in 3.4, previous work by Spano has demonstrated that the absorption line shape can be understood within the framework of a weakly coupled H-aggregate model. [62, 66, 75] Weak resonant Coulombic coupling between cofacial polymer chains,  $J_{\text{inter}}$ , results in electronic dispersion of the vibronic molecular levels to form vibronic bands with free-exciton bandwidth  $W = 4J_{\text{inter}}$ .  $W$  is related to absorbance ratio of 0-0 and 0-1 peaks at 2.0 and 2.2 eV, respectively. Assuming a single-chain Huang-Rhys parameter of unity [62], the ratio is given by [62, 66, 75]

$$\frac{A_{0-0}}{A_{0-1}} \approx \left( \frac{1 - 0.24W/\hbar\Omega_0}{1 + 0.073W/\hbar\Omega_0} \right)^2, \quad (3.1)$$

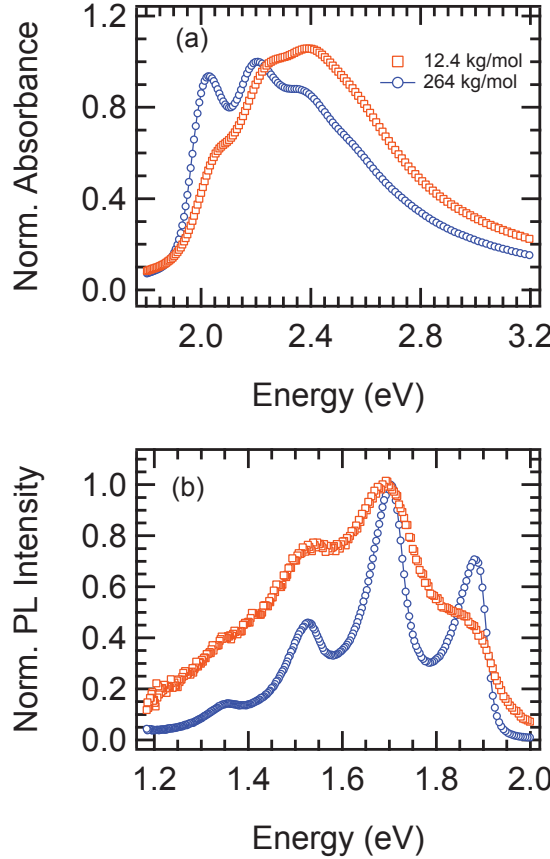


Figure 3.1 – Absorption and photoluminescence spectra in thin films of neat P3HT of low ( $12.4 \text{ kg/mol}$ ; chain extended structure - red symbols) and high ( $264 \text{ kg/mol}$ ; entangled, semicrystalline morphology - blue symbols). (a) Normalized absorption spectra for these films at room temperature. (b) Normalized photoluminescence spectra measured at  $T = 10 \text{ K}$ .

where  $\hbar\Omega_0 \approx 180 \text{ meV}$  is the effective energy of the main vibrational modes coupled to the electronic transition. Our optical absorption data presented in Fig.3.1(a) thus suggests that  $W$  decreases significantly in high- $M_w$  materials compared to P3HT of low  $M_w$ . We associate this noticeable variation in  $W$  between the two samples to conformational changes resulting from the significantly different average chain lengths associated with these two films. Excitonic coupling has been reported to vary inversely with conjugation length in P3HT, [16, 93] consistent with theoretical

predictions. [53, 57, 94, 95] Similar trends have been reported in a series of chiral oligothiophenes end-capped with ethylene oxide side chains. [93]

The second important difference in the absorbance spectra of low- and high- $M_w$  materials is the change in relative spectral weight at photon energies around 2.4 eV, which is higher for the sample of lower  $M_w$ . Absorbance in this high-energy region can be largely assigned to electronically uncoupled chromophores, [60, 62] implying that the lower  $M_w$  sample is comprised of a higher fraction of photophysically uncoupled polymer chains.

Further information can be obtained from the corresponding PL spectra of the two low- and high- $M_w$  samples, measured at 10 K (Fig.3.1(b)). Specifically, we observe a 0-0 (1.88 eV)/0-1 (1.70 eV) PL ratio that is significantly larger in the P3HT film of higher  $M_w$ ; we discuss this trend in more detail later in this section. In addition, we note that the 0-2 (1.52 eV)/0-1 (1.70 eV) intensity ratio also depends on  $M_w$ ; the smaller ratio for the higher  $M_w$  samples indicating a smaller Huang-Rhys parameter. This is somewhat surprising as it is inconsistent with the weakly-coupled H-aggregate model, [60] which predicts that in the weak excitonic coupling regime the relative intensities of the 0-1, 0-2, satellites should be independent of  $W$  (and disorder) and, hence, should resemble what is obtained for an isolated chromophore. Aggregation mainly influences the relative 0-0 peak intensity which depends entirely on the coherence of the emitting exciton, in marked contrast to the mainly incoherent origin of the vibronic satellites.

In order to examine these trends more quantitatively we measured absorption and PL spectra in a series of neat P3HT thin films using materials of  $M_w$  ranging from 2 to 347 kg/mol. We first plot  $W$  versus  $M_w$  (Fig. 2(a)), derived from eq.3.1. For materials of  $M_w < 50$  kg/mol, we deduce an average  $W = 81 \pm 11$  meV, while for P3HT of higher  $M_w$  we consistently derive an average  $W$  of  $21 \pm 2$  meV. (In the SI we show that the values of  $W$  increase by roughly 30% when evaluated using the HJ-aggregate model.) Tellingly, this transition of  $W$  is abrupt and occurs around

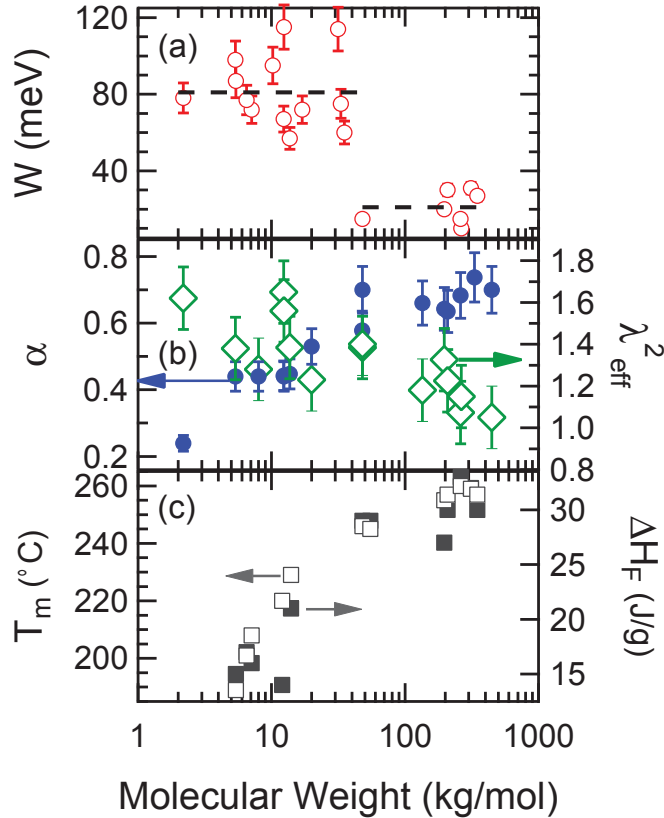


Figure 3.2 – (Color) Dependence of spectroscopic and microstructural features and parameters from spectral analysis on molecular weight of neat P3HT architectures.(a) Free-exciton bandwidth,  $W$ , derived from absorption spectra at room temperature. (b) Relative intensity of the 0-0 PL intensity,  $\alpha$ , and effective Huang-Rhys parameter,  $\lambda_{\text{eff}}^2$ , derived from photoluminescence spectra at 10 K. (c) Melting temperature,  $T_m$ , and enthalpy of fusion,  $\Delta H_f$ , derived from differential scanning calorimetry measurements.

$M_w \approx 50 \text{ kg/mol}$  - which is the molecular-weight region where the P3HT chains attain sufficient length to undergo entanglement, leading to a microstructural change from a paraffinic, chain extended phase to a two-phase morphology composed of interconnected crystalline and amorphous regions. [17, 19, 79, 81, 96] From the PL spectra of all the samples, we obtain the 0-0/0-1 intensity ratio and the effective Huang-Rhys parameter as a function of  $M_w$  via a fit with modified Franck-Condon model (see below) that takes into account the H-aggregate nature of the PL spec-

trum, namely, a symmetry-forbidden but disorder-allowed intensity of the 0-0 peak at 1.88 eV : [62]

$$\begin{aligned} I(\omega) &\propto (\hbar\omega)^3 n^3(\omega) e^{-\lambda_{\text{eff}}^2} \\ &\times \left[ \alpha \Gamma(\hbar\omega - E_0) + \sum_m \frac{\lambda_{\text{eff}}^{2m}}{m!} \Gamma(\hbar\omega - E_0 - m\hbar\Omega_0) \right], \end{aligned} \quad (3.2)$$

where  $n(\omega)$  is the refractive index of the film at the optical frequency  $\omega$ ,  $\lambda_{\text{eff}}^2$  is the effective Huang-Ryhs parameter,  $E_0$  is the energy of the origin of the vibronic progression,  $\hbar\Omega_0 = 180$  meV is the energy of the effective oscillator coupled to the electronic transition, and  $\Gamma(x)$  is a Gaussian function that represents the inhomogeneously broadened spectral line of the vibronic replica in the progression. The parameter  $\alpha$  thus quantifies the relative intensity of the origin of the vibronic progression (0-0), which is decoupled from the rest of the progression because it alone expresses the spatial coherence of the emitting Frenkel exciton within the H-aggregate model. [60] We display  $\alpha$  and  $\lambda_{\text{eff}}^2$  as a function of  $M_w$  in Fig.3.2(b). As the  $M_w$  of the P3HT films increases, we observe a strong increase in  $\alpha$  from 0.24 to 0.74, correlated with a decrease of  $\lambda_{\text{eff}}^2$  from  $\sim 1.5$  to just over 1 for high- $M_w$  samples. Note that for the analysis of the absorption spectrum reported in Fig.3.2(a), we assumed  $\lambda_{\text{eff}}^2=1$ . We also extracted values for  $W$  using  $\lambda_{\text{eff}}^2$  from the PL analysis in Fig.3.1(b), using a more general expression reported elsewhere [89] (see supp. information), generalized for arbitrary HR factors. This increases  $W$  by  $\sim 50\%$ . However, we expect that  $\lambda_{\text{eff}}^2$  in the absorption spectrum is intermediate between 1 and that measured by PL since the distribution of chromophore configurations is larger in absorption. Therefore, we choose to report  $W$  in Fig.3.2(a) obtained by imposing  $\lambda_{\text{eff}}^2=1$ .

The increase in  $\alpha$  - the relative 0-0 intensity - can be accounted for in the H-aggregate model as a decrease in  $W$ , an increase in the energetic disorder magnitude

(quantified by the width  $\sigma$  of a Gaussian distribution of site energies), a decrease in spatial correlation of site energies ( $\beta$ ), or some combination of the above. Here,  $\beta \equiv \exp(-1/\ell_0)$  where  $\ell_0$  is the site-energy spatial correlation length in units of the interchain separation. (Note that  $\beta$  ranges from 0 to 1 as  $\ell_0$  increases from 0 to infinity.) From the perturbative expression derived in Ref. [66] the scaling of the 0-0/0-1 PL ratio with the parameters  $\sigma$ ,  $\beta$  and  $W$  is,

$$\frac{I^{0-0}}{I^{0-1}} \sim \frac{(1-\beta)\sigma^2}{(1+\beta)W^2}, \quad (3.3)$$

which is strictly valid in the limit where  $(1-\beta)\sigma \ll W \ll \hbar\omega_0$ . Since the absorption and emission spectral line widths are smaller in the higher- $M_w$  films, the width of the disorder distribution is also smaller. A change in  $\sigma$  therefore cannot be responsible for the higher 0-0/0-1 ratio observed in the high  $M_w$  materials. Moreover, increasing order is usually coincident with an increasing spatial correlation parameter  $\beta$ , which also serves to decrease the 0-0/0-1 ratio and hence contradicts what we observe. The full influence of spatial correlation will be explored in greater detail later in section 3.6.2. (We find, in fact, that  $\beta$  increases for films prepared with higher  $M_w$  P3HT.)

The data displayed in Fig.3.2(a) shows, however, that  $W$  is significantly smaller for higher- $M_w$  samples (consistent also with increasing order) and thus, according to the H-aggregate model, a reduction in  $W$  would account for the observed increase in the PL 0-0/0-1 ratio with  $M_w$ . Because of the large change in  $W$  in the two well-defined  $M_w$  regimes, we expect that this parameter will represent the dominant contribution to the trend in  $\alpha$ . In the limit that  $W$  becomes negligible (i.e. in  $\pi$ -stacks consisting of polymers with very long conjugation lengths [53, 57, 94, 95]), the 0-0/0-1 line strength ratio is capped at the maximum value of value  $\lambda^2/2$ , the Huang-Rhys parameter representing a single chain in the  $\pi$ -stack. Measurements of Kanemoto et. al. [97] show that the single chain HR factor is approximately unity.

There is, however, evidence for the breakdown of the pure H-aggregate model in the recent literature. For instance, recent reports on P3HT whiskers (i.e. 'nanofibers' grown from relatively high molecular weight materials from solution over time), have shown that the ratio of the 0-0 to 0-1 PL peaks can be as high as two at room temperature, [73] suggesting that the line strength can significantly exceed the aforementioned cap. Additional evidence for the breakdown of the H-aggregate model comes from the decrease of the 0-2/0-1 peak ratio in the PL spectrum of materials of increasing  $M_w$  reported in this paper (Fig.3.1(b)). As mentioned in a prior work, [60] for the relatively weak values of W encountered in P3HT aggregates the *relative* strengths of the side-band peaks (0-1, 0-2, etc.) in the PL spectrum very closely resemble the isolated molecular values ; for example, the ratio of the 0-2 to 0-1 line strengths,  $I^{0-2}/I^{0-1}$ , remains steadfast at the value of  $\lambda^2/2$ , as determined from the Poissonian distribution for an isolated (single molecule) chain :

$$I_{\text{molec}}^{0-n} = \frac{\lambda^{2n} e^{-\lambda^2}}{n!}. \quad (3.4)$$

This relation is in disagreement with the data that is presented in Figs.3.1(b) and 3.2(b), where we observe a significant decrease in the PL 0-2/0-1 ratio (decrease in  $\lambda_{\text{eff}}^2$ ) with increasing  $M_w$ . More precisely,  $\lambda_{\text{eff}}^2$  decreases from approximately 1.3-1.6 for P3HT of low  $M_w$  to 1.0-1.1 for materials of high  $M_w$ . The apparent failure of the H-aggregate model, which assumes that a polymer chain has a unique HR factor independent of  $M_w$ , is due to its assumption that a single chain can be modeled as a two-level chromophore with displaced harmonic nuclear potentials characterized by a unique HR factor  $\lambda^2=2$ . This simple description assumes that the Born-Oppenheimer approximation is valid for a single chain and ignores exciton motion and nonadiabatic coupling to vibrations within a given chain. The consequences of intrachain exciton vibrational coupling were examined in Ref. [49], where a single conjugated polymer chain was modeled as a one-dimensional Wannier ex-

citon coupled vibronically to the main symmetric vinyl-stretching mode. The electron and hole transfer integrals between neighboring unit cells were taken to have the same sign, consistent with what is normally assumed for conjugated polymer chains, and reflective of a direct bandgap semiconductor. The ensuing photophysical properties of such 'quantum wires' were found to be remarkably similar to linear J-aggregates. [98] In Ref. [49] it was shown that the 0-0/0-1 line strength ratio in the PL spectrum of the single chain increases with intrachain exciton bandwidth – as expected for a J-aggregate – while the 0-2/0-1 ratio decreases. The behavior can be crudely described as a decrease in the effective single chain Huang-Rhys factor with increasing exciton coupling, although the relative intensities are generally not Poissonian. An approximate description of this behavior in the adiabatic limit was provided by Chen and coworkers for a Frenkel chain, [99] as well as Cornil et. al. for a polymer chain using quantum chemically derived adiabatic ground and excited state potentials. [100]

We therefore attribute the decrease in  $\lambda_{\text{eff}}^2$  that we observe in the P3HT samples of increasing  $M_w$  to an increase in the intrachain exciton bandwidth. This strongly suggests that in these high- $M_w$  P3HT architectures, the macromolecules are of reduced torsional disorder. Such a transition to a more planar structure in samples of higher molecular weight would be in agreement with some of our thermal analysis data : indeed, we observe an increase in both the melting temperature,  $T_m$  (which is directly correlated with the lamellar crystal thickness) and the enthalpy of fusion,  $\Delta H_f$  (which is directly correlated with the degree of crystallinity ; see Koch et al. [19] and references therein).

Further support high- $M_w$  P3HT structures being of higher torsional order (i.e more pronounced planarization of the polymer backbones) can be evoked from the ratio of the PL decay at 1.90 eV and 1.77 eV (Fig.3.3c). We observe that in the low  $M_w$  -regime, the relaxation of the normalized ratio of intensities at these two photon energies is more significant than for high- $M_w$  material. In fact, Parkinson

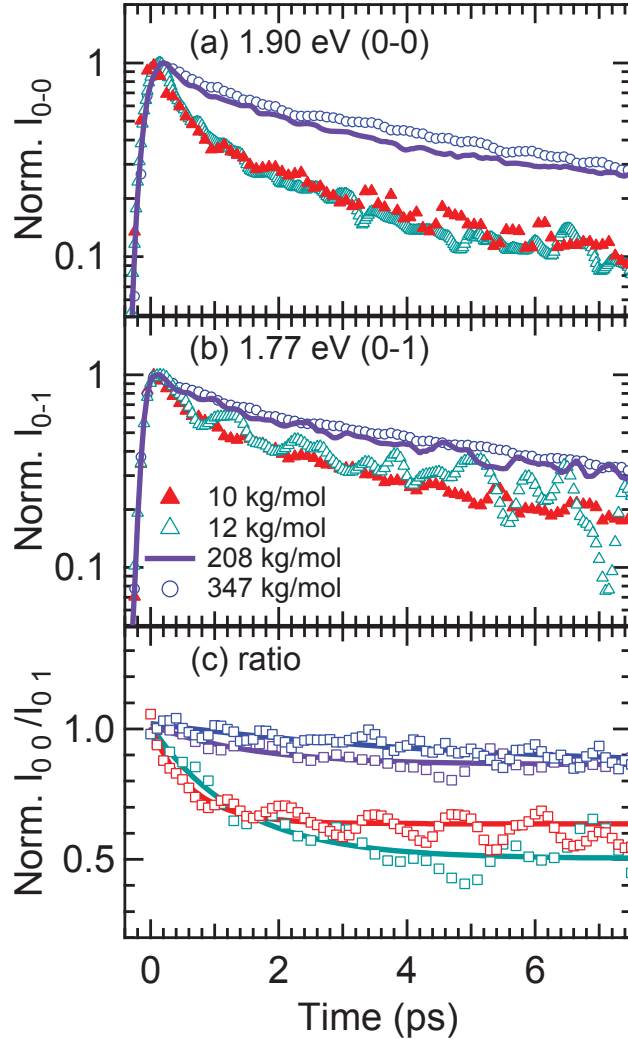


Figure 3.3 – (Color) Time-resolved photoluminescence measurements at room temperature. Time-dependent photoluminescence intensity measured at a photon energy of 1.77 eV(a) and 1.90 eV(b) for various samples of different molecular weight. The normalized ratio  $I_{0-0}/I_{0-1}$  is plotted in part (c).

et al. have reported that vibrational relaxation from a low-symmetry to a high-symmetry ordered state, characteristic of torsional planarization along the polymer backbone upon optical excitation, results in a dynamic decrease of the relative 0-0 PL intensity on a timescale  $\sim 13\text{ ps}$ . [72] Such effect has also been observed by Banerji et al. on timescales  $> 1\text{ ps}$ . [101] Moreover, recent broadband transient spectroscopy

measurements have revealed signatures of both small-scale ( $<1$  ps) and large scale ( $>1$  ps) planarization of P3HT thiophene units after excitation. [102] In other materials such as PPV oligomers, the degree of torsional angle of the backbone is found to correlate with an increase of the oscillator strength for the 0-0 transition in comparison to the rest of the vibronic replicas. [103] This is consistent with higher initial torsional order in the high  $M_w$  regime, which influences  $W$  and consequently  $\alpha$ , the relative intensity of the 0-0 peak in PL. From this observation, we support our conjecture that the decrease in  $\lambda_{\text{eff}}^2$  with increasing  $M_w$  is primarily due to an increase in intrachain exciton bandwidth resulting from a reduction in torsional disorder in high  $M_w$  aggregates.

### 3.6.2 The HJ-aggregate model

In order to obtain a more detailed knowledge about the relationship between exciton signatures and solid-state microstructure and macromolecular chain conformation, and to explore the effect of intrachain exciton bandwidth on  $\lambda_{\text{eff}}^2$  quantitatively, we generalize the HJ-aggregate model introduced in Ref. [59] to include disorder. In the HJ-aggregate model, excitons are free to navigate across chains in the  $\pi$ -stack, as in the original H-aggregate model, but also within chains. Intrachain excitons are generally of the Wannier-Mott type in which electrons and holes are bound across more than one site with a characteristic Bohr radius. Hence, within a  $\pi$ -stack of such chains, the exciton is delocalized over two dimensions ; along the polymer backbone as well as along the stacking axis. Because the Wannier-Mott excitons in one dimension lead to J-aggregate photophysics, [49] the aggregate can be understood as J-like along the backbone dimension and H-like along the stacking direction, allowing for interesting hybrid H-J photophysical properties. If disorder is absent, as was the case treated in Ref. [59], the high symmetry dictates that no 0-0 emission can occur at low temperatures - a classic signature of H-aggregates. Increasing temperature leads to interesting effects, for example, a transition from

H- to J-aggregate behavior with increasing temperature has been predicted. [59] Similar effects are expected when correlated disorder (quantified by  $\sigma$  and  $\beta$ ) is included.

In this Section we show that the intrachain and interchain exciton bandwidths corresponding to the emitting aggregate species can be determined entirely from an analysis of the PL vibronic progression; in particular from the 0-2/0-1 and 0-0/0-1 ratios. This has an advantage over some prior analyses based on the H-aggregate model where the (interchain) exciton bandwidth was extracted from the 0-0/0-1 absorption spectral ratio, which is characteristic of the absorbing species. In polymer films absorption and emission very likely take place from configurationally inequivalent species, as the significant disorder inherent to such films enhances spectral diffusion away from the primary absorbers.

In conjugated polymer chains the ratio of the 0-0 and 0-1 oscillator strengths in the absorption spectrum can be quite large - almost a factor of ten in the isolated and practically disorder-free polydiacetylene (PDA) chains, [92] for example - and is a direct measure of the strength of the intrachain exciton coupling. In modeling a single P3HT chain we assume weaker intrachain coupling than in PDA because the 0-0/0-1 absorption peak ratio in P3HT (in solution or solid phase) has never been observed to increase much beyond unity. In the weak coupling limit, second order perturbation theory shows that transport along the chain occurs via virtual two-step electron-hole (or vice versa) events involving Frenkel-like excitations within a single monomer unit (i.e. thiophene unit). [59] Such a chain can be described with a Frenkel-like Holstein Hamiltonian in which the (through-bond) exciton coupling between adjacent thiophene units is given by,

$$J_{\text{intra}} = \frac{-2t_e t_h}{|U - V_1|}. \quad (3.5)$$

Eq.3.5 contains the product of electron ( $t_e$ ) and hole ( $t_h$ ) transfer integrals

connecting neighboring thiophene LUMO's and HOMO's respectively.  $|U - V_1|$  is the stabilization of the neutral Frenkel-like exciton relative to the nearest-neighbor charge-separated state. Note that the single-chain physics is invariant to a sign change in both  $t_e$  and  $t_h$ . In addition to an effective coupling between adjacent thiophene units there is also a second-order energy (red) shift, given by

$$\Delta_{\text{intra}} = -\frac{2(t_e^2 + t_h^2)}{|U - V_1|} \quad (3.6)$$

due to virtual two-step transfer where, for example, an electron (or hole) moves to a neighbor and then returns to the parent thiophene ring.

As in Ref. [59], we assume equivalent electron and hole transfer integrals, and introduce  $t$  such that  $t_e = t_h$ . Having  $t_e = t_h$  is consistent with a direct bandgap semiconductor. Within this approximation Eq.3.5 leads to

$$J_{\text{intra}} = \frac{-2t^2}{|U - V_1|}, \quad (3.7)$$

where the negative sign on the right-hand side ensures J-aggregate-like behavior. Inserting  $t_e = t_h$  in Eq.3.6 leads to a simple relation between the red shift and  $J_{\text{intra}}$ ,

$$\Delta_{\text{intra}} = 2J_{\text{intra}}. \quad (3.8)$$

Since the P3HT chains are generally torsionally disordered, we consider  $t$  (and  $J_{\text{intra}}$ ) to be an *effective* coupling, smaller than the larger intrinsic coupling found in the "perfect" polydiacetylene chains. [49] Within the space of a single electronic excitation (one electron and one hole), the single-chain effective Hamiltonian representing the  $s^{th}$  disorder-free P3HT chain is therefore given by

$$\begin{aligned}
\hat{H}_s = \varepsilon_1 + \Delta_{intra} &+ \hbar\Omega_0 \sum_n b_{n,s}^\dagger b_{n,s} \\
&+ \hbar\Omega_0 \sum_n \left\{ \lambda_0 \left( b_{n,s}^\dagger + b_{n,s} \right) + \lambda_0^2 \right\} |n, s\rangle \langle n, s| \\
&+ J_{intra} \sum_n \{ |n, s\rangle \langle n+1, s| + |n+1, s\rangle \langle n, s| \}.
\end{aligned} \quad (3.9)$$

$|n, s\rangle$  represents an electron-hole(Frenkel-like) excitation ("S<sub>1</sub>") on the  $n^{th}$  thiophene unit of the  $s^{th}$  chain with energy  $\varepsilon_1$ . The operator  $b_{n,s}^\dagger$  ( $b_{n,s}$ ) creates (destroys) a vibrational quantum of energy,  $\hbar\Omega_0$ , (corresponding to the symmetric ring-stretching mode) in the ground state nuclear potential well (the "S<sub>0</sub>" potential) associated with a neutral "ground state" repeat unit at the  $n^{th}$  site on chain  $s$ . (Such a unit contains no electrons and holes). The quantity  $\lambda_0$  is the Huang-Rhys factor for an individual thiophene unit and is set to 2, which we calculate for uncoupled thiophene monomers by means of time-dependent density functional theory (see appendix.I).

Energetic site disorder within the  $s^{th}$  chain is represented by the Hamiltonian

$$H_{s,dis} = \sum_n \Delta_{n,s} |n, s\rangle \langle n, s|, \quad (3.10)$$

where  $\Delta_{n,s}$  is the transition frequency detuning of the  $n^{th}$  thiophene unit on the  $s^{th}$  chain. In what follows, we take the detunings,  $\Delta_{n,s}$ , to be Gaussian random variables distributed with probability,

$$P(\Delta_{n,s}) = \frac{1}{\sqrt{\pi}\sigma} e^{-\frac{\Delta_{n,s}^2}{\sigma^2}}. \quad (3.11)$$

Here,  $2\sigma$  is the full width of the distribution at  $1/e$  of the maximum. The spatial correlation length,  $\ell_0$ , is defined through an exponential drop in the intersite

correlation function, [60, 104]

$$\langle \Delta_{n,s} \Delta_{n',s'} \rangle = (\sigma^2/2) \exp \left[ -\sqrt{(n-n')^2 + (s-s')^2} / \ell_0 \right]. \quad (3.12)$$

Here,  $\ell_0$  is in units of  $d$ , where  $d \approx 4$  is the (approximate) distance between nearest-neighbor chains as well as the distance between nearest neighbor thiophene units within a given chain. The monomer units in a  $\pi$ -stack therefore constitute a square lattice with a spatial correlation radius given by  $\ell_0$ . As before (see discussion following Eq.3.3) the correlation parameter  $\beta$  is associated with  $\ell_0$  through,  $\beta = \exp(-1/\ell_0)$ . [104] In a more sophisticated treatment, the interchain and intrachain disorder included in Eq.3.12 can be distinguished by introducing spatial correlation lengths along and across the polymer backbone. However, as of the time of this writing we have no clear data to suggest what the anisotropy in the  $\ell_0$  values might be. Although increasing the value of  $\ell_0$  along a particular direction would enhance the coherence length along that direction, the effect is not large. (see Fig.3.9, which shows a remarkable stability of the coherence length to changes in the correlation length). Finally, we emphasize that the torsional disorder is also reflected in the mean intrachain coupling  $J_{\text{intra}}$ . In principle  $J_{\text{intra}}$  should be correlated to  $\ell_0$ . Here we treat them as independent variables but look for consistency in our final results (see below).

The complete Hamiltonian for the  $\pi$ -stack including disorder reads,

$$H_{\pi\text{-stack}} = \sum_s (\hat{H}_{s,\text{chain}} + H_{s,\text{dis}}) + \sum_s \sum_n J_{\text{inter}} \{ |n,s\rangle \langle n,s+1| + |n,s+1\rangle \langle n,s| \} \quad (3.13)$$

where the through-space, interchain coupling,  $J_{\text{inter}}$ , is limited to adjacent (same  $n$ ) thiophene units on neighboring chains. [59] Note that the H-aggregate model is recovered in the limit that  $J_{\text{intra}}$  is set to zero.

In order to derive the mean intramolecular coupling,  $J_{\text{intra}}$ , from the measured

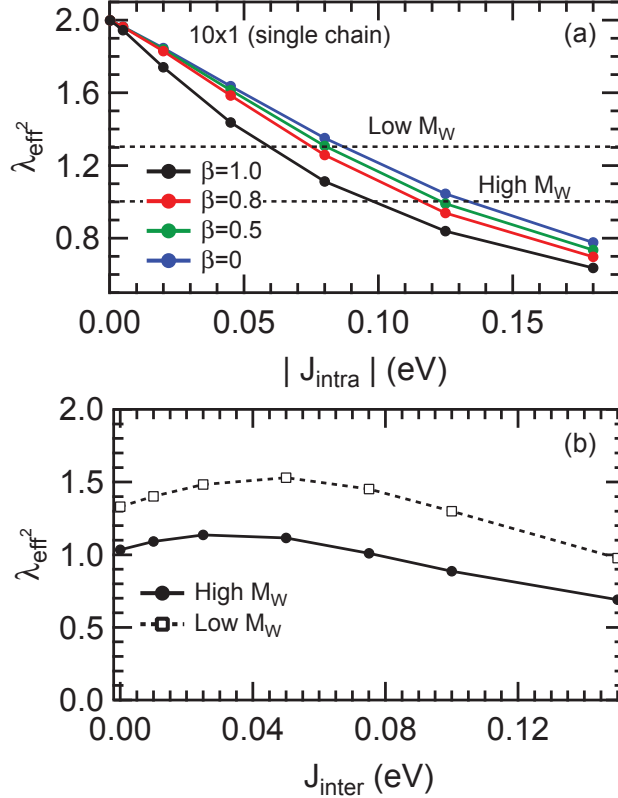


Figure 3.4 – (Color) Calculated effective Huang-Rhys parameter as a function of intramolecular and intermolecular coupling. (a)  $\lambda_{\text{eff}}^2$  as a function of  $J_{\text{intra}}$  for a single polymer chain containing 20 thiophene units with  $\lambda_0^2 = 2$ . Several disorder parameters  $\beta$  are shown, with  $\sigma = 0.54\hbar\omega_0$ . (b)  $\lambda_{\text{eff}}^2$  as a function of interchain coupling for 10 by 6 aggregates of high and low molecular weight chains with  $\beta = 0.6$ .

PL spectra we first introduce the effective HR factor, defined as,

$$\lambda_{\text{eff}}^2 \equiv 2 \frac{I_{PL}^{0-2}}{I_{PL}^{0-1}}, \quad (3.14)$$

where  $I_{PL}^{0-v}$  is the line strength corresponding to the  $0 - v$  transition. As we will show, the effective HR factor defined by Eq.3.14 is far more sensitive to the *intrachain* exciton bandwidth than the interchain exciton bandwidth, thereby providing an effective measure of the former. (By contrast, the ratio,  $I_{PL}^{0-0}/I_{PL}^{0-1}$ , responds to the exciton *coherence number* due to the competition between the intrachain and

interchain exciton coupling.)

In the limit of just a single, site-disordered chain with  $J_{\text{intra}} = 0$  (i.e. a linear array of noninteracting thiophene units)  $\lambda_{\text{eff}}^2$  reduces to the monomeric HR factor  $\lambda_0^2$ , (which we take to be two), as can be appreciated from the Poissonian distribution in Eq.3.3. Increasing  $|J_{\text{intra}}|$  enhances the J-aggregate behavior : the 0-0/0-1 line strength ratio in PL spectrum increases in response to the increasing exciton coherence length, while the 0-2/0-1 ratio decreases. The overall result is a decrease in the effective HR factor. The effect is shown in Fig.3.4 for several values of the disorder correlation parameter,  $\beta$ , with the value of  $\sigma$  taken from the absorption spectral line widths of the high- $M_w$  films when fitted to a Gaussian line shape. ( $\sigma$  is the half-width at  $1/e$  of the maximum). From Fig.3.1(a) we have  $\sigma=0.6\omega_0$  and  $\sigma=0.54\omega_0$ , for the low and high  $M_w$  samples, respectively. Fig.3.4 shows that  $\lambda_{\text{eff}}^2$  decreases markedly with increasing intrachain coupling, as expected for J-aggregates.

After removing the cubic frequency dependence and the index of refraction dependence from the measured PL spectra in Fig.3.1b, the experimentally-obtained values of  $\lambda_{\text{eff}}^2$  were determined to be approximately 1.5 for the low  $M_w$  materials and 1.1 for P3HT of high  $M_w$ . However, in our modeling of a single chain, we take the slightly smaller values of 1.3 and 1.0, for the low- and high- $M_w$  films, respectively, since, as will be shown shortly, the values increase slightly when interchain effects are included. Fig.3.4 shows that  $\lambda_{\text{eff}}^2$  attains the value of near unity observed in films of P3HT of high  $M_w$  when  $|J_{\text{intra}}|$  is in the range, 0.1-0.15 eV, while the value observed for low- $M_w$  material is consistent with values of  $|J_{\text{intra}}|$ , some 30% smaller.

Fig.3.4(b) shows how  $\lambda_{\text{eff}}^2$  varies with interchain coupling,  $J_{\text{inter}}$ , for the two values of  $|J_{\text{intra}}|$  which reproduce the measured effective HR factors for low and high  $M_w$ -materials for a representative value of  $\beta=0.6$ . (Other values of  $\beta$  give qualitatively similar behavior). The dependence on  $J_{\text{inter}}$  is much weaker than the dependence on  $|J_{\text{intra}}|$ , although there is a slight but significant initial rise in  $\lambda_{\text{eff}}^2$

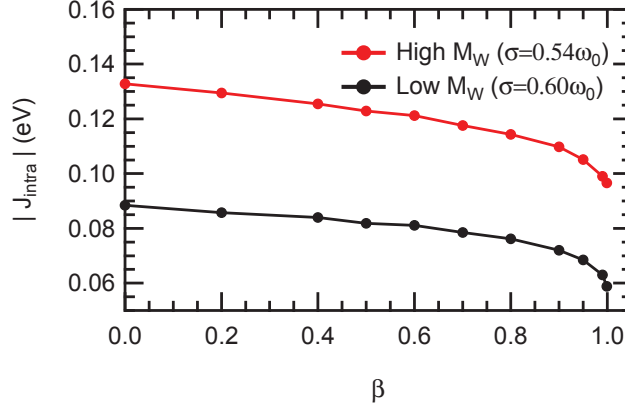


Figure 3.5 – Values of  $(\beta, J_{\text{intra}})$  for which the effective HR factor,  $\lambda_{\text{eff}}^2$  is constant at 1.0 and 1.3 for single (isolated) chains of low and high  $M_w$ , respectively. Each chain contains 10 thiophene rings (sufficient for convergence) and the ensemble average included  $10^4$  configurations. For the low (high)  $M_w$  chains the value of  $\sigma$  is  $0.6\omega_0$  ( $0.54\omega_0$ ) as determined from the absorption spectral line widths

with  $J_{\text{inter}}$ , followed by a peak and subsequent demise. The weak dependence of  $\lambda_{\text{eff}}^2$  on interchain interactions was shown analytically using the H-aggregate model in Ref. [66] and demonstrated numerically in Ref. [60]. The weak dependence is therefore due to the positive sign of the interchain coupling.

Fig.3.4(a) and (b) also show that  $\lambda_{\text{eff}}^2$  serves as an effective probe of the *intrachain* exciton bandwidth and disorder parameter  $\beta$ . Armed with the measured value of  $\lambda_{\text{eff}}^2$  for the low and high  $M_w$  films (1.3 and 1.0, respectively) we then determined the points  $(\beta, J_{\text{intra}})$  which reproduce the measured  $\lambda_{\text{eff}}^2$  in an ensemble of disordered single chains containing 10 thiophene units each. (Ten units are enough to ensure convergence to the polymer limit.) The results are plotted in Fig.3.6 for both low- and high- $M_w$  films. Our results show that generally slightly larger values of  $J_{\text{intra}}$  are required when disorder is increased ( $\beta$  reduced) and that the low- $M_w$  films have uniformly lower values of  $|J_{\text{intra}}|$  than films prepared with high- $M_w$  materials, consistent with increased torsional disorder in the low- $M_w$  films.

We next turn to the effects of interchain coupling. To this end, we first took

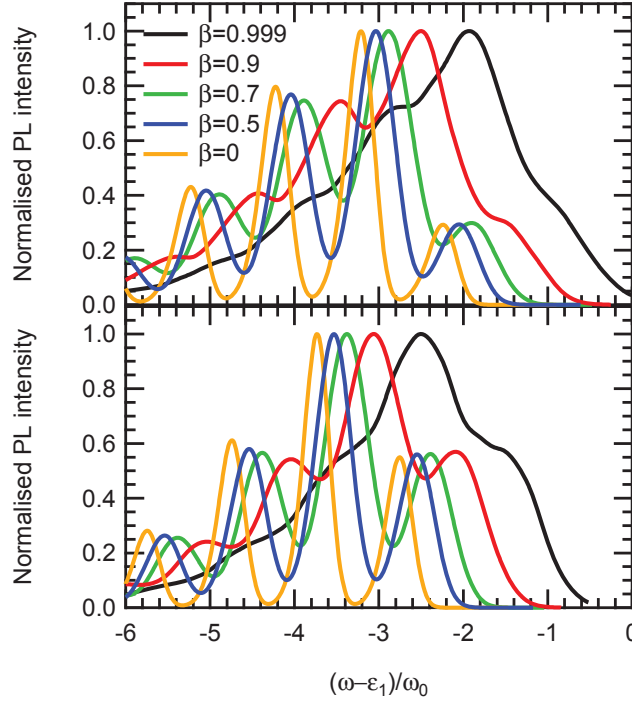


Figure 3.6 – Calculated PL spectra for selected triple points from Table.3.I for materials of molecular weights in the low (a) and high  $M_w$  (b) limits. Ensemble averaging includes  $10^4$  configurations of disorder.  $T=10K$

representative points on the curves in Fig.3.4 and varied  $J_{\text{inter}}$  for each one until the calculated 0-0/0-1 ratio in the PL spectrum matched the measured values. Unlike  $\lambda_{\text{eff}}^2$ , the 0-0/0-1 PL ratio is extremely sensitive to exciton spatial coherence [56, 60] and depends in a complex way on the exciton coupling along and across chains. [59] For the two featured P3HTs of low (12.4 kg/mol) and high (264 kg/mol)  $M_w$ , the 0-0/0-1 ratios were approximately 0.3 and 0.55, respectively, after removal of the cubic frequency dependence and index of refraction dependence. The values of  $J_{\text{inter}}$  which maintain the measured 0-0/0-1 PL ratio are shown in Table.3.I. Ideally, if interchain interactions had no impact on  $\lambda_{\text{eff}}^2$ , all of the "triple points" ( $\beta$ ,  $J_{\text{intra}}$ ,  $J_{\text{inter}}$ ) in Table.3.I would reproduce both the measured 0-2/0-1 and 0-0/0-1 ratios in the PL spectrum. Table.3.I shows that  $\lambda_{\text{eff}}^2$  increases with the disorder as anticipated

from Fig.3.2. The increase, however, is quite modest and within the experimental error bars for both low- and high- $M_w$  samples (1.5 and 1.1, respectively) when  $\beta > 0.5$ .

		High Mw				Low Mw			
$\beta$	$\ell_0$	$ J_{\text{intra}} $	$ J_{\text{inter}} $	$I^{0-0}/I^{0-1}$	$\lambda_{\text{eff}}^2$	$ J_{\text{intra}} $	$ J_{\text{inter}} $	$I^{0-0}/I^{0-1}$	$\lambda_{\text{eff}}^2$
0	0.0	0.133	0.045	0.56	1.24	0.088	0.085	0.3	1.62
0.2	0.6	0.129	0.041	0.56	1.21	0.086	0.078	0.3	1.60
0.4	1.1	0.126	0.035	0.56	1.18	0.084	0.069	0.3	1.56
0.5	1.4	0.123	0.032	0.56	1.17	0.082	0.065	0.3	1.54
0.6	2.0	0.121	0.030	0.56	1.14	0.081	0.061	0.3	1.51
0.7	2.8	0.117	0.028	0.56	1.13	0.078	0.055	0.3	1.50
0.8	4.5	0.114	0.024	0.56	1.10	0.076	0.048	0.3	1.46
0.9-	9.5	0.110	0.020	0.56	1.07	0.072	0.039	0.3	1.42
0.95	19.5	0.105	0.015	0.56	105	0.068	0.030	0.3	1.39
0.99	99.5	0.099	0.008	0.56	1.03	0.063	0.016	0.3	1.34
0.999	999.5	0.097	0.003	0.56	1.01	0.058	0.006	0.3	1.32

Tableau 3.I – Values of  $\beta$  and  $|J_{\text{intra}}|$  (eV) from fig.3.5 along with values of  $|J_{\text{inter}}|$  (eV) which maintain the 0-0/0-1 PL ratio at 0.56 in films of high- $M_w$  P3HT and 0.30 in low- $M_w$  films.

Table.3.I shows that as disorder increases (and  $\ell_0$  diminishes) both  $|J_{\text{intra}}|$  and  $J_{\text{inter}}$  also increase in order to keep the 0-0/0-1 ratio constant.  $J_{\text{inter}}$  increases by more than an order of magnitude over the full disorder range reported in the Table.3.I, far greater than the modest increase of only 30% for  $|J_{\text{intra}}|$ . The main reason for the large increase in  $J_{\text{inter}}$  is to counter the enhancement of the 0-0/0-1 ratio due to the symmetry breaking induced by increasing disorder.

Calculated PL spectra for selected triple points are shown in Fig.3.6, assuming that emission takes place from a Boltzmann distribution of band-bottom excitons, i.e. after relaxation has taken place. [59] The evaluation of the PL spectrum from a thermal population of exciton emitters is outlined in Ref. [59]. Here we perform an additional averaging over many ( $10^4$ ) realizations of spatially-correlated disorder consistent with  $(\sigma, \ell_0)$ . Figure 3.6 shows that the 0-0/0-1 ratio is constant throughout the series, whereas the 0-2/0-1 ratio exhibits the aforementioned slight

rise as disorder increases. The line widths significantly red-shift and narrow with increasing disorder due to a statistical effect discussed in detail in Ref. [60]. Essentially, the probability of finding a low-energy emitting trap increases when the spatial correlation length  $\ell_0$  is smaller ( $\beta$  smaller). Comparison with the experimental linewidths for films of low- and high- $M_w$  P3HT(see Fig. 1) suggests that  $\beta$  is in the range,  $0.5 < \beta < 0.9$ , equivalent to a correlation length in the range,  $1 < \ell_0 < 10$ . The measured spectra of Fig.3.1(b) further show that the 0-0 transition energies of the low- and high- $M_w$  samples are approximately the same. To obtain spectrally-aligned 0-0 peaks in the PL spectra in Fig.3.6 requires  $\beta$  to be larger in the higher  $M_w$  samples ; for example, when  $\beta=0.9$  in the high  $M_w$  films and  $\beta=0.5$  in the low- $M_w$  films the positions of the 0-0 peaks are roughly the same. This is consistent with films of P3HT of low  $M_w$  featuring a higher degree of energetic disorder.

We now turn to the temperature dependence of the 0-0/0-1 ratio. The measured temperature dependence is shown in Fig.3.7 for P3HT of low (12 kg/mol) and high (264 kg/mol)  $M_w$  , alongside the calculated temperature dependence for the selected triple points from Table.3.I. The temperature dependence was evaluated by performing a Boltzmann average over emitting excitons for each disordered chain in the ensemble. When disorder within each chain is minimal ( $\beta>0.95$ ) the form of the calculated temperature dependence is similar to what was derived in Ref. [59] in the limit of no disorder. The initial increase with  $T$  is a result of increasing population of the optically allowed higher energy exciton, as occurs in interchain H-aggregates. The peak occurs when  $kT$  is approximately equal to the interchain splitting, and the subsequent demise is the expected behavior for J-aggregates. When disorder increases, the temperature dependence flattens out considerably and better agrees with the measured trend, as depicted in Fig.3.7. Comparison of calculated and measured data show that the spatial correlation parameter  $\beta$  is most likely less than approximately 0.7 in both low and high molecular weight samples.

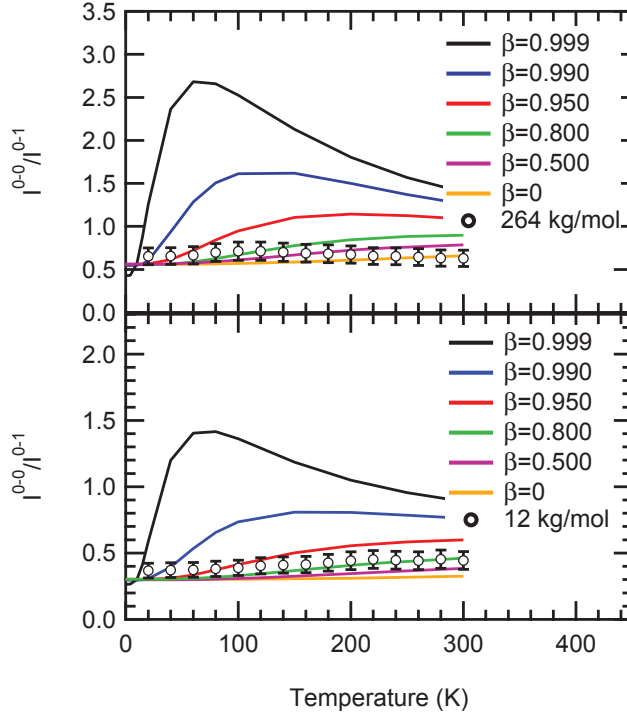


Figure 3.7 – The 0-0/0-1 PL ratio as a function of temperature for selected triple points (see Table.3.I) for P3HT thin films of high and low  $M_w$ . Also shown is the experimental data for the 447 kg/mol film (a) and 8 kg/mol (b) at T=10K

### 3.6.3 Exciton coherence

In what follows we will consider exciton coherence within the two-dimensional P3HT  $\pi$ -stacks. We are primarily interested in the exciton coherence corresponding to the thermally relaxed distribution of excitons which gives rise to the steady-state PL spectrum. The corresponding coherence length is limited by the localizing influences of disorder, vibronic coupling and increasing temperature. We are not concerned with the early-time evolution of exciton coherence during relaxation/thermalization which is driven by inhomogeneous and homogeneous dephasing. The latter is due to interactions between the  $\pi$ -stack and the surrounding bath, arising, for example, from lattice phonons. Due to the inherent anisotropy of exciton coupling in P3HT  $\pi$ -stacks we expect the coherence length along the

polymer backbone,  $L_{//}$ , and along the stacking axis,  $L_{\perp}$ , to differ. Moreover, as we will show, both coherence lengths depend on the polymer molecular weight.

For a thermal distribution of low-energy excitons responsible for emission and transport the ensemble-averaged coherence function is given by [60, 105]

$$\bar{\mathbf{C}}(\mathbf{r}) \equiv \left\langle \langle \psi^{(em)} | \sum_{\mathbf{R}} \mathbf{B}_{\mathbf{R}}^\dagger \mathbf{B}_{\mathbf{R}+\mathbf{r}} | \psi^{(em)} \rangle \right\rangle_{C,T} \quad (3.15)$$

where  $\mathbf{B}_{\mathbf{R}}^\dagger \equiv |\mathbf{R}; vac\rangle \langle g; vac|$  creates an exciton at the monomer site  $\mathbf{R}$  with no vibrational quanta (*vac*) relative to the ground state unshifted potential well. Here, the vector  $\mathbf{R}=(n,s)$  locates the  $n^{th}$  monomer repeat unit on the  $s^{th}$  chain.  $\langle \dots \rangle_{C,T}$  represents a dual configurational and thermal average, the former taking place over the various realizations of site-energy disorder and the latter taking place over a Boltzmann distribution of emitting excitons within each realization of disorder. The  $\mathbf{r}$ -dependent coherence in Eq.3.15 is similar to that used by Mukamel and coworkers [88, 106, 107] and Kuhn and Sundstrom. [87]

Coherence in P3HT using the H-aggregate model was investigated in Ref. [60]. As the H-aggregate model is one-dimensional, only the coherence along the  $\pi$ -stacking direction was considered. It was shown that in such aggregates the coherence function oscillates along the aggregate axis, changing sign as  $(-1)^n$ , where  $n$  labels the  $n^{th}$  polymer in the stack. The oscillation reflects the dominant admixture of the high wave vector ( $k = \pi$ ) exciton in the band-bottom excitons, as is characteristic of disordered H-aggregates. [60] By contrast, in linear J-aggregates the coherence function is nodeless, reflecting the dominant admixture of the  $k = 0$  exciton in the band-bottom excitons. [97]

Fig.3.8 shows the two-dimensional coherence functions for films of high- and low- $M_w$  P3HT evaluated from Eq.3.15 using  $\beta = 0.6$ , with the coupling parameters taken from Table.3.I. Interestingly, the coherence function contains properties of H- and J-aggregation : the oscillations along the  $\pi$ -stacking direction results from the

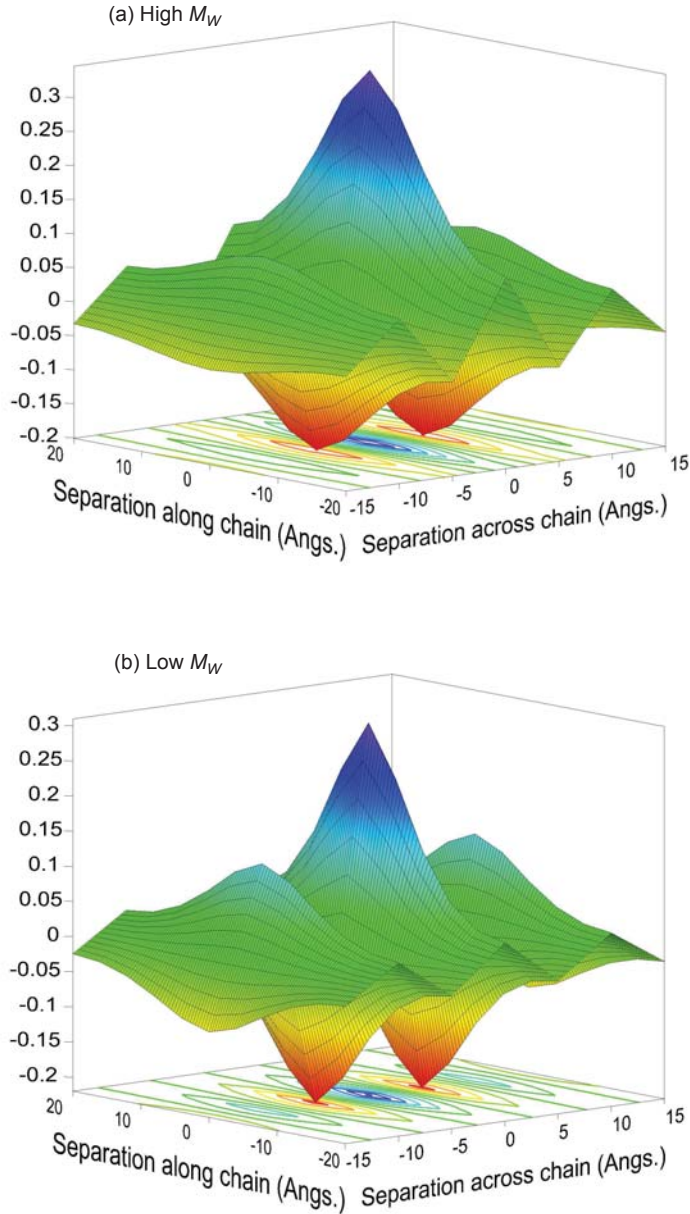


Figure 3.8 – Coherence function from Eq.3.15 for low- and high- $M_w$  samples and  $\beta = 0.6$ . Calculations are conducted on 6 by 10 aggregates (6 chains each containing 10 thiophene rings).

positive sign of the interchain coupling and signals H-aggregation, while the uniform phase of along the chain direction results from the negative sign of the intrachain interactions and signals J-aggregation. Fig.3.8 shows that the coherence has greater

extent along the polymer chain for P3HT of higher  $M_w$  where the intrachain coupling is about 50% larger than in the low- $M_w$  materials (see Table.3.I). Although not as obvious, the opposite holds for the coherence along the  $\pi$ -stacking axis; it has a greater extent for films prepared with low- $M_w$  materials, where the interchain coupling is twice as large compared with P3HT of higher  $M_w$  (see Table.3.I). Fig.3.8 also shows that the coherence function is more anisotropic in the higher-  $M_w$  films.

Based on the coherence function in Fig.3.8 one can approximate the total number of monomeric units,  $N_{coh}$ , within the coherence "area" defined by the spatial extent of the envelope of the coherence function. A more quantitative evaluation of  $N_{coh}$  follows from the simple relation, [60, 97]

$$N_{coh} = \bar{C}(0)^{-1} \sum_{\mathbf{r}} |\bar{C}(\mathbf{r})| \quad (3.16)$$

where the dimensionless vector  $\mathbf{r}$  runs over all monomer-monomer separation vectors within the  $\pi$ -stack. The absolute value dependence on eliminates the phase oscillations, since  $N_{coh}$  depends on the envelope of  $\bar{C}(\mathbf{r})$ . For example, in a linear H-aggregate that is fully coherent (so that  $N_{coh} = N$ ) the oscillations present in  $\bar{C}(\mathbf{r})$  lead to complete destructive interference in the sum,  $\sum_{\mathbf{r}} \bar{C}(\mathbf{r})$ , making it necessary to instead sum over  $\sum_{\mathbf{r}} |\bar{C}(\mathbf{r})|$  in order to determine  $N_{coh} = N$ . Indeed, the sum in Eq.3.16 gives the correct result,  $N_{coh} = N$  (assuming, as we are, periodic boundary conditions).

The coherence number defined in Eq.3.16 has the correct limiting behaviors, ranging from unity when the coherence function is fully localized ( $\bar{C}(\mathbf{r}) = \bar{C}(0)\delta_{r,0}$ ) to  $N$  when the coherence is spread over the entire aggregate.  $N_{coh}$  differs from previously defined measures of exciton coherence sizes, [86] such as the inverse participation ratio. The advantage of our definition is the simple and direct relationship  $N_{coh}$  has to the exciton superradiant enhancement and, more importantly, to the 0-0/0-1 PL ratio in J-aggregates (see below).

The coherence number  $N_{coh}$  depends mainly on the nature of disorder ( $\sigma, \ell_0$ ) as well as the temperature. Generally, increasing disorder and/or temperature localizes excitations and reduces  $N_{coh}$  as demonstrated in detail in Refs. [60] and [97] for H and J-aggregates, respectively. Vibronic coupling is also important since it weakens the excitonic coupling, thereby allowing the disorder-induced localization to be more effective. Using Eq.3.16 we find that  $N_{coh}$  is  $\approx 16$  for the low- $M_w$  P3HT films of Fig.3.8(b) and  $\approx 18$  for the high- $M_w$  films of P3HT of Fig.3.8(a). Since the temperature is low ( $T = 10$  K) it is disorder that is mainly responsible for localizing exciton coherence in both P3HT of low and high- $M_w$ .

In the  $\pi$ -stack, one can also define the coherence *lengths* along the polymer chain direction ( $L_{//}$ ) and along the  $\pi$ -stacking axis ( $L_{\perp}$ ) from the coherence function via,

$$L_{//} = d_{//} \left\{ \bar{C}(0)^{-1} \sum_{\mathbf{r} \in Chain} |\bar{C}(\mathbf{r})| - 1 \right\} \quad (3.17a)$$

$$L_{\perp} = d_{\perp} \left\{ \bar{C}(0)^{-1} \sum_{\mathbf{r} \in ChainNormal} |\bar{C}(\mathbf{r})| - 1 \right\}, \quad (3.17b)$$

where  $d_{//}$  ( $d_{\perp}$ ) is the nearest neighbor distance between two adjacent thiophene units within a chain (on neighboring chains). As stated earlier we take both distances to be 4.0 Å in our calculations. Note that the term  $\mathbf{r}=0$  is included in both sums of Eq.3.17(a),(b). Also note that in the limit of strong localization where  $\bar{C}(\mathbf{r}) = \bar{C}(0)\delta_{r,0}$  the coherence lengths properly tend to zero.

Based on the coherence functions in Fig.3.8 and the use of Eqs.3.17(a),(b), the coherence lengths along the polymer backbone and along the stacking axis are calculated in a 6 by 10 aggregate (6 chains with 10 thiophene units per chain). Fig.3.8 shows the coherence lengths of the low and high- $M_w$  materials for each of the triple points of Table.3.I. The coherence size is remarkably stable throughout the range from  $\beta=0$  to 0.95, corresponding to the spatial correlation length ranging

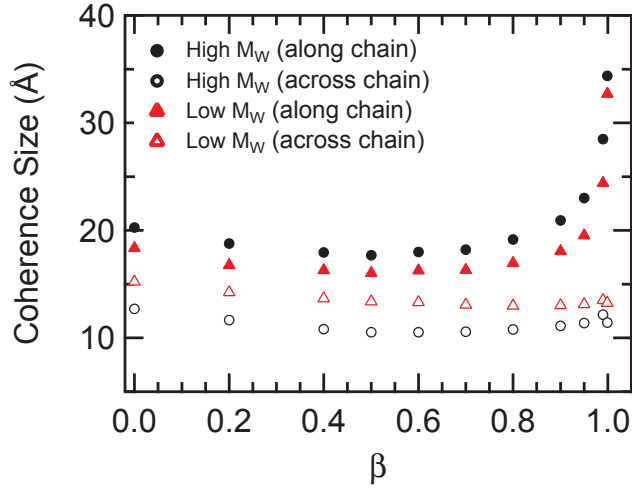


Figure 3.9 – Coherence size defined in Eq.3.17 as a function of disorder parameter,  $\beta$ , for P3HT films of low and high  $M_w$  at  $T=10K$ . Each point corresponds to triple point of Table.3.I. Calculations are conducted on 6 by 10 aggregates (6 chains each containing 10 thiophene rings).

from  $\ell_0 = 0$  to 20 thiophene units. The coherence length begins to significantly increase when  $\ell_0$  exceeds the chain length (10 units) used in the calculation; we therefore suspect that using larger chains in our calculations would lead to an increase in the range of  $\ell_0$  over which the coherence lengths remain approximately constant. When  $\beta=1$  each repeat unit in a given aggregate has essentially the same transition frequency, i.e., the intra-aggregate disorder is zero. Considering the 6 by 10 aggregates used on our calculations, the coherence length along the chain approaches  $9d=36\text{ \AA}$ , as is observed in Fig.3.8. The coherence length across the chains should approach  $5d = 20\text{ \AA}$ , however in this limit the small interchain interaction is of the order of  $kT$  at  $T=10\text{ K}$  ( $J_{\text{inter}} = 0.003\text{ eV}$  from Table.3.I) so that the thermally-induced localization remains significant. From Fig.3.8, the coherence length along the chain for P3HT of high  $M_w$  is about  $18\text{ \AA}$  (maintaining  $\beta=0.6$ ) which corresponds to slightly greater than four thiophene units. The coherence length drops to about  $7.5\text{ \AA}$  across chains. In materials of low  $M_w$  the coherence is

more isotropic ; the coherence length along the chain is about 25% smaller than for high- $M_w$  P3HT, although the coherence length across chains is significantly higher, approximately 10 Å, which is only slightly smaller than the value of  $\approx 12$  Å obtained using the H-aggregate model in Ref. [60]. The greater coherence length along the chain for P3HT of high  $M_w$  is consistent with reduced torsional disorder while the larger coherence length across chains for materials of low  $M_w$  arises mainly from the much higher interchain interactions ( $J_{\text{inter}}$ ) within the  $\pi$ -stacks of these materials (see Table.3.I), possibly due to the higher torsional disorder in such structures, e.g. induced through end-group effects.

### 3.6.3.1 Relationship between $N_{coh}$ and the PL line shape

We have written extensively on the uniquely coherent nature of the 0-0 peak within the PL vibronic progression. [56, 75, 97] For any aggregate type (H and J) the dimensionless 0-0 line strength is directly related to the averaged coherence function through,

$$I_{PL}^{0-0} = \sum_{\mathbf{r}} \bar{C}(\mathbf{r}) \quad (3.18)$$

In the case of J-aggregates, where  $\bar{C}(\mathbf{r})$  is uniformly positive, the 0-0 peak is a direct measure of the coherence size and is the source of superradiance (see Eq.3.16 with  $|\bar{C}(\mathbf{r})| = \bar{C}(\mathbf{r})$ ). Since the side-band line strengths are largely incoherent, the ratio  $I_{PL}^{0-0}/I_{PL}^{0-1}$  is useful for probing coherence. In Ref. [97] we obtained the simple relationship (for a linear J-aggregate),

$$I_{PL}^{0-0}/I_{PL}^{0-1} \approx N_{coh}/\lambda^2. \quad (3.19)$$

Eq.3.18 provides a simple means of extracting  $N_{coh}$  directly from the PL spectrum in J-aggregates. [49, 97]

In marked contrast, in H-aggregates the 0-0 intensity (as well as ratio  $I_{PL}^{0-0}/I_{PL}^{0-1}$

) is not directly proportional to the coherence number because the phase oscillations in  $\tilde{C}(\mathbf{r})$  lead to destructive interferences in  $I_{PL}^{0-0}$  (see Eq.3.18) but not in  $N_{coh}$  (see Eq.3.16). As a result, in H-aggregates the PL ratio is inversely related to  $N_{coh}$ , decreasing with increasing  $N_{coh}$  as the destructive interference between chains become more effective. [60] In the limit of maximum coherence ( $T=0$  K and  $\sigma=0$  or  $\ell_0=\infty$ )  $N_{coh}$  becomes equal to  $N$  and the PL ratio vanishes in H-aggregates - there is no 0-0 peak by symmetry. By contrast, in the same limit the PL ratio is maximized ( $=N/2$ ) in J-aggregates. Hence, for H-aggregates, there is no simple relationship relating the PL ratio to  $N_{coh}$ . Expressions like Eq.3.3 imply that  $N_{coh}$  is a complex function of the exciton bandwidth, disorder, and the vibronic coupling. However, once a model for disorder is assumed,  $N_{coh}$  can be determined numerically from the measured PL ratio as was done in Ref. [60] Hence, for either aggregate type (H or J)  $I_{PL}^{0-0}/I_{PL}^{0-1}$  provides a means of determining  $N_{coh}$ .

In the  $\pi$ -stacks of interest here, the PL ratio is enhanced by the coherence along the polymer chain as the transition dipoles of the repeat units are aligned in-phase. However, between chains there is a phase shift (see Fig.3.9) which causes destructive interference between the chains. Hence, the H-like interchain character leads to an attenuation of the ratio  $I_{PL}^{0-0}/I_{PL}^{0-1}$ . In the presence of disorder and thermal fluctuations the overall PL ratio is therefore due to a competition between intrachain, J-favoring interactions and interchain, H-favoring interactions. As we have shown here in P3HT films the competition is also a function of the chain conformation dictated by the material's molecular weight, with the most influential factor being the diminished interchain coupling (and enhanced intrachain coupling) experienced by the more planar (torsionally less disordered) macromolecules of P3HT of higher  $M_w$ .

### 3.7 Discussion

From the work presented in Section 3.6.1, we identify a clear microstructure-dependent interplay of intermolecular and intramolecular exciton spatial coherence in neat regioregular P3HT, which we rationalize in terms of a hybrid HJ-aggregate model. We can summarize the important conclusions as follows : (i) the photo-physics of P3HT films results from a competition of intrachain  $\pi$ -electron coupling (J-aggregate-like behavior), and interchain Coulombic coupling (H-aggregate behavior); (ii) while the ratio of the 0-0 and 0-1 PL intensities is sensitive to interchain exciton coherence, the 0-2/0-1 ratio in the PL spectrum is predominantly an intrachain property that determines the effective single-chain Huang-Rhys factor  $\lambda_{\text{eff}}^2$  (see eq.3.13). The measured change in  $\lambda_{\text{eff}}^2$  from near unity in P3HT samples of high  $M_w$  to approximately 1.3-1.5 in low- $M_w$  materials reflects greater intrachain coupling in P3HT of high  $M_w$ , which we attribute to reduced torsional disorder; (iii) the enhanced 0-0/0-1 PL ratio in films of P3HT of higher  $M_w$  is mainly due to decreased interchain couplings which correlate to longer conjugation lengths (and coherence lengths) within the chains. Enhanced intrachain coupling also favors a larger 0-0/0-1 PL ratio. (iv) for both P3HT of high and low  $M_w$ , the coherence length is larger along the chain than across chains, but the coherence lengths do not dramatically differ between material of low and high  $M_w$ . We expect that the interplay between inter- and intrachain interactions is a general property in polymeric semiconductors. For instance, Köhler et al. recently presented convincing evidence of a second-order phase transition in MEH-PPV dissolved in methyltetrahydrofuran, [74] where the disordered "blue-phase" is converted to the aggregate "red-phase" as the temperature is lowered through the critical temperature near 200 K. In contrast to the PL line shape of the P3HT film aggregates studied here, the PL spectrum from red-phase MEH-PPV aggregates is dominated by the 0-0 transition, indicative of J-aggregate like behavior resulting from dominant intra-

chain interactions. In fact, the spectra closely resemble the PL spectra obtained from the P3HT whiskers of Niles et al., [73] the optical behavior of which were also rationalized in the same way. It is not fully understood why the optical properties of P3HT films cast from organic solvents under ambient conditions should more closely resemble H-aggregates, but the work here supports the hypothesis that such aggregates are comprised of chains with more torsional disorder, shorter conjugation lengths, and therefore stronger interchain interactions. The correlation between increased intrachain spatial coherence and reduced interchain coupling is consistent with the well-known oligomer length effect : the longer the oligomer the weaker are the interchain excitonic coupling. [53, 57, 95]

The solid-state microstructures formed over the wide molecular weight range studied in this work are very distinct, ranging from a one-phase, chain extended (paraffinic-like) structure to a two-phase semicrystalline morphology, [19] and the absorbance and PL spectral line shapes vary accordingly (Figs.3.1 and 3.2). It is striking that while field-effect mobilities [19, 30, 81, 83, 108] time-of-flight mobilities, [19, 84] and microwave conductivities [18] all display marked dependence on microstructure, the two-dimensional equilibrium exciton spatial coherence function derived from analysis of the PL spectral lines shape varies in a modest way over the same range (Figs.3.8,3.9). This reflects the strong Frenkel-like character of excitons in P3HT, which, together with the strong coupling to vibrational degrees of freedom and the substantial amount of configurational disorder intrinsic in these semicrystalline microstructures, results in fairly strong localization. From Fig.3.8 we obtain a coherence "area" - defined as the product of the two coherence lengths in Eq.'s3.17(a),(b) - of roughly  $130 \text{ \AA}^2$  for both low- and high- $M_w$  materials, with P3HT of high  $M_w$  being slightly more anisotropic ("rectangular"). We have focused mainly on the steady-state exciton coherence, although our time resolved results in Fig.3.3 indicate that for time windows beyond the  $\sim 200 \text{ fs}$  time resolution of our experiment, the spatial coherence properties do not change significantly in P3HT

of high  $M_w$ . In contrast, the significant reduction in the PL 0-0/0-1 ratio with time over the first 5-10 ps in materials of low  $M_w$  is consistent with an increasing coherence domain size with time due to planarization of the more torsionally disordered P3HT chains. [100] Interestingly, Banerji et al. reported that in films based on P3HT of  $M_w = 79.9$  kg/mol, this relaxation of the 0-0 intensity on picosecond timescales takes the system from a predominantly J-like emission spectrum (the 0-0 peak is more intense than the 0-1 peak), to distinctly an H-like emission spectrum (suppressed 0-0 intensity with respect to the rest of the progression). [72] We speculate that at early time, well within the time resolution of most ultrafast experiments ( $\blacksquare 100$  fs), nascent excitons are characterized by long coherence before localization occurs to produce the the coherence lengths at equilibrium conditions, as discussed in this work. Such a scenario involving hot, spatially coherent excitation at organic heterojunctions in the photocarrier photogeneration mechanism in solar cells has received significant support in the last year. [72, 109] Interestingly, photovoltaic efficiency performance in P3HT :PCBM diodes is found to be optimized with P3HT of medium  $M_w$ , [110] and we propose that early-time spatial coherence properties of polymer films may depend on the complex configurational and energetic landscape in similar ways as the equilibrium spatial coherence properties investigated here. We consider that this is a valuable future direction of research using techniques such as multidimensional electronic spectroscopy.

### 3.8 Conclusion

In this paper we have shown how to analyze the steady-state photoluminescence spectral line shape in order to obtain the two-dimensional exciton coherence function in semicrystalline polymeric semiconductors. In particular, the 0-0/0-1 PL ratio results from a competition between intrachain interactions, which serve to enhance the PL ratio (as is characteristic of J-aggregates) and interchain interac-

tions, which serve to attenuate the PL ratio (as is characteristic of H-aggregates). The resulting coherence function for P3HT  $\pi$ -stacks is J-like (nodeless) along the chain, and H-like (oscillating phase) across the chains. By contrast, the 0-2/0-1 PL ratio, quantifying the effective Huang-Rhys parameter of the vibronic progression, is sensitive primarily to intrachain excitonic coupling. In regioregular P3HT films, the interplay between intra- and intermolecular interactions results in a coherence "area" of approximately  $130 \text{ \AA}^2$ . Low molecular weight ( $M_w < 50 \text{ kg/mol}$ ) materials form chain-extended morphologies based on lamellar stacks of torsionally disordered macromolecules, leading to excitons with interchain spatial coherence that extends over  $\sim 10 \text{ \AA}$  (i.e. over 2.5 neighbouring macromolecules), but with intrachain spatial coherence limited to  $\sim 13 \text{ \AA}$  (i.e.  $\approx 3$  thiophene monomers). On the opposite regime, films made of high-molecular-weight P3HT ( $M_w > 50 \text{ kg/mol}$ ), which are characterized by two-phase morphologies consisting of interconnected crystalline and amorphous domains, host excitons that are spatially coherent over only  $\sim 7.5 \text{ \AA}$  along the stacking axis, but over  $\sim 18 \text{ \AA}$  along the chain. Hence, the coherence areas for P3HT of low and high  $M_w$  are similar, although high- $M_w$  materials host a more anisotropic coherence favored along the polymer chain axis. This establishes that there is a microstructure-dependent interplay between intrachain and interchain exciton interactions in this important class of semiconductor materials. Future work will be directed at exploring the time dependence of the spatial coherence as tracked by the time-resolved PL line shape.



## CHAPITRE 4

### CHARGE SEPARATION IN SEMICRYSTALLINE POLYMERIC SEMICONDUCTORS BY PHOTOEXCITATION : IS THE MECHANISM INTRINSIC OR EXTRINSIC ?

#### 4.1 Contexte de l'article

La diffusion des excitons de Frenkel dans un cristal se fait en transférant leur énergie de molécule en molécule par un mécanisme de diffusion résonant de type Förster. Cependant, ils ne portent pas de charge. Puisqu'ils ont une énergie de liaison largement supérieure à celle des excitons Wannier-Mott, il doit alors subsister un mécanisme permettant leur séparation en électron-trou indépendant. La majorité des dispositifs optoélectronique dont l'utilité est de récolter des charges suite à une excitation optique utilisent un complexe donneur/accepteur d'électrons. On utilise alors des matériaux de différentes affinités électronique et potentiel d'ionisation, ce qui cause un décalage entre leurs niveaux HOMO et LUMO et permet ainsi de transférer l'électron excité de la bande LUMO d'une molécule (donneur) à la bande LUMO d'une autre molécule (accepteur). De façon à dissocier efficacement la paire électron-trou, le décalage énergétique entre les bandes HOMO et LUMO du donneur et de l'accepteur doit être de l'ordre de l'énergie de liaison de l'exciton. [47]

La façon la plus efficace de scinder l'exciton sur deux molécules est de créer une hétérojonction volumique. [111] Par exemple, les dispositifs électroniques à base de P3HT sont généralement constitués d'un réseau interpénétré de P3HT et d'un dérivé du fullerène, le [6,6]-phényl-C<sub>61</sub>-butanoate de méthyle communément appelé PCBM, [112] formant ainsi une hétérojonction de type II efficace. [24] Les excitons créés aux interfaces entre les domaines de P3HT et PCBM se scindent directement

en paires de charges<sup>1</sup> sur des échelles de temps <150 fs [33–35] tandis que ceux créés dans les domaines cristallins de P3HT diffusent à ces interfaces à l’intérieur de 7 à 10 ps. [35, 113] Les paires de charges ainsi formées sont séparées spatialement sur les 2 molécules, abaissant par le fait même leur énergie de liaison à ~0.1 – 0.5 eV . [47, 114, 115] Puisque la longueur de diffusion des excitons dans le P3HT est de l’ordre de ~7-9 nm, [116, 117] il est important que la ségrégation des molécules soit telle que l’exciton puisse trouver une interface pendant son court temps de vie. Dans ce type d’hétérojonction, le P3HT joue à la fois le rôle de récolter la lumière et de conduire les trous, tandis que le PCBM se charge de la conduction des électrons. L’attraction coulombienne entre l’électron et le trou formant les polarons fortement liés favorise la recombinaison par rapport à la séparation complète en charges séparées. Pour cette raison, ces états intermédiaires et sombres ont à la fois été qualifiés de détrimentaires et de précurseurs pour la génération de charges libres, mettant une fois de plus l’emphase sur l’importance de la compréhension de la physique aux interfaces donneur/accepteur. Notons qu’à ce jour, il n’y a toujours pas de consensus sur le mécanisme exact de dissociation des excitons et charges aux interfaces.

Un résultat expérimental surprenant est qu’une présence de polarons est aussi observée sur des échelles de temps ultrarapides dans les films de P3HT (sans addition de PCBM), [52, 113, 118] et la présence de charges est difficilement explicable étant donné l’énergie de liaison élevée de l’exciton. L’observation de ces espèces se fait généralement par spectroscopie d’absorption transitoire. Cette expérience de type pompe sonde utilise une impulsion laser pour exciter le matériau, créant ainsi des espèces photoexcitées (excitons, polarons). Une seconde étape consiste à envoyer une sonde, qui est en fait une lumière blanche à large bande. Les quasi-particules ainsi formées peuvent alors absorber cette lumière, produisant

---

<sup>1</sup>Différentes nomenclatures sont utilisées pour décrire ces paires de charges interfaciales : paire de polaron liés, paire électron-trou lié, paire geminale de polarons

par le fait même un changement de la transmission de l'échantillon à l'intérieur de la bande interdite, aux longueurs d'onde où ces espèces absorbent. Le temps de vie de ces espèces dans le P3HT :PCBM peut être largement supérieur à la nanoseconde. [113, 118, 119] Ohkita et coll. ont aussi observé dans un complexe polymère/polymère de P3HT :F8BT que ces polarons peuvent subsister jusqu'à quelques microsecondes. [118]. La formation de polarons dans le P3HT relève de la morphologie complexe de ce polymère qui est constitué de domaines cristallins et de régions amorphes. En effet, certains ont stipulé que la formation se fait dans des domaines qui sont morphologiquement plus désordonnés que les domaines cristallins [34, 113, 120, 121]. D'autres ont révélé que le taux de formation augmente avec des impulsions d'énergie supérieure à la bande interdite, [113] mettant l'emphase sur le rôle possible des excitons chauds à la production de charges.

Ici, nous sommes intéressés à la recombinaison de ces polarons qui génèrent de la photoluminescence à long temps de vie (supérieur au temps de vie de l'exciton singulet). Nous démêlons ainsi la complexité du mécanisme de séparation de charge dans les films de P3HT à l'aide de méthodes spectroscopiques de photoluminescence en fonction du temps et avec l'appui de simulations de dynamique quantique. Dans les chapitres suivants, nous faisons un suivi des travaux du présent article en élucidant l'effet de la microstructure sur la dissociation des excitons.

## 4.2 Techniques de photoluminescence résolue en temps

Dans cet article, nous utilisons deux techniques qui nous permettent de sonder la dynamique de PL du P3HT. La première consiste à exciter l'échantillon avec une brève impulsion dont la longueur d'onde peut être variée grâce à un amplificateur paramétrique optique et récolter la photoluminescence réémise à l'aide d'une caméra à balayage picoseconde. Les photons sont alors converti en électrons sur une photocathode à l'entrée de la caméra et par la suite déviés verticalement par un

voltage appliqué entre une anode et une cathode. Les électrons frappent alors un écran de phosphore à une position qui dépend de leur temps d'arrivée. La chute de tension entre l'anode et la cathode du tube de la caméra se fait très rapidement, ce qui permet d'obtenir une résolution expérimentale de l'ordre de quelques picoseconds. Pour étudier la dynamique à des échelles temporelles supérieures, nous utilisons plutôt une ICCD ("Intensified charge-coupled device") dont la porte peut être contrôlée électroniquement. La résolution temporelle est inférieure à celle de la caméra à balayage picoseconde ( $\sim 5$  ns), mais l'intensificateur nous permet d'aller sonder la dynamique jusqu'à des échelles de temps de l'ordre de la  $\mu$ s, où la PL est très faible.

### 4.3 Contribution originale de chaque coauteurs

Francis Paquin a fait l'élaboration du montage expérimental et pris les mesures de photoluminescence ultrarapides avec la caméra à balayage picoseconde ainsi que les mesures d'anisotropie de photoluminescence et de dépendance en fluence. Les mesures de photoluminescence résolue en temps avec la ICCD ont aussi été prises par Francis Paquin et la modélisation faite par Gianluca Latini et Francis Paquin. Les mesures d'excitation de la photoluminescence à long temps de vie ont été prises par Maciej Sakowicz et Francis Paquin. Les mesures d'efficacité quantique externe sur la diode à base de P3HT ont été prises par Maciej Sakowicz. Les mesures d'absorption transitoire ont été prises par Paul-Ludovic Karsenti et Francis Paquin. Les mesures de photoluminescence en continu ont été prises par Francis Paquin. Les calculs quantiques ont été élaborés par Linjun Wang et David Beljonne. Carlos Silva a écrit le manuscript en étroite collaboration avec Francis Paquin.

# Charge Separation in Semicrystalline Polymeric Semiconductors by Photoexcitation : Is the mechanism Intrinsic or Extrinsic ?

Francis Paquin,<sup>1</sup> Gianluca Latini,<sup>2</sup> Maciej Sakowicz,<sup>1</sup> Paul-Ludovic Karsenti,<sup>1</sup>  
Linjun Wang,<sup>3</sup> David Beljonne,<sup>3</sup> Natalie Stingelin,<sup>2</sup> and Carlos Silva<sup>1</sup>

<sup>1</sup>*Département de physique & Regroupement québécois sur les matériaux de pointe,  
Université de Montréal, C.P.6128, Succursale centre-ville, Montréal (Québec)  
H3C 3J7, Canada*

<sup>2</sup>*Department of Materials and Centre for Plastic Electronics, Imperial College  
London, South Kensington Campus, London SW7 2AZ, United Kingdom*

<sup>3</sup>*Chemistry of Novel Materials, University of Mons, Place du Parc 20, B-7000  
Mons, Belgium*

Phys. Rev. Lett. 106, 197204 (2011)

#### 4.4 Abstract

We probe charge photogeneration and subsequent recombination dynamics in neat regioregular poly(3-hexylthiophene) films over six decades in time by means of time-resolved photoluminescence spectroscopy. Exciton dissociation at 10 K occurs extrinsically at interfaces between molecularly ordered and disordered domains. Polaron pairs thus produced recombine by tunnelling with distributed rates governed by the distribution of electron-hole radii. Quantum-chemical calculations suggest that hot-exciton dissociation at such interfaces results from a high charge-transfer character.

## 4.5 Introduction

Unravelling primary electronic processes in polymeric semiconductors opens a fundamental window to their materials physics. The steps to generate charge by optical absorption are currently the subject of wide interest [47]. Here, we focus on charge generation and recombination dynamics in *neat* regioregular poly(3-hexylthiophene) (P3HT). This semicrystalline polymer adopts  $\pi$ -stacked lamellar microstructures in the solid state [7], leading to two-dimensional electronic dispersion [122]. Crystallinity induced by molecular organization influences profoundly electronic properties, exemplified by the high yield ( $\eta$ ) up to 30% over ultrafast timescales in P3HT films at 300 K [33, 123–126]. However, photoemission spectroscopy measurements place the energy for free polaron generation  $\sim 0.7$  eV above the optical gap in neat P3HT [127]. Weak interchain electronic coupling in the lamellar architecture leads to a free-exciton bandwidth — the pure electronic bandwidth due to dispersion neglecting coupling to vibrations — that is well below this energy [60, 66, 128, 129]. Thus, are charges indeed generated *intrinsically* (directly by photoexcitation due to the crystalline electronic structure) or *extrinsically* (due to a driving force for exciton dissociation) ?

Charge photogeneration in neat P3HT has been studied previously by means of transient absorption spectroscopy [124, 126], which measures directly the dynamics of nascent polarons. We implement time-resolved photoluminescence (PL) spectroscopy at 10 K to probe charge photogeneration and recombination dynamics. Our strategy is to exploit the intricate detail of electronic structure, structural relaxation, and correlated disorder afforded by the spectral bandshape of the PL spectrum [60], over timescales where it is known that charge photogeneration is important. We probe the recombination environment via the bandshape and decay dynamics of delayed PL from charge-pair recombination, which also probes the environment in which photogeneration occurs, since photoexcitations are fro-

zen at 10 K. We find that charge generation occurs over sub-nanosecond timescales by dissociation of excitons created at interfaces between lamellar (aggregate) and poorly stacked (non-aggregate) domains, driven by energetic disorder. Thus, prompt charge photogeneration is an *extrinsic* process, and film microstructure determines the surface area and the energy landscape of interfaces between domains.

#### 4.6 Experimental Methods

PL measurements were carried out with a 40-fs, 532-nm (2.33-eV) pulse train derived from an optical parametric amplifier (Light Conversion TOPAS), pumped by a Ti :sapphire laser system (KMLabs Dragon). Time-resolved PL spectra were measured with an optically-triggered streak camera (Axis-Photonique, 6-ps instrument response). Alternatively, an intensified CCD camera (Princeton-Instruments PIMAX 1024HB) was used. P3HT films (Merck,  $M_w = 47.8$  kg/mol, 150-nm thick) were spun from trichlorobenzene solution (6% wt).

In P3HT films, the PL spectrum is understood within the framework of a weakly-coupled H-aggregate model [129], resulting from weak resonance-Coulomb coupling ( $J$ ) of transition moments aligned co-facially in neighboring polymer chains [66, 128]. In contrast, the absorption spectrum contains contributions from both the aggregate and non-aggregate regions [129]. From the ratio of the (0,0) and (0,1) absorbance peaks [130] (see appendix.II, we estimate a free-exciton bandwidth ( $W = 4J$ ) of  $100 \pm 3$  meV [129].

#### 4.7 Results and Discussion

Fig. 4.1(a) displays time-resolved PL measurements at 10 K. The PL spectrum decays substantially over sub-nanosecond timescales, and it red-shifts by  $> 40$  meV with weak evolution of the spectral bandshape. We examine in more detail this spectral evolution in Fig. 4.1(b). Fig. 4.1(c) displays the early-time PL anisotropy,

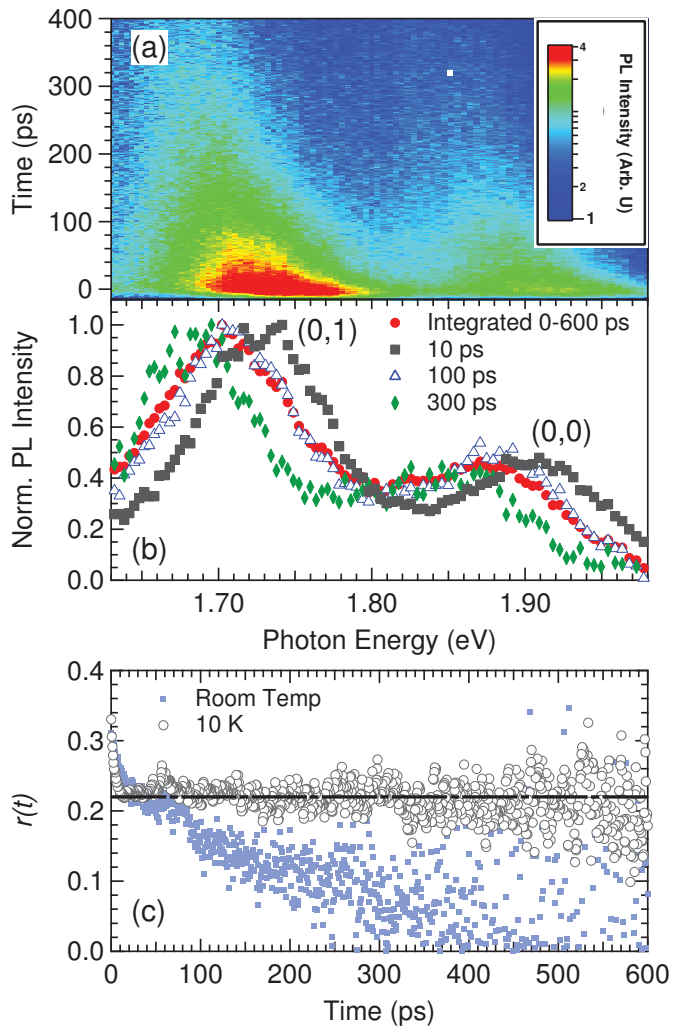


Figure 4.1 – (Color online) (a) Time-resolved PL spectrum ( $10\text{ K}$ ,  $19\text{ }\mu\text{J cm}^{-2}$  per pulse). (b) Normalized slices of (a) at various times. (c) Time-resolved PL anisotropy  $r$  at  $10\text{ K}$  (open circles) and at room temperature (dots). The horizontal line indicates the average anisotropy between  $20$  and  $600\text{ ps}$ .

defined as  $r = (I_{\parallel} - I_{\perp})/(I_{\parallel} + 2I_{\perp})$ , where  $I_{\parallel(\perp)}$  is the instantaneous PL intensity parallel (perpendicular) to the linear polarization of the pump pulse. At 10 K (open circles),  $r$  decays to  $0.22 \pm 0.03$  within the instrument response of several picoseconds due to exciton self trapping in the photophysical aggregate [131, 132], and does not evolve further on a sub-nanosecond window. In contrast,  $r$  decays to zero after 500 ps at room temperature. PL anisotropy decay is a signature of exciton diffusion [133], so at 10 K, excitons are immobile over the timescale of the dynamic red shift in Fig. 4.1(a). Another possibility could be relaxation of excess vibrational energy following ultrafast excitation of the sample. Parkinson et al. have reported that torsional relaxation of the backbone leads to more cofacial lamellar structures (more extended correlation of site energies in the aggregate [60]), leading to a dynamic loss of (0,0) intensity over  $\sim 13$  ps at 300 K [134]. We do not observe significant relaxation of the (0,0) relative intensity over the timescale of Fig 4.1(a). Furthermore, upon increasing the temperature even slightly, the steady-state PL spectrum broadens significantly at 10 K [129], so we rule out thermal relaxation. We suggest that the dynamic spectral red-shift of the PL spectrum results from an evolving electric field distribution [135] from photogenerated charges in the aggregate, which is consistent with charge photogeneration yields reported in the literature and our own transient absorption measurements (see appendix.II). If so, charges are generated over all timescales spanning 1 ns, by a mechanism not involving exciton diffusion.

We next consider delayed PL dynamics due to charge recombination. Fig. ??(a) displays time-gated PL spectra at 10 K. After a few nanoseconds, the aggregate spectrum is superimposed with a broader component (see appendix.II) with similar dynamics to those of the H aggregate since this composite bandshape persists over microseconds. While we know that the aggregate spectrum arises from lamellar stacks, we conjecture that the featureless spectrum arises from non-aggregate regions. It is reminiscent of red-emitting species found in amorphous polymer films,

often referred to as excimers [136]. From the delayed PL bandshape in Fig. ??(a), we conclude that recombination occurs at the interface between H-aggregate and non-aggregate regions, and can populate either species.

The total PL intensity decays exponentially over picosecond timescales, but asymptotically as a power law ( $I(t) \propto t^{-1.54}$ ) for times much longer than the exciton lifetime (Fig. ??(b)). This behavior can arise from unimolecular charge recombination [137] or by triplet bimolecular annihilation [138, 139]. We find that the delayed PL intensity varies linearly with the pump fluence (see appendix.II), which permits us to assign the power-law decay to exciton regeneration by charge recombination with a distribution of rates, as the other two possibilities would lead to a non-linear fluence dependence. The power-law decay is independent of temperature (see appendix.II), suggesting recombination by tunnelling. We note that we cannot reproduce the measured time-resolved PL intensity as a simple superposition of a multiexponential and an asymptotic power-law decay, as the time window spanning 1–10 ns features a PL decay over nearly three orders of magnitude that deviates significantly from either decay function (Fig. ??(b)). This indicates that the two PL decay phenomena are not independent, but that one decay regime evolves into the other, with competing kinetics on nanosecond timescales. By integrating the PL intensity over timescales where the decay is non-exponential, we find that  $\geq 12\%$  of the time-integrated intensity is accounted for by slow recombination. This reflects a significant density of charge pairs.

Based on the results of Figs. 4.1 and ?? and building upon previous reports [33, 123–126], we construct the following photophysical picture, depicted schematically in Fig. ??(c). Upon photoexcitation, charge pairs are generated with efficiency  $\eta$ , and the rest of the population relaxes to self-trapped excitons  $x$  in  $<1\text{ ps}$  [132]. These decay to the ground state with rate constant  $\Gamma_x$ , or charge-separate with rate constant  $\Gamma_{ct}$ . Charge pairs may recombine to regenerate  $x$  with a temporal

distribution  $R(t)$ . Thus,

$$\frac{dx}{dt} = -(\Gamma_x + \Gamma_{ct})x + \eta R(t) + \int_0^t \Gamma_{ct}x(t')R(t-t')dt'. \quad (4.1)$$

Assume a distribution of charge-pair distances  $f(r) = \varepsilon e^{-\varepsilon r}$ . The tunnelling rate is  $k(r) = v e^{-\beta r}$  and its time distribution is  $R(t) = \int_0^\infty f(r)k(r)e^{-k(r)t}dr$ . With  $x(0) = 1 - \eta$ , the Laplace transform of eq. 4.1 is

$$\hat{x}(s) = \frac{1 - \eta + \eta \hat{R}(s)}{s + \Gamma_x + \Gamma_{ct} [1 - \hat{R}(s)]}, \quad (4.2)$$

where  $\hat{R}(s) = \mu \int_0^\infty e^{-(1+\mu)\chi} / (s/v + e^{-\chi}) d\chi$ ,  $\chi = \beta r$ , and  $\mu = \varepsilon/\beta$ . The model predicts biphasic dynamics with PL intensity,  $I(t) \propto \Gamma_x x(t)$ , evolving as  $I(t) \propto \exp(-\Gamma_x t)$  at short times and as  $I(t) \propto t^{-(1+\mu)}$  at long times. We evaluate eq. 4.2 as described elsewhere to recover  $I(t)$  [140].

The most robust parameter in this model is the ratio of the characteristic electron-hole separation ( $\varepsilon$ ) and the distance dependence of charge tunnelling ( $\beta$ ) :  $\mu = \varepsilon/\beta = 0.54 \pm 0.08$ , as it defines uniquely the slope of the power-law decay at long times. Hence,  $\varepsilon \approx 0.54\beta$ ; a significant fraction of charge pairs do not recombine in the microsecond timescale, as the tail of  $f(r)$  extends beyond the characteristic lengthscale of  $k(r)$ . The charge-pair population is expected to survive on much longer timescales, which is consistent with reports of a high residual charge density in P3HT at steady state [141, 142].

We next consider  $\eta$ . We cannot extract it uniquely from the model, as it is coupled to  $\Gamma_{ct}$ . Both parameters affect the amplitude of the power-law decay without altering the decay rate. We probe the range of  $\eta$  that is consistent with the literature, and explore the consequences on  $\Gamma_{ct}$ . With  $\Gamma_x = 1.23 \text{ ns}^{-1}$  (fixed by the slow part of the bi-exponential decay in Fig. 4.1(a)) and with  $v = 4.37 \times 10^{13} \text{ s}^{-1}$  (corresponding to the frequency of the aromatic C—C stretch measured by Raman

spectroscopy [143]), we find that if we set  $\eta = 3\%$ , we require  $\Gamma_{ct} = 0.35 \pm 0.05 \text{ ns}^{-1}$ , but if  $\eta = 30\%$  we can reproduce the data with  $\Gamma_{ct} = 0$ . With  $\eta = 40\%$ , we can no longer obtain a satisfactory fit of the amplitude of the power-law component, which is over-estimated. We have interpreted the dynamic red shift of the PL spectrum (Fig. 4.1) as a consequence of an evolving electric field on the subnanosecond timescale, which is comparable to the exciton lifetime. In order to rationalize our time-resolved spectroscopic data, we therefore consider that  $\Gamma_{ct}\Gamma_x$ , which from the modelling, would imply that  $\eta < 10\% \text{ in the solid-state microstructure of our films}$ .

If the two slow-decaying emissive species in Fig. ??(a) are due to regeneration of aggregate and non-aggregate excitations by charge tunnelling, we propose that charges are initially generated at the interface between the two domains. To explore this further, we have carried out quantum chemical calculations [144] on a stack of ten oligothiophene chains (Fig. 4.2(a)) to represent the crystalline moieties in the higher molecular-weight (i.e. longer chain) P3HT used in our experimental study. We note higher conformational disorder at the top/bottom of the stack, leading to a higher excitation energy in those regions compared to the center (Fig. 4.2(b)). Fig. 4.2(c) displays the calculated absorption spectrum in a given configuration. For all stack configurations studied, we always observe a shoulder at  $\sim 2.7 \text{ eV}$  on the blue side of the main absorption band at  $\sim 2.4 \text{ eV}$ . (Note that these energies are overestimated, but the  $\sim 0.3 \text{ eV}$  difference is meaningful.) The excited states that are generated in this spectral region are quasi-degenerate with the lowest-lying charge-transfer (CT) states, shown by the superimposed plot of CT character as a function of excitation energy. We can identify three regimes of the spatial distribution of transition densities, shown in Fig. 4.2(d). The excitation with the lowest transition energy (I) is always confined to the center of the stack over two to three sites as a result of disorder and is weakly emissive (H aggregate); the intermediate excitation (II) carries most of the oscillator strength and is delocalized in the center of the stack; the higher-lying excitation (III) is dominated by conformationally

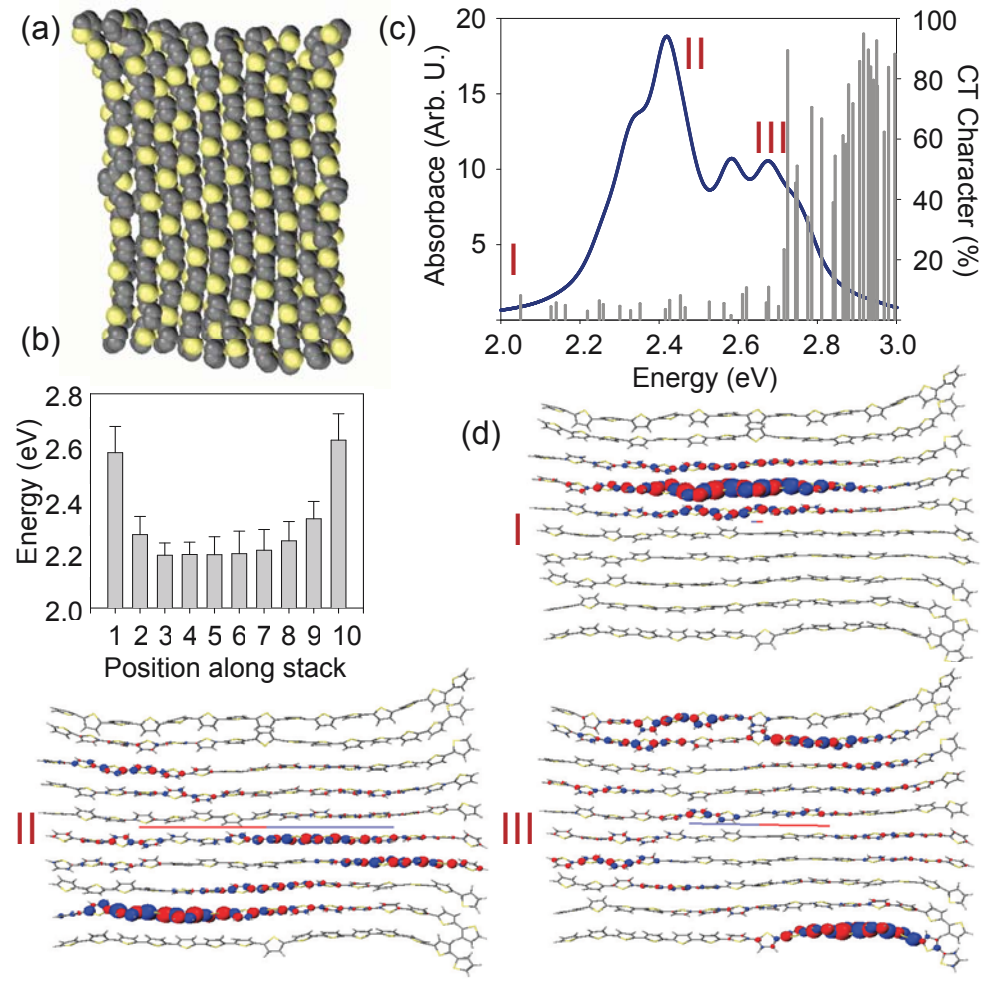


Figure 4.2 – (Color online) (a) Snapshot of an aggregate architecture (15-mers in a 10-chain stack [144]). (b) Average site excitation energy (uncertainty is the variance), averaged over many excited-state calculations on isolated conformers extracted from the stack. (c) Absorption spectrum for one configuration of the full stack superimposed to the corresponding CT character. (d) Transition densities (ground-state – excited-state overlap) for excitations of increasing energy.

disordered chains at the ends of the stack, but it communicates with chains in the center so that charge separation of these higher-energy states is possible. In our measurements, we excite  $\sim 0.3$  eV above the (0,0) absorption, placing us at the limit of CT excitation predicted by Fig. 4.2(c). We have measured the delayed PL excitation spectrum, shown in Fig ??(d). This reveals that excitation on the edge of the component of the absorption spectrum due to less ordered or amorphous species enhances the delayed PL yield, consistent with the significant CT character of excitons at these photon energies. Photocurrent measurements reveal that a further 0.4-eV energy is required to produce charge carriers (Fig. ??(d)), underlining that our delayed PL measurements probe recombination of tightly-bound geminate polaron pairs (not carriers) produced by excitation with energies 3 eV. Deibel et al. reported that 0.42-eV excess energy above the optical gap is required to produce polaron pairs, and then a further 0.3 eV to generate photocarriers [127], consistent with our findings.

We have presented compelling evidence that excitons with sufficient energy dissociate *extrinsically* near interfaces between molecularly organized and less organized domains, underlining the importance of the disordered energy landscape. This competes with dissociation at heterojunctions in photovoltaic diodes [47].

## CHAPITRE 5

### MULTI-PHASE SEMICRYSTALLINE MICROSTRUCTURES DRIVE EXCITON DISSOCIATION IN NEAT PLASTIC SEMICONDUCTORS

#### 5.1 Contexte de l'article

Dans ce chapitre, nous établissons un pont entre le taux et la dynamique de recombinaison des paires de polarons formés suite à une excitation optique et la microstructure conférée par le poids moléculaire et les procédés de fabrication. Les films créés directement à l'état solide, par pressage du polymère entre deux substrats de verre, sont hautement cristallins et indiquent des mobilités de charge jusqu'à 3 ordres de grandeur supérieures à ceux créés à partir de solution, [145] mais avec un taux de formation nettement inférieur à ce qui est mesuré dans ces derniers. [18] Dans un premier temps, nous cherchons à contrôler l'aire d'interface entre les régions cristallines et les domaines amorphes pour ainsi observer l'influence de la microstructure sur le taux de paires de charges formées. En second lieu, nous appliquons le modèle dynamique présenté au chapitre précédent, ce qui nous permet de sonder la dynamique de recombinaison des paires de polarons en associant la pente de la recombinaison en loi de puissance à long temps de vie à la distance caractéristique entre l'électron et le trou qui forment cette paire.

#### 5.2 Contribution originale de chaque coauteurs

Francis Paquin a pris tous les résultats expérimentaux et fait l'analyse de ceux-ci à l'exception des mesures de diffraction par rayons-x qui provient de Jonathan Rivnay. Carlos Silva et Francis Paquin ont écrit l'article et tous les coauteurs ont apportés leurs commentaires.

Francis Paquin,<sup>1</sup> Jonathan Rivnay,<sup>2</sup> Alberto Salleo,<sup>2</sup> Natalie Stingelin,<sup>3</sup> and  
Carlos Silva,<sup>1</sup>

<sup>1</sup>*Département de physique & Regroupement québécois sur les matériaux de pointe,  
Université de Montréal, C.P.6128, Succursale centre-ville, Montréal (Québec)  
H3C 3J7, Canada*

<sup>2</sup>*Materials Science and Engineering, Stanford University, 476 Lomita Mall, 239  
McCullough Building, Stanford, California 94305, United States*

<sup>3</sup>*Department of Materials and Centre for Plastic Electronics, Imperial College  
London, South Kensington Campus, London SW7 2AZ, United Kingdom*

(Submitted to Phys. Rev. X)

### 5.3 Abstract

The optoelectronic properties of macromolecular semiconductors depend fundamentally on their solid-state microstructure. For example, the molecular-weight distribution influences polymeric-semiconductor properties via diverse microstructures; polymers of low weight-average molecular weight ( $M_w$ ) form unconnected, extended-chain crystals, usually of a paraffinic structure. Because of the non-entangled nature of the relatively short-chain macromolecules, this leads to a polycrystalline, one-phase morphology. In contrast, with high- $M_w$  materials, where average chain lengths are longer than the length between entanglements, two-phase morphologies, comprised of crystalline moieties embedded in largely unordered (amorphous) regions, are obtained. We investigate charge photogeneration processes in neat regioregular poly(3-hexylthiophene) (P3HT) of varying  $M_w$  by means of time-resolved photoluminescence (PL) spectroscopy. At 10 K, PL originating from recombination of long-lived charge pairs decays over microsecond timescales. Both the amplitude and decay rate distribution depend strongly on  $M_w$ . In films with dominant one-phase chain-extended microstructures, the delayed PL is suppressed as a result of a diminished yield of photoinduced charges, and its decay is significantly faster than in two-phase microstructures. However, independent of  $M_w$ , charge recombination regenerates singlet excitons in torsionally disordered chains forming more strongly coupled photophysical aggregates than those in the steady-state ensemble, with delayed PL lineshape reminiscent of that in paraffinic morphologies at steady state. We conclude that highly delocalized excitons in disordered regions between crystalline and amorphous phases dissociate extrinsically with yield and spatial distribution that depend intimately upon microstructure.

## 5.4 Introduction

Understanding how the solid-state microstructure of neat polymeric semiconductors influences their photophysical properties is of fundamental importance in plastic optoelectronics. For example, state-of-the-art organic solar cells rely on so-called bulk heterojunctions, in which electron acceptors (typically fullerene derivatives) are blended in a  $\pi$ -conjugated polymer matrix, which acts as the electron donor. The resulting solid-state microstructures can be fantastically complex, typically involving multiple phases that consist of crystalline and amorphous domains rich in each component, and potentially co-crystallized and inter-mixed amorphous phases [146–148]. The details of the disordered energy landscape that drives electronic processes such as charge separation depend intimately on the solid-state microstructure, and specifically on how structure on mesoscopic lengthscales leads to order on molecular lengthscales.

In this communication, we address this issue focusing on exciton dissociation and recombination processes in neat, regioregular P3HT. In a previous letter [149], we reported that tightly bound geminate-polaron pairs are formed on sub-picosecond timescales following ultrafast photoexcitation, which subsequently recombine by tunnelling over distributed timescales, producing delayed PL. We speculated that these are generated in intermediate regions between crystalline and amorphous phases, and that the recombination dynamics depend upon the local energy landscape in these regions. In order to develop this hypothesis, we present here time-resolved PL measurements in neat P3HT films of  $M_w$  ranging over 12–331 kg/mol. For  $M_w$  40 kg/mol, polycrystalline one-phase morphologies dominate in solution-processed films (Fig. 5.1(a)) [150–152]. For similar processing, material of  $M_w$  50 kg/mol produces complex two-phase architectures, in which crystalline lamellae are embedded in largely amorphous regions (Fig. 5.1(b)) [153]. Independent of  $M_w$ , predominantly chain-extended microstructures are achieved by pressing the

polymer in the solid state (Fig. 5.1(c)) [145, 154]. Therefore, by choice of molecular weight and processing route, solid-state microstructures ranging from one-phase polycrystalline through semicrystalline (two-phase) P3HT architectures can be prepared. We find that indeed exciton dissociation is favoured by the disordered landscape at gradual interfaces between crystalline and amorphous regions, with a yield of photoinduced charges that depend on the solid-state microstructure. Furthermore, as the disorder along the  $\pi-\pi$  stacking direction increases, the mean electron-hole separation increases, leading to a slower distribution of charge recombination times. Our conclusions on neat P3HT help shed light on how structural and energetic disorder plays a role in driving excitonic processes in more complex systems, such as the class of bulk heterojunction structures. More generally, our work provides a general fundamental link between organic-semiconductor photophysics and classical polymer science.

## 5.5 Results and analysis

Fig. 5.2 shows time-resolved PL spectra for both solution processed (panels a and b) and solid-state processed (panels c and d) films at time delays indicated in each panel. With the shortest temporal gate of our detector (5 ns, Fig. 5.2(a)), the solution-processed films display spectral lineshapes that depend on  $M_w$ . Over this short gate window, we measure the integrated PL intensity over the exciton intrinsic lifetime in neat P3HT [149], and the gated PL spectra therefore reflect the same ensemble properties as steady-state PL spectra. As  $M_w$  increases, two clear trends in the prompt PL spectral lineshapes are evident : (i) the relative amplitude of the 0–0 peak at 1.88 eV, when spectra are normalized to the 0–1 feature at 1.70 eV, increases at high  $M_w$ ; (ii) the effective Huang-Rhys parameter, here defined as  $\lambda_{\text{eff}}^2 = 2I^{0-2}/I^{0-1}$ , decreases from  $\lambda_{\text{eff}}^2 = 1.5 \pm 0.2$  at  $M_w = 12 \text{ kg/mol}$  to  $\lambda_{\text{eff}}^2 = 0.9 \pm 0.1$  at  $M_w = 348 \text{ kg/mol}$ . In a separate publication, we have reported

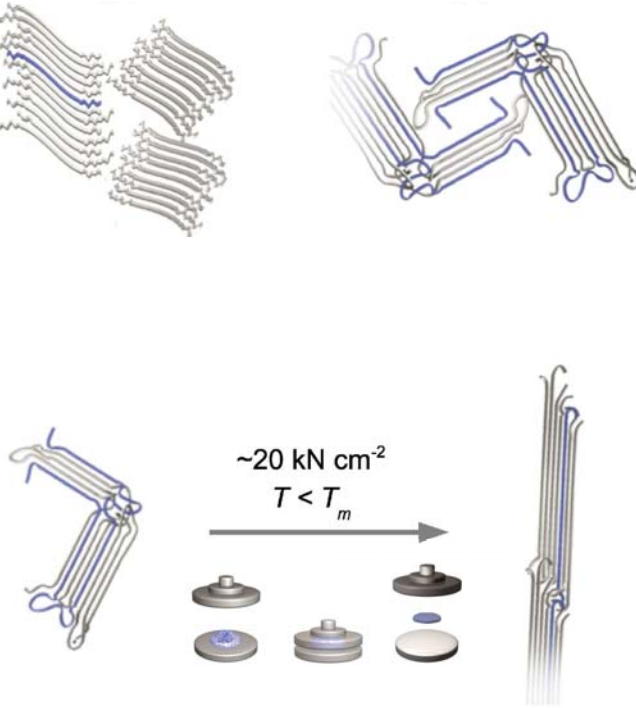


Figure 5.1 – Schematic of different solid-state microstructures adopted by the films studied in this work. (a) P3HT of low  $M_w$  leads to isolated, unconnected extended-chain crystals, forming polycrystalline one-phase morphologies. In this regime, the chain length is shorter than the threshold for chain entanglement,  $M_e$ . Any particular oligomer chain (e.g. that highlighted in blue) is a building block of only one crystal on average. (b) P3HT of high  $M_w$ , where chain lengths exceed  $M_e$ , leads to a two-phase microstructure, in which crystalline lamella are embedded in largely amorphous regions that result from chain entanglements in the liquid state, which hinder molecular ordering during solidification [153]. Individual polymer chains may serve as tie molecules connecting different crystals through amorphous regions (highlighted in blue). (c) By pressing the polymer powder at temperatures below the melting point  $T_m$ , the lamellar crystal thickness is enlarged, thereby inducing predominantly chain-extended morphologies that depend weakly on  $M_w$ .

steady-state PL spectra of solution-processed P3HT throughout this range of  $M_w$ , and modelled the spectral lineshape evolution with  $M_w$  within the framework of a photophysical aggregate model taking into account both intra- and intermolecular

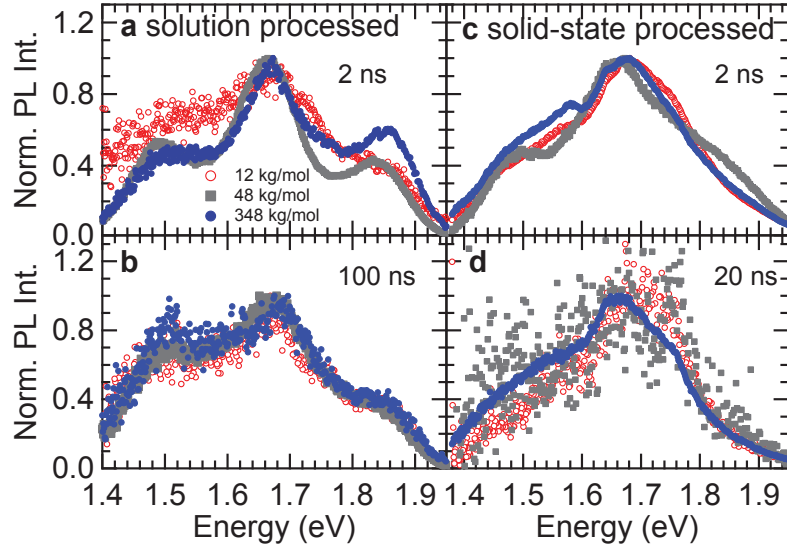


Figure 5.2 – Time-gated photoluminescence spectra measured at 10 K. Prompt (a) and delayed (b) spectra for solution-processed films of different weight-average molecular weight, indicated in the legend of part a, are displayed. Panels (c) and (d) display prompt and delayed PL spectra, respectively, for solid-state-processed films of the same materials as those in the solution-processed films. The time delay after excitation is indicated in each panel. In all panels, the spectra were normalised to have equal intensity at 1.70 eV, the energy of the 0–1 vibronic peak.

electronic dispersion [64]. The 0–0/0–1 ratio depends entirely on the intrachain excitonic (resonance-Coulomb) coupling [155, 156], and  $\lambda_{\text{eff}}^2$  reflects the degree of torsional disorder along the chain backbone [64]. The interchain excitonic coupling decreases abruptly for  $M_w \geq 50 \text{ kg/mol}$  [64, 157]. This coincides with a transition from a one-phase microstructure (Fig. 5.1(a)) to a two-phase one (Fig. 5.1(b)) [150–152]. The abrupt transition in excitonic coupling around  $M_w \sim 50 \text{ kg/mol}$  influences the exciton coherence length derived from steady-state PL spectra [64] : in the low- $M_w$  regime, the exciton coherence length is larger along the  $\pi$ -stack direction than in the high- $M_w$  regime. Concomitantly, As  $M_w$  increases, polymer chains constituting the lamellar lattice are on average more planar as they are sterically less influenced by chain ends, and more susceptible to neighbouring chains in the  $\pi$  stack [152].

Therefore, the decrease of  $\lambda_{\text{eff}}^2$  and increase of the 0–0/0–1 PL ratio with increasing  $M_w$  is consistent with longer, more torsionally ordered, planar chains with decreasing interchain excitonic coupling. The time-resolved PL spectral lineshapes in Fig. 5.2(a) reproduce the steady-state PL spectra reported previously [64], and we interpret this trend accordingly.

On longer time windows, we observe delayed PL assigned to recombination of geminate charge pairs over distributed timescales [149], Fig. 5.2(b). In all of the samples, the relative 0–0 intensity is lower than that on short time windows, and it depends weakly on  $M_w$ . In fact, in all samples, the relative 0–0 intensity resembles that in the steady-state spectrum of films of the lowest  $M_w$ . Furthermore, the Huang Rhys parameter is also similar in the delayed PL spectra of all samples, at  $\lambda_{\text{eff}}^2 \sim 1.5$ , again reminiscent of that in the lowest  $M_w$  sample at early time (Fig. 5.2(a)) and at steady state [64]. This suggests that slow charge recombination events populate a sub-ensemble that is *always* characterized by a microstructure similar to the average bulk one in the lowest  $M_w$  sample, characterized by higher interchain excitonic coupling and higher intrachain torsional disorder than the broader ensemble of emitters over the fast gate window, resulting in longer interchain spatial coherence and more limited intrachain one. This points at the  $M_w$  independence of the microstructure hosting charge recombination, which we have argued is the same environment as the charge separation environment at 10 K [149]. We can therefore conclude that charge separation occurs in regions with highest configurational disorder, which resemble low- $M_w$  average microstructures, in all samples.

In the solid-state processed samples, in which a chain-extended conformation is forced on the polymer film, both the prompt (Fig. 5.2(c)) and the delayed (Fig. 5.2(d)) PL spectra display very weak relative 0–0 intensity. Self-absorption in these considerably thicker films cannot be ruled out easily, which complicates attempts to analyze the 0–0 relative intensity. Importantly, the spectral lineshape at lower energies is similar for prompt and delayed PL at all  $M_w$ , in contrast to those

in the solution-processed samples discussed above. The effective Huang-Rhys parameter is more akin to that in the highest  $M_w$  film for all samples, namely  $\lambda_{\text{eff}}^2 \sim 1$ , which is suggestive of a more torsionally ordered recombination environment in all solid-state processed films compared to solution-processed counterparts. These observations are consistent with a significant reduction of the disordered regions near chain entanglements that we conclude are responsible for geminate polaron pair generation in solution-processed films.

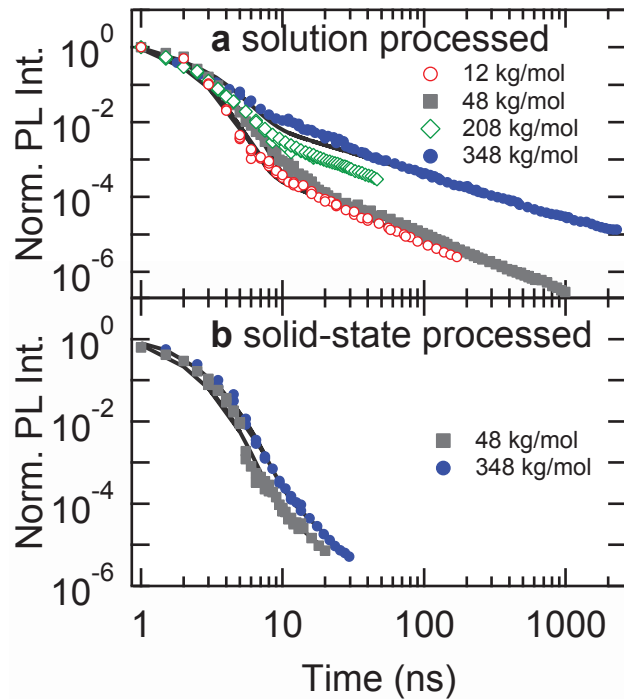


Figure 5.3 – Time-resolved photoluminescence intensity measured at 10 K. The weight-average molecular weight is indicated in the figure for both solution (a) and solid-state processing conditions (b). The intensity was determined by integrating time-resolved spectra such as those displayed in Fig. 5.2. The data were normalised to have equal intensity at a 1-ns delay.

In order to quantify differences in geminate-pair generation and recombination kinetics, we consider the evolution of the spectrally integrated PL intensity. Fig. 5.3(a) shows time-resolved PL intensity of solution-processed films of different

$M_w$ , measured at 10 K. We have previously assigned the long power-law component to distributed recombination of geminate-polaron pairs [149]. Here, we observe a marked dependence of the power-law decay kinetics on  $M_w$ ; the long-lived emission amplitude increases significantly ( $> 40\%$  of total PL intensity) for the sample with  $M_w = 348 \text{ kg/mol}$ , relative to that in ref. [149] ( $M_w = 48 \text{ kg/mol}$ ;  $> 12\%$  delayed PL intensity). The increased delayed PL intensity with increasing  $M_w$  is accompanied by a slow-down of the power-law decay. While the power-law decay kinetics are dramatically different in the diverse solid-state microstructures arising from solution processing, they are weakly dependent on  $M_w$  in the solid-state processed films (Fig. 5.3(b)). These show a significant decrease in the amplitude of the power law for all  $M_w$  studied, as well as an increase of the decay rate with respect to solution-processed films. The delayed PL dynamics are profoundly different by solid-state processing (Fig. 5.1(c)). In these, the surface area of photophysical aggregate and non-aggregate phases is reduced in all samples regardless of molecular weight, leading to a substantial reduction in the geminate pair yield, as the volume of conformationally disordered regions is reduced substantially.

We now consider the evolution of the slope of the power-law decay with  $M_w$  in greater detail. To explain the time-resolved PL intensity decay, we have invoked a model which accounts for rapid branching between bright excitons and dark geminate polaron pairs following photoexcitation, followed by a distribution of times for recombination [149]. The initial exponential component thus arises from relaxation of the emissive state during the excited-state lifetime, while the power-law component results from regeneration of excitons via recombination of geminate polarons with a distribution of rates. The absence of any marked temperature dependence in the power-law decay suggests that recombination of geminate pairs occurs via tunnelling of charges on distinct polymer chains, such that the recombination rate constant is exponentially distance-dependent,  $k(r) \propto e^{-\beta r}$ . Furthermore, following Tachiya and Seki [158], we assumed an exponential distribution of geminate-pair

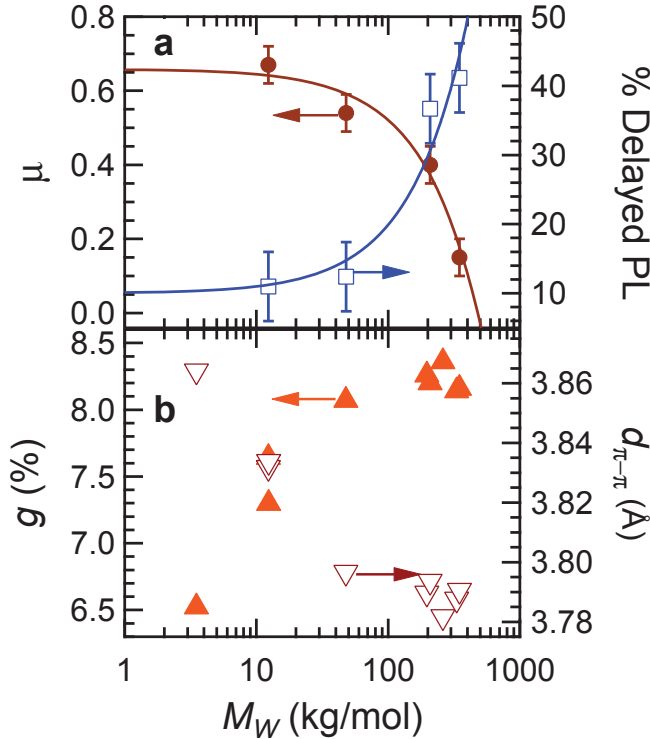


Figure 5.4 – (a) Power-law decay parameter  $\mu$  (left axis) and delayed PL relative intensity (right axis) versus  $M_w$ . The parameters are obtained by fitting the long-time time-resolved PL data such as that displayed in Fig. 5.3 to a power law in the form  $I \propto t^{1+\mu}$ , with the delayed PL intensity corresponding to the power-law amplitude. Within the model invoked here,  $\mu$  represents the ratio of the characteristic geminate-pair radii and the distance dependence of the charge recombination rate. A linear fit to  $\mu(M_w)$  has intercept  $0.66 \pm 0.03$  and slope  $(-1.37 \pm 0.16) \times 10^{-3}$  mol/kg. A linear fit to the delayed PL intensity data has intercept 10 and slope 0.099. (b) Paracrystalline disorder  $g$  and  $\pi-\pi$  stacking distance  $d_{\pi-\pi}$  versus  $M_w$ , derived from wide-angle X-ray scattering measurements. Disorder in  $d_{\pi-\pi}$  is quantified by  $g$ .

separation for the purposes of modelling,  $f(r) = \varepsilon e^{-\varepsilon r}$ . Within this model, the waiting time distribution for recombination is determined by these spatial functions,  $R(t) = \int_0^\infty f(r)k(r)e^{-k(r)}dr$ . The long-time PL decay is governed by geminate-pair recombination events, and is functionally of the form  $I(t \gg \tau) \propto t^{1+\mu}$ , where  $\tau$  is the excited-state lifetime and  $\mu \equiv \varepsilon/\beta$ . Thus, if the characteristic electron-hole

separation  $\varepsilon$  in the distribution  $f(r)$  increases, or if  $\beta$  decreases,  $\mu$  increases and the power-law decays more slowly. We show the dependence of  $\mu$  on  $M_w$  in the solution-processed films in Fig. 5.4(a), which shows a marked apparently linear decrease with increasing  $M_w$ .

In order to explore the trend in  $\mu$  by considering the evolution of lamellar structure with  $M_w$ , we have calculated the paracrystalline disorder parameter,  $g$ , in the  $\pi$ -stacking direction, which is the standard deviation in the  $\pi$ -stacking distance as a percentage of the mean lattice spacing (the  $\pi$ -stacking distance) [159, 160]. Therefore,  $g_\pi$  is directly related to structural disorder in the inter-chain distance along the stack. Through peak shape analysis of the principal and higher order  $\pi$ -stacking diffraction peaks, deconvolution of the effects of cumulative lattice disorder and finite crystallite size is possible using a model based on that of Warren and Averbach [161, 162]. This allows us to rank structural disorder quantitatively, from a perfectly ordered crystalline lattice ( $g = 0\%$ ) to an amorphous one ( $g \geq \sim 10\%$ ). It has been shown that for semicrystalline polymers, especially those of high molecular weight, the influence of paracrystalline disorder ( $g$ ) dominates the peak shape, thus allowing for single peak-width estimation of  $g$  [160] Fig. 5.4(b) shows an increase in  $g$  with  $M_w$  from  $\sim 6.5\%$  to  $> 8\%$  at  $M_w > M_e$ . It should be noted that for low  $M_w$  oligomers, the observed diffraction line shapes have an increased contribution from finite size effects, causing the single peak-width estimate to loose accuracy. Nevertheless, full peak shape analysis of 3HT-oligomers reveals the  $g$  value from a full fit is less than a factor of two different from that of the estimate, and that the estimate is indeed an overestimation of the  $\pi$ -stacking disorder for oligomeric materials [163], meaning that transition at the entanglement threshold is realistically more pronounced than that shown in Fig. 5.4(b). In addition to the molecular weight dependence of the  $\pi$ -stacking (intermolecular) order, we also extract the inter-chain distance and observe a slight decrease ( $< 2\%$ ) with increasing  $M_w$ , which is faster than the linear decrease in  $\mu$ . We thus find that

in the regime of higher paracrystalline disorder in the  $\pi$ -stacking direction,  $\mu$  is lowest, reflecting an increase in characteristic electron-hole separation. Hence, as  $M_w$  increases, the average electron-hole separation increases as well, leading to a broader distribution of electron-hole recombination rates and a slower power-law PL decay. We attribute this development to an increase in interface area between crystalline and amorphous phases, where the disordered energy landscape is more complex than in crystalline domains.

It is useful to attempt to quantify the characteristic electron-hole separation in different samples based on Fig. 5.4. We do not have a reliable measurement of  $\beta$  in this class of materials, but assuming that  $\beta \sim 1 \text{ \AA}^{-1}$ , which is typical for charge tunnelling in molecular systems [164], then characteristic geminate-pair radii vary from  $\epsilon^{-1} = 1.5 \text{ \AA}$  for films made from 12 kg/mol materials, to  $6.7 \text{ \AA}$  for those fabricated from 348 kg/mol material. For  $\pi-\pi$  stacking distances in these samples,  $\sim 3.8 \text{ \AA}$ , this implies that the average electron-hole separation is less than one nearest-neighbour distance in the lowest  $M_w$  samples, and more than one nearest-neighbour distance in the highest  $M_w$  samples. The paracrystalline disorder thus correlates with the average radius and yield of geminate-polaron pairs, underlining the influence of structural disorder and exciton dissociation processes.

## 5.6 Discussion

The key results of the previous section are that (*i*) the *amplitude* of delayed PL contribution to the integrated PL intensity increases systematically with increasing  $M_w$  in solution-processed films (Fig. 5.3(a)), but drops dramatically in solid-state processed films independent of  $M_w$  (Fig. 5.3(b)); (*ii*) although both the prompt PL spectral lineshape (Fig. 5.2(a)) and the delayed PL decay kinetics (Fig. 5.3(a)) depend unambiguously on  $M_w$  in solution-processed films, there is a striking independence of the delayed PL spectral lineshape on  $M_w$  (Fig. 5.2(b)).

The platform to discuss these observations is our preliminary report in which we concluded that geminate polaron pairs are generated on fast timescales with respect to the exciton lifetime, without significant exciton diffusion, and that these recombine in a distribution of times by quantum tunnelling in the same region in which they were generated [149]. Observation ( i) establishes that as the solid-state microstructure evolves from a polycrystalline morphology (Fig. 5.1(a)) to a two-phase one featuring a higher contribution of chain-entangled, amorphous configurations (Fig. 5.1(b)), the yield of photoinduced geminate polaron pairs increases, and the radial distribution (the distance between the centre of mass of the electron and hole) increases as well. When the microstructure is forced to be predominantly chain-extended by solid-state processing (Fig. 5.1(c)), both the yield and radius distribution of geminate polarons decreases dramatically for all values of  $M_w$ . Furthermore, observation ( ii) establishes that while the contribution of amorphous phases is important for the charge generation yield, states that are re-populated by geminate-pair recombination are characteristic of photophysical aggregates in the lamellar phases, but these aggregates are defined by a high degree of torsional disorder and high average interchain excitonic coupling, evident from the spectral lineshape of delayed PL [64]. Therefore, we conclude that the polymer conformations that constitute regions between ordered crystals and amorphous phases are key in the geminate polaron pair photogeneration mechanisms in neat P3HT. The microstructure dependence on the yield and radius distribution of charge photogeneration that we demonstrate in this communication is likely to be general to semicrystalline semiconductor polymer films. In fact, Labastide et al. showed that P3HT nanoparticles formed by processing from aqueous solution show a marked dependence of delayed PL dynamics with particle size [165], with  $\mu$  increasing with increasing particle diameter, suggesting important microstructure evolution with particle spatial characteristics.

A fundamentally important question that emerges from this interpretation is :

what is the mechanism of this fast branching between self-trapped excitons and geminate polaron pairs in these complex microstructures? A starting consideration is that as this is a neat  $\pi$ -conjugated polymer system and as such is characterized by highly bound Frenkel excitons at equilibrium, there should be no significant driving force for exciton dissociation in the absence of molecular electron acceptors such as fullerene derivatives or chemical defects. In fact, at steady state, the interchain exciton coherence length across the entire  $M_w$  range studied here varies by only  $\sim 20\%$  [64]. The vibrationally dressed exciton density, that is, the electronic excitation that is largely localised on a single chain with the vibrational lattice distortion dressing it, spans 2–4 chains at equilibrium, depending on  $M_w$ . Nevertheless, polaron signatures have also been reported in P3HT neat films [33, 123, 125, 166, 167] and nanoparticles [165] by diverse groups. A possible explanation is that nascent excitons experience substantially longer spatial coherence across different chains on ultrafast timescales [168]. This phenomenon has been invoked to account for ultrafast charge separation in polymer heterostructures [169–171]. On ultrashort ( $<< 100 \text{ fs}$ ) timescales, bath-induced quantum coherence between Frenkel-exciton and delocalized charge-transfer states is possible [172], and its dynamics would be correlated to the dynamic motion of the molecular framework [173]. Transient coherent photoexcitations would branch into the self-trapped excitons inferred from steady-state PL spectra [64], or into geminate polaron pairs, on ultrafast timescales corresponding to decoherence dynamics. The excitation spectrum of delayed PL demonstrates that exciting into states that do not constitute photophysical aggregates in the ground state ( $> 2.4 \text{ eV}$ ) enhances the delayed PL yield [149], and the role of delocalized charge-transfer states coherently coupled to exciton states could be the origin of that phenomenon. Here, the excitation photon energy employed in our measurements is 2.33 eV, which is close to the isosbestic point between photophysical aggregate and non-aggregate absorption [174]. Previous ultrafast PL studies on P3HT films have pointed out the even upon excitation with  $\sim 3\text{-eV}$  photon energy,

well into the non-aggregate absorption range, the transient PL spectrum is characteristic of photophysical aggregates within the experimental instrument response, typically  $\sim 100$  fs [169]. This indicates that even upon excitation well into energy ranges in which chromophores do not ‘feel’ significant intermolecular coupling in the ground state, photoexcitations rapidly relax into photophysical aggregates, on timescales much faster than vibrational relaxation of the chains (whose signatures are evident from transient PL spectra on  $> 10$ -ps timescales [175]). Hot photoexcitations are argued by some to play a crucial role in driving photocarrier generation at polymer donor-acceptor heterojunctions used in photovoltaic diodes [176, 177], and at times  $<< 100$  fs the fate of hot excitons in complex multi-phase P3HT films could mirror that of excitons near heterojunctions in photovoltaic blends. Note however, that we clearly generate tightly bound geminate polaron pairs in neat P3HT, not photocarriers [149], in contrast to polymer blends optimized for photovoltaic diodes. The process of full charge separation at heterojunctions is distinct from photoexcitation relaxation in neat polymer films; here we only argue that the nature of the transient coherent excitation following the first few femtoseconds after light absorption, and the local chain conformations hosting them, might be what drives branching into predominantly charge-transfer-like excitations. *Direct* spectroscopic probes of spatial coherence of these highly transient states remains an important challenge for the ultrafast spectroscopy community concerned with the photophysics of plastic semiconductors, but may be probed by multidimensional spectroscopies [178].

Perhaps a more banal but plausible explanation of the microstructure dependence of delayed PL phenomena reported here involves chemical defects, likely arising from photo-oxidation of P3HT. Majewski et al. have reported that degradation of field-effect transistors based on P3HT show marked kinetics depending on processing conditions, and attributed the differences to the extent to which water and oxygen diffuse to crystalline/amorphous interfaces due to differences in micro-

structure [179]. As the volume fraction of amorphous regions of the film increases with  $M_w$ , it is possible that the density of dopants at interfaces also increases, producing a higher amplitude of delayed PL in our samples. We cannot rule out this possibility, although it is unclear why the decay kinetics would depend on  $M_w$  in this scenario. However, even if dopant-induced quenching accounts to a substantial extent for the delayed PL dynamics reported here, the same fundamental semiconductor polymer science issues stand : there is a clear relationship between solid-state microstructure and exciton quenching dynamics, and two-phase microstructures enhance this process due to the complex energy landscape intrinsic to these disordered architectures. This complexity can then be generalized to binary systems involving electron acceptor moieties.

Reid et al. reported time-resolved microwave conductivity measurements on the same  $M_w$  series and processing routes (Fig. 5.1) as reported here [157], allowing direct comparison with this work. Those measurements were carried out at room temperature and probe photocarriers, in contrast to the tightly-bound charge pairs probed by our delayed PL measurements at 10 K [149]. Nevertheless, that data show that the yield of photocarriers increases with increasing molecular weight in the paraffinic regime (Fig. 5.1(a)) and saturates at the transition into the entangled, semicrystalline regime (Fig. 5.1(b)). The main conclusion was that the evolution of semicrystalline microstructure with well-defined interfaces between amorphous and crystalline polymer domains is necessary for spatial separation of the electron and hole, which controls the yield of free charges. We consider that there is a general conclusion to be drawn from both types of optical probes involving the importance of solid-state microstructure on electronic dynamics in semicrystalline organic semiconductors. The development of chain configurations defining two-phase semicrystalline microstructures define a complex disordered energetic landscape that influences the branching of transient photoexcitations into charge separated states.

In classical polymer science, understanding of the complex architectures formed

by high- $M_w$  macromolecules is essential because many of the properties of bulk commodity “plastics” are dictated by two-phase morphologies of long-chain polymers. The development of mechanical properties with  $M_w$  is fundamentally no different in P3HT than in common plastics, and electronic properties such as charge transport display a corresponding development [152]. Here we have demonstrated that excitonic processes in neat P3HT are also profoundly dependent on microstructure via  $M_w$  and processing routes, and we consider that this is a general property of plastic semiconductors.

## 5.7 Conclusions

By means of time-resolved PL spectroscopy at 10 K, we have explored geminate-polaron-pair yields and their recombination dynamics in films composed of neat P3HT of varying  $M_w$ , and processed either from solution or in the solid state. Over the range of  $M_w$  studied, the solid-state microstructure varies from polycrystalline (one-phase) to semicrystalline (two-phase crystalline/amorphous). The yield of photogenerated geminate polaron pairs, their distribution of radii (the separation between electron and hole), and their distribution of recombination rates depends sensitively on the nature of the microstructure. These findings illustrate that the key consideration to determine electronic properties in semicrystalline polymeric semiconductors is to control the solid-state microstructure by appropriate choice of molecular weight and by processing routes.

## 5.8 Experimental Methods

### 5.8.1 Polymer processing

P3HT films of weight-average molecular weight in the range of 12.3, 48, 208, 265, and 348 kg/mol were investigated. All materials have similar regioregularity but the polydispersity is, respectively, 1.7, 1.8, 2.6, 2.1, and 3.7. Samples were

processed in two different ways. Firstly, they were wire-bar-coated from p-xylene solution (1.4% by wt) on glass substrates. The solution and substrate temperature was 70 °C. Throughout this paper, we refer to samples processed this way as “solution-processed” films. Alternatively, they were pressed from powder as described elsewhere [145], and these samples are described here as “solid-state-processed” films.

### 5.8.2 Photoluminescence spectroscopy

Time-resolved PL measurements were carried out with a 40-fs, 532-nm (2.33-eV) pulse train derived from an optical parametric amplifier (Light Conversion TOPAS), pumped by a Ti :sapphire laser system (KMLabs Dragon, 1-kHz repetition rate). Maximum pump fluences were  $5 \mu\text{J cm}^{-2}$ . Spectra were measured with an intensified CCD camera (Princeton-Instruments PIMAX 1024HB) coupled to a 300-mm spectrometer (SP2300i, Princeton Instruments), with a 5-ns electronic gate synchronized to the pulse train. Time-resolved PL spectra were obtained by varying the gate delay and temporal width electronically with respect to the laser-pulse arrival time. All time-resolved PL spectra were corrected for the instrument response of our spectrometer.

### 5.8.3 Wide-angle X-ray scattering

X-ray scattering experiments were performed at the Stanford Synchrotron Radiation Lightsource (SSRL) on beamline 7-2 (high-resolution grazing incidence), with an incident energy of 8 keV. The diffracted beam was collimated with 1 mrad Soller slits for high-resolution in-plane scattering. For grazing incidence experiments, the incidence angle was slightly larger than the critical angle, ensuring that we sampled the full film depth. All synchrotron X-ray scattering measurements were performed under a He atmosphere to reduce air scattering and beam damage to the sample. Full Warren Averbach peak shape analysis and single peak estimates

of grazing incidence diffraction peaks were performed as detailed elsewhere [163].



## CHAPITRE 6

# INFLUENCE OF MICROSTRUCTURE ON GEMINATE POLARON SPATIAL DISTRIBUTION IN SEMICRYSTALLINE POLYMERIC SEMICONDUCTORS.

### 6.1 Contexte de l'article

Les résultats des chapitres 4 et 5 indiquent la présence de paires de polarons localisés dans des régions spécifiques de nos films de P3HT, soit aux interfaces entre les domaines cristallins et amorphes. Cette conclusion est tirée suite à l'analyse de la forme spectrale en photoluminescence et de la dynamique de recombinaison des excitons dans des régions cristallines plus désordonnées moléculairement.

Dans ce chapitre, nous sondons la présence de polarons via des techniques de type pompe-sonde, notamment l'absorption photo-induite en continu ainsi que l'absorption transitoire. Ces techniques nous permettent de sonder l'absorption d'une lumière, induite par la présence des excitations dans le matériau. Ceci nous renseigne notamment sur le spectre d'absorption de l'état excité. Les résultats présentés nous permettent de déterminer que la photogénération des paires de polarons se fait sur des échelles de temps sous la nanoseconde, dans des régions où les chaînes de polymères sont plus désordonnées que celles présentes dans le volume des domaines cristallins. Les résultats présentés mettent une fois de plus l'emphase de l'importance de la semi-cristallinité et du rôle des interfaces dans la formation de ces paires de polarons.

### 6.2 Contribution originale de chaque coauteurs

Francis Paquin a pris tous les résultats expérimentaux (à l'exception des mesures d'absorption transitoire par Paul-Ludovic Karsenti), fait l'analyse de ceux-ci et a

écrit le texte. Carlos Silva a apporté des corrections mineures au manuscrit final.

Francis Paquin,<sup>1</sup> Paul-Ludovic Karsenti,<sup>1</sup> Natalie Stingelin,<sup>2</sup> and Carlos Silva,<sup>1</sup>

<sup>1</sup>*Département de physique & Regroupement québécois sur les matériaux de pointe,  
Université de Montréal, C.P. 6128, Succursale centre-ville, Montréal (Québec)  
H3C 3J7, Canada*

<sup>2</sup>*Department of Materials and Centre for Plastic Electronics, Imperial College  
London, South Kensington Campus, London SW7 2AZ, United Kingdom*

(To be submitted to Journal of Polymer Science B)

### 6.3 Abstract

We address the influence of the weight-average molecular weight ( $M_w$ ) of the neat polymeric semicrystalline semiconductor poly(3-hexylthiophene) on the spatial distribution of photogenerated geminate polaron pairs. In previous studies, we have shown that films processed from low  $M_w$  ( $< 50 \text{ kg/mol}$ ) P3HT forms aggregates of cofacially stacked extended chains with characteristically higher torsional disorder than in higher  $M_w$  material. In the latter, the solid-state morphology is semicrystalline and comprised of crystalline domains embedded in an amorphous matrix of entangled chains. By means of quasi steady-state photoinduced and transient absorption spectroscopy, we show compelling evidence that in films of  $M_w \sim 50 \text{ kg/mol}$ , ultrafast geminate polaron pairs formation occurs in more molecularly disordered regions of the aggregates, with a ground-state bleach signature typical of low  $M_w$  material. The deep modulation of the steady-state photobleaching reveal qualitative information on the  $M_w$ -dependence of the spatial distribution geminate-polaron-pair separation. We address the significant role of semicrystallinity and ordered/disordered interfaces in the process of charge separation in semicrystalline polymeric semiconductors.

## 6.4 Introduction

The optoelectronic properties of polymeric semicrystalline semiconductors are known to be intimately interconnected to their morphology, which in turn is largely defined by the degree of molecular packing of the polymer chains. For example, it is well known that materials such as regiorandom poly(3-hexylthiophene), rr-P3HT, poorly aggregates which results in amorphous films with characteristic charge mobilities that are six orders of magnitude lower than in the typical regioregular P3HT (rr-P3HT). [180] In contrast, the electronic properties in rr-P3HT critically depends on multiple parameters such as the processing method, [16, 18, 152] the choice of solvent, [75] and the molecular weight. [19, 27, 32, 83, 108, 152] The latter is responsible for interesting crystallisation behavior in thin films. [152]

Indeed, it is known that low weight-average molecular weight ( $M_w$ ) rr-P3HT tends to be polycrystalline, comprised of 2D lamellae of chain-extended molecules with higher torsional disorder than in films of  $M_w$  higher than the molecular weight between chain entanglement. [19] In this higher  $M_w$  regime ( $>50$  kg/mol), the morphology is characterised by crystalline domains embedded in a network of entangled polymer chains. [19] From this ensues important morphological dependence of chain packing and order on the optoelectronic properties. For example, charge transport is known to be heavily impacted by the choice of  $M_w$ . Indeed, there has been experimental evidence of the increased field-effect mobilities with molecular weight in P3HT thin films up to  $\sim 40$  kg/mol. [19, 30, 81–83] after which saturation occurs. On the other hand, bulk mobilities trends differ from different groups but are shown to exhibit a decrease at high  $M_w$ . [19, 84] Importantly, these results depend strongly on the film processing route, and it is clear that the role of the interfaces between crystalline and amorphous domains in higher  $M_w$  material seem to be important.

In this paper, we address the role of the polymer molecular weight on the spatial distribution of geminate polaron pairs generated upon photoexcitation. Full

separation of such tightly bound species is one of the crucial step in achieving high yield of charge formation in bulk heterojunction solar cells. [181] In previous papers, [149, 182] we have argued that exciton separation in neat polymeric semicristalline semiconductors occurs at the gradual interface between molecularly ordered and disordered domains and forms tightly bound geminate polaron pairs which total yield of formation is dictated by the surface area of interfaces, [149] an aspect that can be controlled for example by varying the molecular weight of the material. [182] Moreover, we have also shown that the follow up event is the radiative recombination of those charge pairs, a process that occurs as a result of quantum mechanical tunneling of the electron and hole accross the interface. This yields long-lived photoluminescence (PL) with spectral signatures that indicate that recombination occurs in more molecularly disordered regions than what is found in the bulk of the aggregates. We found that the yield and the lifetime of this long-lived ( $> 10\text{ ns}$ ) PL depend profoundly on the microstructure impacted by the choice  $M_w$  and processing route. In the high  $M_w$  films, we attributed the slower decay of the delayed PL to a larger average electron-hole spatial distribution of geminate polaron pairs, and the yield of recombination to the surface area of cristalline/amorphous interfaces. We have shown, along with other groups, that the surface area can be controlled by varying the molecular weight [182] and/or processing route. [182, 183] The goal of this paper is to support, via pump-probe spectroscopy techniques, that charge photogeneration in thin films of P3HT occurs under ultrafast timescales in more molecularly disordered regions of the film, and to show evidence of the  $M_w$ -dependent signature of their spatial distribution. We find that the early time ground-state bleach signature in the transient absorption spectrum of a thin film of  $M_w=48\text{ kg/mol}$  carries the signature of the absorption of low- $M_w$  material, hence demonstrating that molecularly disordered segments of the aggregates are responsible for the efficient polaron pairs formation.

## 6.5 Results

### 6.5.1 Absorption

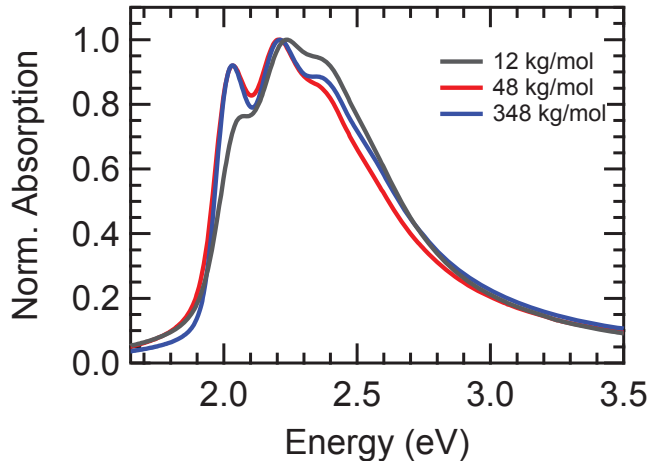


Figure 6.1 – Room temperature absorption spectra of thin films of neat P3HT for different molecular weight indicated in the figure. (Figure adapted from ref. [64])

Fig.6.1 displays the room temperature absorption spectra of films of P3HT of  $M_w=12, 48$  and  $348 \text{ kg/mol}$ . Within this range, the contribution of the crystalline domains as measured on the same material and processing by another group accounts for  $>50\%$  of the total absorption. [18] We point out the difference in the intensity of the origin of the vibronic progression at  $2.0 \text{ eV}$  for the low and high  $M_w$  films. Spano et al. has shown that the absorption spectrum of thin films of P3HT can be understood in the framework of a weakly coupled H-aggregate model. [60, 66] In this model, weak resonance Coulomb interactions,  $J_{\text{inter}}$ , between cofacially stacked polymer chains in the crystalline regions leads to electronic dispersion of the vibronic molecular levels, thus forming a band with free exciton bandwidth  $W = 4J_{\text{inter}}$ . In another paper, [64] we have followed the work of ref. [62] and extracted  $W$  from the ratio between the  $0-0$  ( $2.0 \text{ eV}$ ) and  $0-1$  ( $2.2 \text{ eV}$ ) transitions in the absorption spectrum of Fig.6.1.

Our previous analysis [64] gave  $W \approx 80$  meV for the 12 kg/mol film compared to  $W \approx 20$  meV for  $M_w > 48$  kg/mol. The strength of the excitonic coupling is known to exhibit strong variation with conjugation length, [16, 93] with the latter being greatly impacted by the morphology that the chains adopt in thin films. In this specific case, the disparity between  $W$  in high and low- $M_w$  films can be accounted for the different morphology adopted above and below the molecular weight resulting in chain entanglement ( $\sim 50$  kg/mol). In previous paper, we have shown that the specific microstructure adopted by films of different molecular weight not only regulate the coherence length of excitons in the crystalline regions, [64] but also impacts the charge separation and recombination dynamics of excitons into geminate polaron pairs in the material, [182] an important result that will be covered in the discussion section. Also, Clark et al. have shown that the degree of intramolecular order can be tuned by using the proper choice of solvent for solution processed films. [75] We thus conclude that the results of Fig.6.1 are consistent the lower excitonic coupling expected in the higher  $M_w$  material as a result of increased planarity of the chains.

### 6.5.2 Steady-state photoinduced absorption

Excitation of thin films of P3HT yields both excitons and polaron pairs under ultrafast timescales ( $< 100$  fs), [34, 35] a process typically monitored via transient absorption spectroscopy. One can also draw important conclusions from steady-state measurements. In Fig.6.2(a), we show the ground-state bleach (GSB) of the continuous-wave photoinduced absorption spectrum (cw-PIA) at  $T=10$  K, for the films of different molecular weight presented in Fig.6.1. We observe a deep modulation of the GSB signal that closely resembles the first derivative of the absorption spectrum, as shown in Fig.6.2(b). The signature of the cw-PIA bleaching spectrum is complex and results from a change in the absorption spectrum of the excited state caused by the quasi steady-state population of excitons and polarons photo-

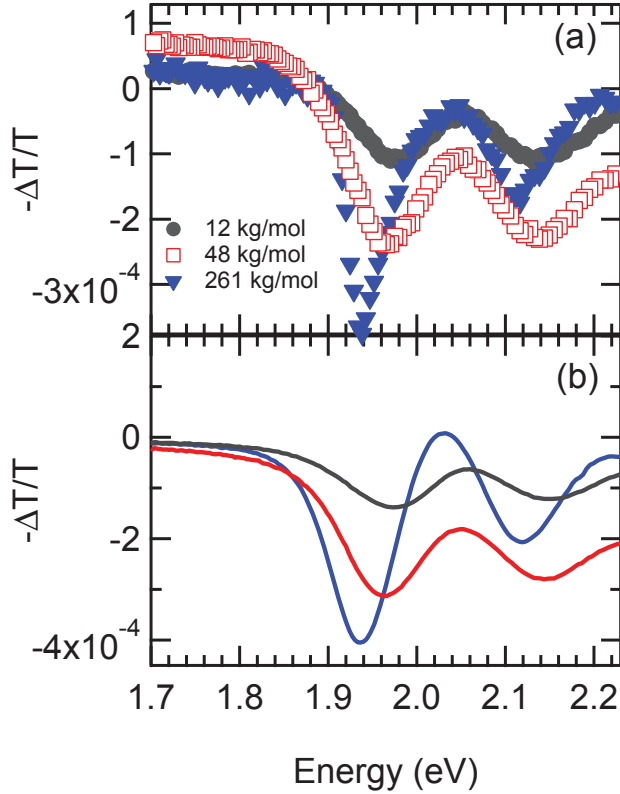


Figure 6.2 – (a) Quasi-steady-state photoinduced absorption spectra at  $T=10$  K in thin films of neat P3HT of different molecular weight indicated in the figure. (b) Fit of the spectrum in (a) with  $-\frac{\Delta T}{T} = a_0 A(\nu) + b_0 \frac{dA(\nu)}{d\nu}$  with  $b_0 \gg a_0$ .

generated upon excitation, with the latter showing a characteristic photoabsorption signature around 1.25 eV (see supplemental information III). [34, 52, 184] At steady-state, the GSB is a mixture of the absorption spectra of all the sites hosting the excitations, with their molecular ordering differing for different molecular weight. Seifried et al. have observed the same absorption first derivative-like spectral signature of the photobleach in the transient spectrum of P3HT under high pulse fluence. [185] In their report, the modulation of the bleaching spectrum was assigned to both photoexcited states and a thermal effect which causes a blue-shift of the ground-state absorption spectrum. They also observe an associated increase in

the highest energy transition (1.94 eV) with an increased photon flux and a diminished absorption band at 1.25 eV caused by subnanosecond bimolecular annihilation of polarons. [185] To rule out a thermal heating effect as the main source of the modulation of the GSB signal of Fig.6.2, we have also undertaken cw-PIA measurements on substrates of different thermal conductivity (supplemental information III); specifically : fused silica ( $\sim 1.4 \text{ W/K m}$ ) and ITO ( $\sim 12 \text{ W/K m}$ ) and observe no difference in the lineshape, hence eliminating the thermal effect as the main contribution of the shift of the absorption spectrum in the excited state. We suspect that the strong modulation of the GSB signal is a result of a linear Stark shift of the molecular transition, reminiscent of spatially distributed geminate polaron pairs, with a typical signature almost identical to what is observed by Vardeny et al. in the electroabsorption spectrum of neat P3HT films. [34] Such modulation of the GSB has also been observed in the PIA spectrum of dye-sensitized solar cell with similar conclusion, i.e as a results of the electric field existing between the positive charges on the oxidized dye and the injected electron in  $\text{TiO}_2$  particles. [186] In our case, we speculate that this Stark shift is caused by a built-in local electric field resulting from a significant population of long-lived polaron pairs at the interface between molecularly ordered and disordered regions of the film. To exploit the idea that this occurs in such regions of the film, we proceed to study the evolution of the GSB via transient absorption spectroscopy.

### 6.5.3 Transient-absorption spectroscopy

The transient absorption (TA) spectrum of a thin film of P3HT of average  $M_w=48 \text{ kg/mol}$  at  $T=10 \text{ K}$  is shown in Fig.6.3(a). In Fig.6.3(b), we show slices of the spectrum at two different times indicated in the figure. The TA spectrum can be complex as there usually exist significant overlap between stimulated emission, photoabsorption and ground-state bleach bands. Nevertheless, the negative broad absorption band around 1.9 eV is consistant with the formation of early polaron

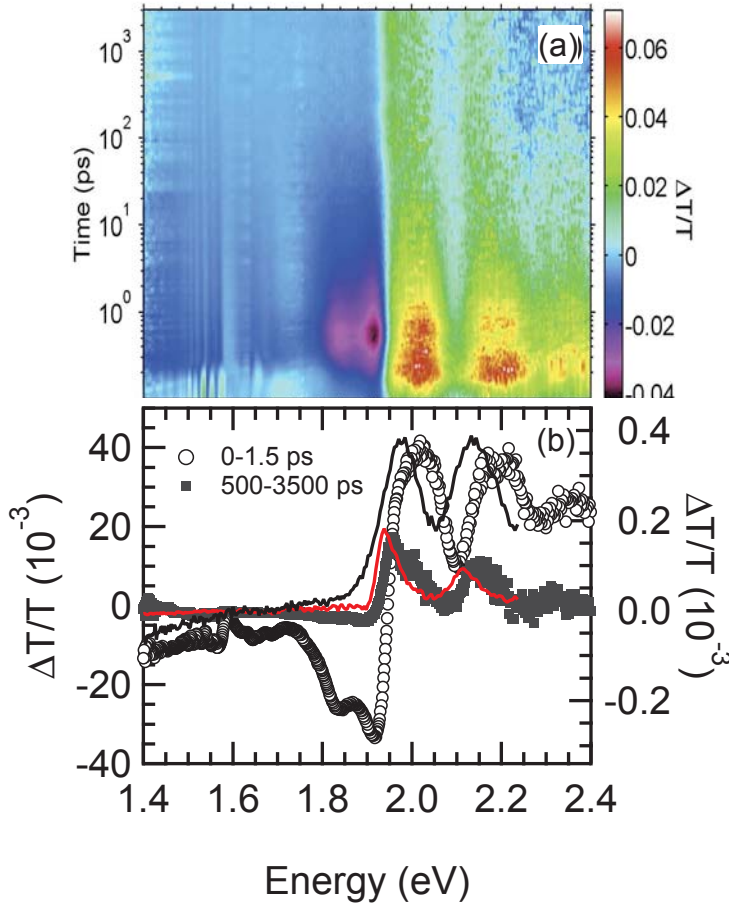


Figure 6.3 – (a) Transient absorption spectrum of neat P3HT of  $M_w=48$  kg/mol measured at  $T=10$  K with a pump photon energy of 2.33 eV. (b) Integrated transient signal at times indicated in the figure (symbols). Also shown is the steady-state photoinduced absorption spectra of low (12 kg/mol, black curve) and high (348 kg/mol, red curve) molecular weight film at  $T=10$  K.

pairs in the film. [35, 187] The presence of the peaks around 1.70 eV and 1.87 eV are a result of stimulated emission which overlaps the absorption band. We note that the early time ( $<1.5$  ps) photobleach spectrum above 1.95 eV closely resembles the quasi-steady state photobleach of the low  $M_w$  (12 kg/mol) film. At longer timescales (integrated from 0.5 to 3.5 ns) the bleach spectrum is red-shifted and resembles the cw-PIA of the higher  $M_w$  (348 kg/mol) material. This result is interesting given

the fact that  $M_w \approx 50 \text{ kg/mol}$  is close to the molecular weight between entanglement ( $M_e$ ) for P3HT. [19] This specific signature in the TA spectrum shows that in films with  $M_w \sim M_e$ , early formation of photoexcited states occurs in more molecularly disordered regions of the films, specifically on chains with shorter conjugation lengths. This result corroborates previous studies which puts emphasis that the early formation of charge pairs occurs in regions with different molecular packing configuration than observed in the bulk of the aggregates. [120, 136, 188, 189] Even if the fluence is much lower than in Ref. [185], we cannot rule out completely the possibility of a contribution of thermal heating of the sample in the signature of the GSB of our TA. Our conclusions are drawn simply on the similarity of the spectral shape of the TA and cw-PIA of the high and low  $M_w$  films. In any case, the presence of the polaron absorption band indicates that there is significant contribution to the GSB by efficient photogeneration of long-lived electronic excitations.

## 6.6 Discussion

From the work of the previous section, we identify that the microstructure of thin films of P3HT can be controlled via the molecular weight and we note that the early formation of geminate polaron pairs occurs in regions of the aggregates that are more molecularly disordered, possibly near the interface between ordered and disordered regions. Excitation at 2.33 eV of a film of P3HT of  $M_w = 48 \text{ kg/mol}$  excites both amorphous and crystalline regions in the film [149] and yields excitons and geminate polaron pairs under ultrafast timescales ( $\sim 150 \text{ fs}$ ). [34, 35] The photobleaching spectrum reveal that within the resolution of the experiment, those tightly bound charge pairs are photogenerated in regions with a morphology similar to low molecular weight polymers, i.e aggregates with reduced intramolecular and concomitant increased intermolecular order. The complex energical landscape at such interfaces plays a crucial role in the formation and dynamics of long-lived

charge pairs in polymeric semicrystalline semiconductors.

In a previous paper, [149] we have studied the photoluminescence (PL) decay dynamics of films of P3HT of molecular weight in the same range that is presented here. In all films, we observed long-lived ( $>10$  ns) PL that account for  $>10\%$  of the total emission, in a way that depends with the molecular weight. We assign this delayed PL to recombination of geminate polaron pairs near the interface between molecularly ordered and disordered regions. [149, 182] The slower decay of this long-lived PL in high  $M_w$  films was assigned to a larger distribution of radii of electron-hole pairs localised at the interface. We also attributed the higher % of delayed PL observed in high  $M_w$  films to a larger surface area between ordered and disordered domains. The conclusions that we draw from the dynamic change in the lineshape of the TA spectrum of Fig.6.3 is consistent with other studies. In fact, different groups have shown that polaron pairs photogeneration are limited to specific domains, possibly where chains are more torsionally disordered and kinked and that the process of exciton separation into geminate polaron pairs is driven by the energetic disorder between polymer chromophores. [136, 188, 189] Here, we show that this occurs in regions with higher degree of conjugation breaks. Zen et al. have shown compelling evidence that the strong relationship between the mobility of charges with molecular weight is largely hindered by conjugation breaks of the backbone, which reduces the hopping rate. [21] Hence, there should exist a tradeoff between a good amount of ordered/disordered interfaces necessary for the formation of long-lived charge pairs and higher average intramolecular order for increased average electron-hole radii. The latter being beneficial for efficient separation.

In this work, we use the same batch of material that was used in the work of Ref.[18]. In their studies, the presence of long-lived polaron is observed via time-resolved microwave conductivity measurements (TRMC) with yield and decay dynamics that depends strongly on the molecular weight. The TRMC spectrum reveal higher yield of charges at higher molecular weight with a saturation around

$M_w \approx 50 \text{ kg/mol}$ , consistant with the transition from non-entangled paraffinic-like to entangled, semicrystalline morphology. The authors point out the importance of well-defined interfaces between cristalline and amorphous domains in efficient separation of electron and holes in the material and speculate that the electrons are trapped at the interface whereas the holes finds host in the cristalline regions with lower site energy. If this is the case, the density of electrons trapped at the interface and holes in the cristalline region could lead to a short-range local electric field giving rise to the specific signature that we observe in the GSB of Fig.6.2 and 6.3, consistant the Stark effect that we propose. Such field could assist the separation of tightly bound electron-hole pairs to fully separated charges.

The results of Reid et al. also points out that only carriers that are generated at the interfaces between ordered and disordered domains can survive up to nanoseconds. This is also consistant with transient absorption imaging experiments in the efficient photovoltaic blend of P3HT :PCBM, where direct excitation at the interface between domains of P3HT and PCBM, in regions that are considered more disordered than the bulk of the aggregates is responsible for the high yield long-lived charge-pairs. [119] Hence manipulating independantly the morphology at interfaces and in the bulk of the aggregates can be regarded as one important tool for optimised polaron formation and subsequent separation in free carriers. This could be achieved by carefully intermixing phases of low and high- $M_w$  polymers as was attempted in Ref.[110].

Finally, our contribution to the understanding of the dependance of the morphology on geminate polaron pair fomation can be imbricated in the work of Koch et al. [19] which demonstrates increased field-effect mobilities in thin P3HT films up to 25 kg/mol. In their study, this mobility is limited by the thin-film architecture at low- $M_w$ . Above the threshold for chain entanglement, this mobility is maximised as a result of the interconnectivity between cristalline domains bridged by long polymer chains. The bulk mobility that they observe via time-of-flight technique

is more complex and is maximised at 4.8 kg/mol. Increasing the lamellar thickness via a high-pressure crystallisation process has been demonstrated to augment the bulk mobility by orders of magnitude. This shows that not only the choice of molecular weight, but the processing method also greatly impacts the optoelectronic properties in semicrystalline polymers.

## 6.7 Conclusion

Geminate polaron pairs formation in P3HT occurs at the interface between ordered and disordered regions and give rise to a complex spectral signature in the transient photobleach spectrum. The microstructure can be controlled by variation of the molecular weight of the polymer and we find that for an average  $M_w$  of 48 kg/mol, the early time photobleach signature in the transient absorption spectrum is similar to what is found at steady-state in low molecular weight polymers. This demonstrates that polaron formation occurs in more molecularly disordered regions of the aggregates. Also, the deep modulation of the photobleach closely resemble the first derivative of the absorption spectrum, a behavior that we associate with a linear stark effect caused by the local electric field generated from spatially distributed charge pairs. Our results show the importance of controlling the interfaces between crystalline and amorphous regions for efficient charge photogeneration in semicrystalline polymers.

## 6.8 Experimental Methods

### 6.8.1 Polymer processing

Films of P3HT of molecular weight in the range of 12, 48, 348 kg/mol were wire-bar-coated from p-xylene solution at a concentration of 1.4% by wt on glass substrate. The films and substrates were kept at 70°C. Films of  $M_w=48$  kg/mol were dropcast on spectrosil and ITO substrates from a chloroform solution (1 mg/ml).

The film and substrate were kept at 50°C.

### 6.8.2 Absorption measurement

The absorption spectra were measured at room temperature with a UV-Vis spectrophotometer (Perkin Elmer, Lambda25)

### 6.8.3 Photoinduced absorption measurement

Photoinduced absorption experiments were carried out by excitation with a continuous-wave laser (Ultralasers Inc., 200mW maximum, 532 nm) modulated at a frequency of 170 Hz with a mechanical chopper (Terahertz Technologies). An halogen lamp was sent through a spectrometer (Princeton Instruments, SP2300i) and modulated at 139 Hz to be used as a probe. The PIA signal was acquired by phase-sensitive detection : The probe was sent to one lock-in amplifier (SR810, Stanford Research Systems) and used to normalise the change of transmission. The latter was acquired by monitoring the PIA signal at the sum frequency (309 Hz) on a second lock-in amplifier (SR830, Stanford Research Instrument). The samples were housed in a closed-cycle, temperature controlled cryostat (CryoIndustries of America).

### 6.8.4 Transient absorption measurement

TA measurements were carried out by exciting the sample with a femtosecond laser pulse train (2.33 eV, 1 KHz) at a fluence of  $3.6 \mu\text{Jcm}^{-2}$  and probed with a single-filament white-light continuum generated from the fundamental (780 nm) of the Ti :Sapphire laser in a sapphire window.



## CHAPITRE 7

### CONCLUSION

Les travaux présentés dans cette thèse tentent d'éclaircir la relation intime entre la microstructure et les propriétés excitoniques dans les polymères semi-conducteurs semi-cristallins. Pour élucider ces attributs complexes, nous avons principalement sondé la dynamique de recombinaison des excitations neutres primaires et des paires de polarons successivement formées dans des films minces de poly(3-hexylthiopène). La nature de ces excitons et la dynamique associée à leur séparation en paires de charges fortement localisées, ainsi que leur recombinaison successive dépend en grande partie du procédé de fabrication du film ainsi que du poids moléculaire des chaînes de polymère. Les conclusions que nous avons précisées dans ce document sont générales à la grande classe des polymères semi-conducteurs semi-cristallins. Nous faisons ici une revue des travaux des articles présentés dans les chapitres précédents en les mettant en contexte avec la littérature récente.

Les polymères semi-conducteurs sont des matériaux malléables et le débat est toujours ouvert sur les limitations (optiques et électroniques) liées à la morphologie des films minces. Par exemple, il est connu que l'auto-empilement des chaînes P3HT de faible poids moléculaire (<50 kg/mol) engendre une formation de domaines polycristallins où les chaînes de polymères sont étendues, mais torsionnellement plus désordonnées que les chaînes de plus haut poids moléculaire. Les différents agrégats se retouchent abruptement, ce qui engendre une dislocation du réseau cristallin. Au-delà du poids moléculaire où les chaînes tendent à s'emmêler sur elles-mêmes, la microstructure est gouvernée par ces mêmes cristaux qui sont imbriqués dans une matrice de chaînes amorphes où certaines molécules servent de pont entre les domaines cristallins avoisinants. Cette microstructure cristalline particulière a un impact profond sur les propriétés des excitations générées suite à l'absorption

de photons.

À basse température ( $T = 10\text{ K}$ ), les excitons photogénérés se recombinent radiativement dans les domaines cristallins, donnant une signature optique qui nous renseigne sur leur cohérence spatiale. La cohérence de ces ondes d'excitation est bidimensionnelle et anisotrope dans la direction des chaînes et perpendiculairement à celles-ci (dans la direction de l'empilement des chaînes). Cette anisotropie relève du fait que la force du couplage excitonique intermoléculaire et intramoléculaire montre aussi une anisotropie qui dépend du poids moléculaire et de l'agencement des chaînes. La signature optique qui découle de la recombinaison des excitons dans les agrégats formés à partir de matériaux de plus haut poids moléculaire est compatible avec une plus grande planarité moyenne des chaînes dans les agrégats. Dans cette limite de haut poids moléculaire ( $>50\text{ kg/mol}$ ), la cohérence spatiale des excitons le long de l'axe de l'agrégat est d'environ 4.5 unités de thiophène tandis que la cohérence le long de la chaîne est plus faible et d'environ 2 unités de thiophène. Inversement, dans les agrégats formés de chaînes où  $M_w < 50\text{ kg/mol}$ , la cohérence spatiale le long de la chaîne est réduite d'environ 30% et augmente d'environ 25% le long de l'agrégat. Bien que la nature du couplage inter et intramoléculaire se charge de délocaliser l'exciton dans le cristal, le désordre énergétique joue le rôle d'agent localisateur sur les excitations. Ces résultats diffèrent largement avec la signature optique des excitons dans les longs agrégats moléculaires planaires et ordonnés où la cohérence peut atteindre des micromètres. [67] Il est alors envisageable de considérer une façon ingénieuse de manipuler l'agrégation de molécules et contrôler l'interaction des chaînes, par exemple en ajustant le décalage entre ces dernières, permettant par le fait même d'ajuster la force du couplage inter et intramoléculaire. Ce type d'idée est déjà exploitée théoriquement pour le P3HT en étudiant l'effet du décalage longitudinal entre les chaînes d'un agrégat, permettant de réguler le caractère d'agrégats-H ou J. [190]

Les études sur la dynamique des espèces photoexcitées dans les films de P3HT

démontrent qu'une fraction significative de ces excitations primaires peuvent se scinder en paires de charges localisées, sous des échelles de temps ultrarapides ( $\sim 150$  fs), [33–35] compétitionnant avec le processus de conversion interne typiquement observé dans les matériaux organiques. Nos résultats démontrent que lorsqu'on excite le matériau avec une impulsion dont l'énergie est supérieure à l'énergie de la bande interdite ( $E_{\text{exc}} \approx 2.25$  eV), ces excitons génèrent des paires de charges fortement localisées aux interfaces entre les domaines cristallins et les régions amorphes. La population de ces états sombres peut se faire via l'état excitonique "chaud" ou relaxé. Le modèle dynamique proposé avance que ces paires de polarons se recombinent de façon géminale et par effet tunnel. Cette recombinaison passe par l'état excitonique de plus basse énergie, avec une signature caractéristique d'agrégats plus désordonnés et donne lieu à de la photoluminescence sur des échelles de temps  $> 10$  ns, au-delà du temps de vie intrinsèque de l'exciton primaire. Le taux élevé de recombinaison à long temps de vie dans les films de P3HT où  $M_w = 348$  kg/mol,  $> 40\%$  vs  $\sim 5\%$  pour  $M_w = 12$  kg/mol est consistant avec une aire d'interface de domaines cristallins/amorphes supérieure à haut poids moléculaire. Ces résultats diffèrent de ceux de films de P3HT produits par compression du polymère, dans lesquels les régions amorphes sont quasi inexistantes et le taux de génération de polarons pratiquement nul. Dans ce cas, la photoluminescence à long temps de vie est négligeable. De plus, la dynamique plus lente de la recombinaison des paires de charges des films où  $M_w > 50$  kg/mol est expliquée, selon le modèle dynamique, par une distribution plus étalée de rayons de ces paires de charges. Ceci pourrait faciliter leur dissociation en électrons et trous libres. Ces résultats ont une importance fondamentale au niveau de la compréhension des mécanismes limitant la séparation de charge dans les matériaux semi-cristallins, puisque la recombinaison des paires de polarons géminales compétitionne avec leur séparation en paire de charges libres dans les dispositifs optoélectroniques.

L'énergie supplémentaire accumulée par les excitons durant les premières fem-

tosecondes de leur existence leur confère des propriétés intéressantes. Nos résultats des chapitres 4 et 5 sont compatibles avec ceux de plusieurs groupes, i.e la photogénération intrinsèque efficace de charges dans les polymères conjugués peut se produire suite à une excitation d'énergie supérieure à celle de la bande interdite, possiblement avant la dissipation d'excès d'énergie. [149, 191, 192] Ceci vient ternir l'image standard de la dissociation d'excitons, soit celle d'un processus qui s'effectue suite à la thermalisation des excitons vers le bas de la bande. De plus, plusieurs résultats récents mettent l'accent sur l'importance des excitons "chauds". Par exemple, dans des matériaux de faible bande interdite tel que le PCPDTBT mélangés avec du PC<sub>60</sub>BM, la dissociation d'excitons crée des états à transfert de charge aux interfaces ainsi que des polarons. [177] Cependant, lorsque l'énergie de l'excitation surpassé celle de la bande interdite, elle n'est pas perdue par dissipation, mais sert plutôt à peupler des états à transfert de charge chauds (de plus haute énergie), qui eux permettent la formation de polarons délocalisés. Ce n'est pas l'excès d'énergie en soi qui est important, mais plutôt le fait que ces états chauds démontrent un degré de délocalisation supérieur à celui atteint par une excitation d'énergie de l'ordre de la bande interdite. [193] Ces résultats peuvent aussi être rationalisés suite aux travaux présentés au chapitre 3. Nos mesures démontrent qu'il subsiste une réorientation des chaînes de P3HT suite à une excitation. Cette réorientation tend à rendre les chaînes planaires dans l'état excité, engendrant possiblement une délocalisation plus prononcée des excitations le long de la chaîne. Cette déformation géométrique pourrait aussi contribuer à l'agencement des états singulets avec ceux à transfert de charge sur des échelles de temps compétitionnant avec la conversion interne d'énergie.

Dans les polymères semi-cristallins, les barrières énergétiques qui se forment entre les domaines cristallins et des régions amorphes piègent les paires de polarons. Ces derniers peuvent se recombiner par effet tunnel. Bien que nous nous intéressons principalement à la recombinaison des excitations, une récente publication dans le

journal Nature fait objet du transport des polarons libres dans plusieurs polymères semi-conducteurs. [194] Ces travaux démontrent que la théorie de Marcus décrivant le transfert des excitations fait défaut à basse température et que le transport des polarons se fait aussi par médiation de l'effet tunnel médié par les modes de vibration intermoléculaires, et ce, indépendamment du polymère étudié. Notre apport scientifique démontre que ce processus contrôle aussi la recombinaison des paires de polarons.

La communauté scientifique démontre actuellement un intérêt vigoureux envers les méthodes de spectroscopie électronique bidimensionnelles. Ces techniques largement utilisées par le groupe de G. Scholes [195] permettent de sonder la dynamique de cohérence entre les états électroniques dans les polymères conjugués ainsi que d'autres systèmes biologiques. Ce type d'expérience à multi impulsions qui a entre autres été utilisé pour étudier la dynamique du transport cohérent des excitations intramoléculaires dans le Poly(phenyleve vinylene) [85] (PPV) serait complémentaire à nos travaux du chapitre 3. Notamment, elles nous permettraient de déterminer la dynamique du transport cohérent des excitations le long des chaînes de polymère ainsi que le long de l'axe de l'agrégat. Cette dynamique devrait être anisotrope et dépendre du poids moléculaire avec la même tendance que nous observons.



## BIBLIOGRAPHIE

- [1] Alan J. HEEGER : Semiconducting and metallic polymers : The fourth generation of polymeric materials (nobel lecture)13. *Angewandte Chemie International Edition*, 40(14):2591–2611, 2001.
- [2] R H FRIEND, R W GYMER, A B HOLMES, J H BURROUGHES, R N MARKS, C TALIANI, D D C BRADLEY, M Lo, W R SALANECK, D A Dos SANTOS et J L BRE : Electroluminescence in conjugated polymers. pages 121–128, 1999.
- [3] Qibing PEI, Gang YU, Chi ZHANG, Yang YANG et Alan J. HEEGER : Polymer light-emitting electrochemical cells. *Science*, 269(5227):1086–1088, 1995.
- [4] Fumitomo HIDE, María A. DÍAZ-GARCÍA, Benjamin J. SCHWARTZ, Mats R. ANDERSSON, Qibing PEI et Alan J. HEEGER : Semiconducting polymers : A new class of solid-state laser materials. *Science*, 273(5283):1833–1836, 1996.
- [5] N. TESSLER, G. J. DENTON et R. H. FRIEND : Lasing from conjugated-polymer microcavities. *Nature*, 382(6593):695–697, août 1996.
- [6] Christopher R. MCNEILL et Neil C. GREENHAM : Conjugated-polymer blends for optoelectronics. *Advanced Materials*, 21(38-39):3840–3850, 2009.
- [7] H SIRRINGHAUS, P J BROWN, R H FRIEND, M M NIELSEN, K BECHGAARD, B M W LANGEVELD-VOSS, A J H SPIERING, R A J JANSSEN, E W MEIJER, P HERWIG et D M de LEEUW : Two-dimensional charge transport in self-organized, high-mobility conjugated polymers. *Nature*, 401(6754):685–688, Jan 1999.
- [8] Ananth DODABALAPUR : Organic and polymer transistors for electronics. *Materials Today*, 9(4):24 – 30, 2006.

- [9] G. YU, J. GAO, J. C. HUMMELEN, F. WUDL et A. J. HEEGER : Polymer photovoltaic cells : Enhanced efficiencies via a network of internal donor-acceptor heterojunctions. *Science*, 270(5243):1789–1791, 1995.
- [10] R. Alex MARSH, Justin M. HODGKISS et Richard H. FRIEND : Direct measurement of electric field-assisted charge separation in polymer :fullerene photovoltaic diodes. *Advanced Materials*, 22(33):3672–3676, 2010.
- [11] Sachetan M. Tuladhar Stelios A. Choulis Jenny Nelson James R. Durrant Donal D. C. Bradley Mark Giles Iain McCulloch Chang-Sik Ha YOUNG-KYOO KIM, Steffan Cook : A strong regioregularity effect in self-organizing conjugated polymer films and high-efficiency polythiophene :fullerene solar cells, 2006.
- [12] NREL : Best research cell efficiencies, 2013.
- [13] R MCCULLOUGH, S TRISTRAM-NAGLE, S WILLIAMS, R D LOWE et M JAYARMAN : Self-orienting head-to-tail poly (3-alkylthiophenes) : new insights on structure-property relationship in conducting polymers. *J. Am. Chem. Soc.*, 115(2):4910–4911, Jan 1993.
- [14] Tian-An CHEN, Xiaoming WU et Reuben D. RIEKE : Regiocontrolled synthesis of poly(3-alkylthiophenes) mediated by rieke zinc : Their characterization and solid-state properties. *Journal of the American Chemical Society*, 117(1):233–244, 1995.
- [15] J. CORNIL, D. BELJONNE, J.-P. CALBERT et J.-L. BRÉDAS : Interchain interactions in organic  $\pi$ -conjugated materials : Impact on electronic structure, optical response, and charge transport. *Advanced Materials*, 13(14):1053–1067, 2001.

- [16] Christina SCHARSICH, Ruth H. LOHWASSER, Michael SOMMER, Udom ASA-WAPIROM, Ullrich SCHERF, Mukundan THELAKKAT, Dieter NEHER et Anna KOHLER : Control of aggregate formation in poly(3-hexylthiophene) by solvent, molecular weight, and synthetic method. *Journal of Polymer Science Part B : Polymer Physics*, 50(6):442–453, 2012.
- [17] M. BRINKMANN et P. RANNOU : Effect of molecular weight on the structure and morphology of oriented thin films of regioregular poly(3-hexylthiophene) grown by directional epitaxial solidification. *Advanced Functional Materials*, 17(1):101–108, 2007.
- [18] Obadiah G. REID, Jennifer A. Nekuda MALIK, Gianluca LATINI, Smita DAYAL, Nikos KOPIDAKIS, Carlos SILVA, Natalie STINGELIN et Garry RUMBLES : The influence of solid-state microstructure on the origin and yield of long-lived photogenerated charge in neat semiconducting polymers. *Journal of Polymer Science Part B : Polymer Physics*, 50(1):27–37, 2012.
- [19] Felix Peter Vinzenz KOCH, Jonathan RIVNAY, Sam FOSTER, Christian MÜLLER, Jonathan M. DOWNING, Ester BUCHACA-DOMINGO, Paul WESTACOTT, Liyang YU, Mingjian YUAN, Mohammed BAKLAR, Zhuping FEI, Christine LUSCOMBE, Martyn A. McLACHLAN, Martin HEENEY, Garry RUMBLES, Carlos SILVA, Alberto SALLEO, Jenny NELSON, Paul SMITH et Natalie STINGELIN : The impact of molecular weight on microstructure and charge transport in semicrystalline polymer semiconductor poly(3-hexylthiophene), a model study. *Progress in Polymer Science*, (0):–, 2013.
- [20] Elena MENA-OSTERITZ, Alexander MEYER, Bea M. W. LANGEVELD-VOSS, Rene A. J. JANSSEN, E. W. MEIJER et Peter BADUERLE : Two-dimensional crystals of poly(3-alkyl- thiophene)s : Direct visualization of polymer folds in

- submolecular resolution. *Angewandte Chemie International Edition*, 39(15): 2679–2684, 2000.
- [21] A. ZEN, J. PFLAUM, S. HIRSCHMANN, W. ZHUANG, F. JAISER, U. ASAWA-PIROM, J. P. RABE, U. SCHERF et D. NEHER : Effect of molecular weight and annealing of poly(3-hexylthiophene)s on the performance of organic field-effect transistors. *Advanced Functional Materials*, 14(8):757–764, 2004.
- [22] Veaceslav COROPCEANU, Jérôme CORNIL, Demetrio A. da SILVA FILHO, Yoann OLIVIER, Robert SILBEY et Jean-Luc BRÉDAS : Charge transport in organic semiconductors. *Chemical Reviews*, 107(4):926–952, 2007.
- [23] Henning SIRRINGHAUS, Nir TESSLER et Richard H. FRIEND : Integrated optoelectronic devices based on conjugated polymers. *Science*, 280(5370): 1741–1744, 1998.
- [24] Minh Trung DANG, Lionel HIRSCH et Guillaume WANTZ : P3ht :pcbm, best seller in polymer photovoltaic research. *Advanced Materials*, 23(31):3597–3602, 2011.
- [25] Su-Hwan LEE, Ji-Heon KIM, Tae-Hun SHIM et Jea-Gun PARK : Effect of interface thickness on power conversion efficiency of polymer photovoltaic cells. *Electronic Materials Letters*, 5(1):47–50, 2009.
- [26] Su-Hwan LEE, Dal-Ho KIM, Ji-Heon KIM, Gon-Sub LEE et Jea-Gun PARK : Effect of metal-reflection and surface-roughness properties on power-conversion efficiency for polymer photovoltaic cells. *The Journal of Physical Chemistry C*, 113(52):21915–21920, 2009.
- [27] R.J. KLINE, M.D. MCGEHEE, E.N. KADNIKOVA, J. LIU et J.M.J. FRÉCHET : Controlling the field-effect mobility of regioregular polythiophene by changing the molecular weight. *Advanced Materials*, 15(18):1519–1522, 2003.

- [28] R. Joseph KLINE, Michael D. MCGEHEE, Ekaterina N. KADNIKOVA, Jinsong LIU, Jean M. J. FRÉCHET et Michael F. TONEY : Dependence of regioregular poly(3-hexylthiophene) film morphology and field-effect mobility on molecular weight. *Macromolecules*, 38(8):3312–3319, 2005.
- [29] Chiatzun GOH, R. Joseph KLINE, Michael D. MCGEHEE, Ekaterina N. KADNIKOVA et Jean M. J. FRÉCHET : Molecular-weight-dependent mobilities in regioregular poly(3-hexyl-thiophene) diodes. *Applied Physics Letters*, 86(12):122110, 2005.
- [30] Rui ZHANG, Bo LI, Mihaela C. IOVU, Malika JEFFRIES-EL, Geneviève SAUVÉ, Jessica COOPER, Shijun JIA, Stephanie TRISTRAM-NAGLE, Detlef M. SMILGIES, David N. LAMBETH, Richard D. McCULLOUGH et Tomasz KOWALEWSKI : Nanostructure dependence of field-effect mobility in regioregular poly(3-hexylthiophene) thin film field effect transistors. *Journal of the American Chemical Society*, 128(11):3480–3481, 2006.
- [31] Jui-Fen CHANG, Jenny CLARK, Ni ZHAO, Henning SIRRINGHAUS, Dag W. BREIBY, Jens W. ANDREASEN, Martin M. NIELSEN, Mark GILES, Martin HEENEY et Iain MCCULLOCH : Molecular-weight dependence of interchain polaron delocalization and exciton bandwidth in high-mobility conjugated polymers. *Phys. Rev. B*, 74:115318, Sep 2006.
- [32] Amy M. BALLANTYNE, Lichun CHEN, Justin DANE, Thomas HAMMANT, Felix M. BRAUN, Martin HEENEY, Warren DUFFY, Iain MCCULLOCH, Donal D. C. BRADLEY et Jenny NELSON : The effect of poly(3-hexylthiophene) molecular weight on charge transport and the performance of polymer :fullerene solar cells. *Advanced Functional Materials*, 18(16):2373–2380, 2008.
- [33] E HENDRY, J M SCHINS, L P CANDEIAS, L D A SIEBBELES et M BONN :

- Efficiency of exciton and charge carrier photogeneration in a semiconducting polymer. *Phys. Rev. Lett.*, 92(19):196601, Jan 2004.
- [34] T DRORI, J HOLT et Z. V VARDENY : Optical studies of the charge transfer complex in polythiophene/fullerene blends for organic photovoltaic applications. *Phys. Rev. B*, 82(7):075207, Jan 2010.
- [35] Jiamo GUO, Hideo OHKITA, Hiroaki BENTEN et Shinzaburo ITO : Charge generation and recombination dynamics in poly(3-hexylthiophene)/fullerene blend films with different regioregularities and morphologies. *Journal of the American Chemical Society*, 132(17):6154–6164, 2010.
- [36] William BARFORD : *Electronic and Optical Properties of Conjugated Polymers*. Clarendon Press, Oxford, 2005.
- [37] J. David GRIFFITHS : *Introduction to quantum mechanics*. Pearson Prentice Hall, 2005.
- [38] M. POPE et C. E. SWENBERG : *Electronic Processes in Organic Crystals and Polymers*. Oxford University Press, 2nd édition, 1999.
- [39] Jean-Luc BRÉDAS, David BELJONNE, Veaceslav COROPCEANU et Jérôme CORNIL : Charge-transfer and energy-transfer processes in  $\pi$ -conjugated oligomers and polymers : A molecular picture. *Chemical Reviews*, 104(11):4971–5004, 2004. PMID : 15535639.
- [40] C. GADERMAIER, G. CERULLO, G. SANSONE, G. LEISING, U. SCHERF et G. LANZANI : Time-resolved charge carrier generation from higher lying excited states in conjugated polymers. *Phys. Rev. Lett.*, 89:117402, Aug 2002.
- [41] E. S. MEDVEDEV et V. I. OSHEROV : *Radiationless Transitions in Polyatomic Molecules*, volume 57. Springer-Verlag, 1995.

- [42] J. Nicholas TURRO : *Modern Molecular Photochemistry*. University Science Books, 1991.
- [43] A. KOHLER et D. BELJONNE : The singlet-triplet exchange energy in conjugated polymers. *Advanced Functional Materials*, 14(1):11–18, 2004.
- [44] Steffan COOK, Han LIYUAN, Akihiro FURUBE et Ryuzi KATOH : Singlet annihilation in films of regioregular poly(3-hexylthiophene) : Estimates for singlet diffusion lengths and the correlation between singlet annihilation rates and spectral relaxation. *J Phys Chem C*, 114(24):10962–10968, Jan 2010.
- [45] Jiamo GUO, Hideo OHKITA, Hiroaki BENTEN et Shinzaburo ITO : Near-infrared femtosecond transient absorption spectroscopy of ultrafast polaron and triplet exciton formation in polythiophene films with different regioregularities. *Journal of the American Chemical Society*, 131(46):16869–16880, 2009. PMID : 19886624.
- [46] Alan J. Heeger JEAN-LUC BRÉDAS, Jérôme Cornil : The exciton binding energy in luminescent conjugated polymers, 1996.
- [47] Tracey M. CLARKE et James R. DURRANT : Charge photogeneration in organic solar cells. *Chem. Rev.*, 110(11):6736–6767, 2010.
- [48] Brian A. GREGG et Mark C. HANNA : Comparing organic to inorganic photovoltaic cells : Theory, experiment, and simulation. *Journal of Applied Physics*, 93(6), 2003.
- [49] H. YAMAGATA et F. C. SPANO : Vibronic coupling in quantum wires : Applications to polydiacetylene. *The Journal of Chemical Physics*, 135(5):–, 2011.
- [50] Frank C. SPANO et Carlos SILVA : H- and j-aggregate behavior in polymeric semiconductors. *Annual Review of Physical Chemistry*, 65(1), 2014.

- [51] M. Ashraf El-Bayoumi M. KASHA, H. R. Rawls : The exciton model in molecular spectroscopy, 1965.
- [52] R. ÖSTERBACKA, C. P. AN, X. M. JIANG et Z. V. VARDENY : Two-dimensional electronic excitations in self-assembled conjugated polymer nanocrystals. *Science*, 287(5454):839–842, 2000.
- [53] J. CORNIL, D. A. dos SANTOS, X. CRISPIN, R. SILBEY et J. L. BRÉDAS : Influence of interchain interactions on the absorption and luminescence of conjugated oligomers and polymers : A quantum-chemical characterization. *Journal of the American Chemical Society*, 120(6):1289–1299, 1998.
- [54] Michael J. MCINTIRE, Eric S. MANAS et Frank C. SPANO : Spontaneous emission and absorption in model aggregates of  $\pi$ -conjugated oligomers. *The Journal of Chemical Physics*, 107(19), 1997.
- [55] Z. G. SOOS, G. W. HAYDEN, P. C. M. McWILLIAMS et S. ETEMAD : Excitation shifts of parallel conjugated polymers due to  $\pi$ -Relectron dispersion forces. *The Journal of Chemical Physics*, 93(10), 1990.
- [56] Frank C SPANO : The spectral signatures of frenkel polarons in h- and j-aggregates, Jan 2010.
- [57] William BARFORD : Exciton transfer integrals between polymer chains. *The Journal of Chemical Physics*, 126(13), 2007.
- [58] Muhammet E. KOSE : Evaluation of excitonic coupling and charge transport integrals in p3ht nanocrystal. *The Journal of Physical Chemistry C*, 115(26): 13076–13082, 2011.
- [59] H. YAMAGATA et F. C. SPANO : Interplay between intrachain and interchain interactions in semiconducting polymer assemblies : The hj-aggregate model. *The Journal of Chemical Physics*, 136(18):184901, 2012.

- [60] Frank C SPANO, Jenny CLARK, Carlos SILVA et Richard H FRIEND : Determining exciton coherence from the photoluminescence spectral line shape in poly(3-hexylthiophene) thin films. *J Chem Phys*, 130(7):074904, Jan 2009.
- [61] Michael R. PHILPOTT : Theory of the Coupling of Electronic and Vibrational Excitations in Molecular Crystals and Helical Polymers. *The Journal of Chemical Physics*, 55(5):2039–2054, 1971.
- [62] Jenny CLARK, Carlos SILVA, Richard H. FRIEND et Frank C. SPANO : Role of intermolecular coupling in the photophysics of disordered organic semiconductors : Aggregate emission in regioregular polythiophene. *Phys. Rev. Lett.*, 98:206406, May 2007.
- [63] William BARFORD : Excitons in conjugated polymers : A tale of two particles. *The Journal of Physical Chemistry A*, 117(13):2665–2671, 2013.
- [64] Francis PAQUIN, Hajime YAMAGATA, Nicholas J. HESTAND, Maciej SAKOWICZ, Nicolas BÉRUBÉ, Michel CÔTÉ, Luke X. REYNOLDS, Saif A. HAQUE, Natalie STINGELIN, Frank C. SPANO et Carlos SILVA : Two-dimensional spatial coherence of excitons in semicrystalline polymeric semiconductors : The effect of molecular weight. *Phys. Rev. B*, submitted, 2013.
- [65] William BARFORD, David G LIDZEY, Dmitry V MAKHOV et Anthony J. H MEIJER : Exciton localization in disordered poly(3-hexylthiophene). *J Chem Phys*, 133(4):044504, Jan 2010.
- [66] F. C. SPANO : Modeling disorder in polymer aggregates : The optical spectroscopy of regioregular poly(3-hexylthiophene) thin films. *J. Chem. Phys.*, 122(23):234701, Jan 2005.
- [67] Thierry Barisien Roger Grousson-Laurent Legrand Michel Schott Valia Vo-

liotis FRANÇOIS DUBIN, Romain Melet : Macroscopic coherence of a single exciton state in an organic quantum wire, 2005.

- [68] Dylan H. ARIAS, Katherine W. STONE, Sebastiaan M. VLAMING, Brian J. WALKER, Moungi G. BAWENDI, Robert J. SILBEY, Vladimir BULOVIC et Keith A. NELSON : Thermally-limited exciton delocalization in superradiant molecular aggregates. *The Journal of Physical Chemistry B*, 117(16):4553–4559, 2013.
- [69] T. KOBAYASHI : *J-aggregates*. World Scientific, Singapore, 1996.
- [70] Edwards T. NILES, John D. ROEHLING, Hajime YAMAGATA, Adam J. WISE, Frank C. SPANO, Adam J. MOULÉ et John K. GREY : J-aggregate behavior in poly-3-hexylthiophene nanofibers. *The Journal of Physical Chemistry Letters*, 3(2):259–263, 2012.
- [71] Christoph HELLMANN, Francis PAQUIN, Neil D. TREAT, Annalisa BRUNO, Luke X. REYNOLDS, Saif A. HAQUE, Paul N. STAVRINO, Carlos SILVA et Natalie STINGELIN : Controlling the interaction of light with polymer semiconductors. *Advanced Materials*, 25(35):4906–4911, 2013.
- [72] Patrick PARKINSON, Christian MULLER, Natalie STINGELIN, Michael B. JOHNSTON et Laura M. HERZ : Role of ultrafast torsional relaxation in the emission from polythiophene aggregates. *The Journal of Physical Chemistry Letters*, 1(19):2788–2792, 2010.
- [73] Edwards T. NILES, John D. ROEHLING, Hajime YAMAGATA, Adam J. WISE, Frank C. SPANO, Adam J. MOULĀL' et John K. GREY : J-aggregate behavior in poly-3-hexylthiophene nanofibers. *The Journal of Physical Chemistry Letters*, 3(2):259–263, 2012.

- [74] Anna KOHLER, Sebastian T. HOFFMANN et Heinz BASSLER : An ordered-disorder transition in the conjugated polymer meh-ppv. *Journal of the American Chemical Society*, 134(28):11594–11601, 2012.
- [75] Jenny CLARK, Jui-Fen CHANG, Frank C. SPANO, Richard H. FRIEND et Carlos SILVA : Determining exciton bandwidth and film microstructure in polythiophene films using linear absorption spectroscopy. *Applied Physics Letters*, 94(16):–, 2009.
- [76] Mina BAGHGAR, Joelle LABASTIDE, Felicia BOKEL, Irene DUJOVNE, Aidan MCKENNA, Austin M. BARNES, Emily PENTZER, Todd EMRICK, Ryan HAYWARD et Michael D. BARNES : Probing inter- and intrachain exciton coupling in isolated poly(3-hexylthiophene) nanofibers : Effect of solvation and regioregularity. *The Journal of Physical Chemistry Letters*, 3(12):1674–1679, 2012.
- [77] Peter KOHN, Sven HUETTNER, Hartmut KOMBER, Volodymyr SENKOVS-KYY, Roman TKACHOV, Anton KIRIY, Richard H. FRIEND, Ullrich STEINER, Wilhelm T. S. HUCK, Jens-Uwe SOMMER et Michael SOMMER : On the role of single regiodefects and polydispersity in regioregular poly(3-hexylthiophene) : Defect distribution, synthesis of defect-free chains, and a simple model for the determination of crystallinity. *Journal of the American Chemical Society*, 134(10):4790–4805, 2012.
- [78] Sarah T. TURNER, Patrick PINGEL, Robert STEYRLEUTHNER, Edward J. W. CROSSLAND, Sabine LUDWIGS et Dieter NEHER : Quantitative analysis of bulk heterojunction films using linear absorption spectroscopy and solar cell performance. *Advanced Functional Materials*, 21(24):4640–4652, 2011.
- [79] Martin BRINKMANN : Structure and morphology control in thin films of

- regioregular poly(3-hexylthiophene). *Journal of Polymer Science Part B : Polymer Physics*, 49(17):1218–1233, 2011.
- [80] B. WUNDERLICH : *Macromolecular Physics.*, volume 2.
- [81] R.J. KLINE, M.D. MCGEHEE, E.N. KADNIKOVA, J. LIU et J.M.J. FRÉCHET : Controlling the field-effect mobility of regioregular polythiophene by changing the molecular weight. *Advanced Materials*, 15(18):1519–1522, 2003.
- [82] R. Joseph KLINE, Michael D. MCGEHEE, Ekaterina N. KADNIKOVA, Jinsong LIU, Jean M. J. FRÉCHET et Michael F. TONEY : Dependence of regioregular poly(3-hexylthiophene) film morphology and field-effect mobility on molecular weight. *Macromolecules*, 38(8):3312–3319, 2005.
- [83] Chiatzun GOH, R. Joseph KLINE, Michael D. MCGEHEE, Ekaterina N. KADNIKOVA et Jean M. J. FRÉCHET : Molecular-weight-dependent mobilities in regioregular poly(3-hexyl-thiophene) diodes. *Applied Physics Letters*, 86(12):–, 2005.
- [84] Amy M. BALLANTYNE, Lichun CHEN, Justin DANE, Thomas HAMMANT, Felix M. BRAUN, Martin HEENEY, Warren DUFFY, Iain MCCULLOCH, Donal D. C. BRADLEY et Jenny NELSON : The effect of poly(3-hexylthiophene) molecular weight on charge transport and the performance of polymer :fullerene solar cells. *Advanced Functional Materials*, 18(16):2373–2380, 2008.
- [85] Elisabetta COLLINI et Gregory D. SCHOLES : Coherent intrachain energy migration in a conjugated polymer at room temperature. *Science*, 323(5912): 369–373, 2009.
- [86] Cathal SMYTH, Francesca FASSIOLI et Gregory D. SCHOLES : Measures and implications of electronic coherence in photosynthetic light-harvesting.

*Philosophical Transactions of the Royal Society A : Mathematical, Physical and Engineering Sciences*, 370(1972):3728–3749, 2012.

- [87] Oliver KUHN et Villy SUNDSTROM : Pump-probe spectroscopy of dissipative energy transfer dynamics in photosynthetic antenna complexes : A density matrix approach. *The Journal of Chemical Physics*, 107(11), 1997.
- [88] T. MEIER, V. CHERNYAK et S. MUKAMEL : Multiple exciton coherence sizes in photosynthetic antenna complexes viewed by pumpâŠprobe spectroscopy. *The Journal of Physical Chemistry B*, 101(37):7332–7342, 1997.
- [89] Frank C. SPANO : Absorption in regio-regular poly(3-hexyl)thiophene thin films : Fermi resonances, interband coupling and disorder. *Chem. Phys.*, 325(1):22 – 35, 2006.
- [90] A. HORVATH, G. WEISER, C. LAPERSONNE-MEYER, M. SCHOTT et S. SPAGNOLI : Wannier excitons and fritz-keldysh effect of polydiacetylene chains diluted in their single crystal monomer matrix. *Phys. Rev. B*, 53:13507–13514, May 1996.
- [91] R. LÉCUILLER, J. BERRÉHAR, J. D. GANIÈRE, C. LAPERSONNE-MEYER, P. LAVALLARD et M. SCHOTT : Fluorescence yield and lifetime of isolated polydiacetylene chains : Evidence for a one-dimensional exciton band in a conjugated polymer. *Phys. Rev. B*, 66:125205, Sep 2002.
- [92] M. SCHOTT : *Photophysics of Molecular Materials : from Single Molecules to Single Crystals*, edited by G. Lanzani. Wiley-VCH, Weinheim, 2005.
- [93] S. WESTENHOFF, A. ABRUSCI, W.J. FEAST, O. HENZE, A.F.M. KILBINGER, A.P.H.J. SCHENNING et C. SILVA : Supramolecular electronic coupling in chiral oligothiophene nanostructures. *Advanced Materials*, 18(10):1281–1285, 2006.

- [94] Johannes GIERSCHNER, Ya-Shih HUANG, Bernard VAN AVERBEKE, Jérôme CORNIL, Richard H. FRIEND et David BELJONNE : Excitonic versus electronic couplings in molecular assemblies : The importance of non-nearest neighbor interactions. *The Journal of Chemical Physics*, 130(4), 2009.
- [95] Eric S. MANAS et Frank C. SPANO : Absorption and spontaneous emission in aggregates of conjugated polymers. *The Journal of Chemical Physics*, 109(18), 1998.
- [96] Chris GROVES, Obadiah G. REID et David S. GINGER : Heterogeneity in polymer solar cells : Local morphology and performance in organic photovoltaics studied with scanning probe microscopy. *Accounts of Chemical Research*, 43(5):612–620, 2010. PMID : 20143815.
- [97] Katsuichi KANEMOTO, Tatsushi SUDO, Ichiro AKAI, Hideki HASHIMOTO, Tsutomu KARASAWA, Yoshio ASO et Tetsuo OTSUBO : Intrachain photoluminescence properties of conjugated polymers as revealed by long oligothiophenes and polythiophenes diluted in an inactive solid matrix. *Phys. Rev. B*, 73:235203, Jun 2006.
- [98] R. CHANG, J.H. HSU, W.S. FANN, K.K. LIANG, C.H. CHANG, M. HAYASHI, J. YU, S.H. LIN, E.C. CHANG, K.R. CHUANG et S.A. CHEN : Experimental and theoretical investigations of absorption and emission spectra of the light-emitting polymer meh-ppv in solution. *Chemical Physics Letters*, 317(12):142 – 152, 2000.
- [99] R. CHANG, J.H. HSU, W.S. FANN, K.K. LIANG, C.H. CHANG, M. HAYASHI, J. YU, S.H. LIN, E.C. CHANG, K.R. CHUANG et S.A. CHEN : Experimental and theoretical investigations of absorption and emission spectra of the light-emitting polymer meh-ppv in solution. *Chemical Physics Letters*, 317(12):142 – 152, 2000.

- [100] J. CORNIL, D. BELJONNE, C.M. HELLER, I.H. CAMPBELL, B.K. LAURICH, D.L. SMITH, D.D.C. BRADLEY, K. MULLEN et J.L. BRÉDAS : Photoluminescence spectra of oligo-paraphenylenevinylenes : a joint theoretical and experimental characterization. *Chemical Physics Letters*, 278(13):139 – 145, 1997.
- [101] Natalie BANERJI, Sarah COWAN, Eric VAUTHEY et Alan J. HEEGER : Ultra-fast relaxation of the poly(3-hexylthiophene) emission spectrum. *The Journal of Physical Chemistry C*, 115(19):9726–9739, 2011.
- [102] Erik BUSBY, Elizabeth C. CARROLL, Erin M. CHINN, Lilian CHANG, Adam J. MOULÉ et Delmar S. LARSEN : Excited-state self-trapping and ground-state relaxation dynamics in poly(3-hexylthiophene) resolved with broadband pump-dump-probe spectroscopy. *The Journal of Physical Chemistry Letters*, 2(21):2764–2769, 2011.
- [103] S. TRETIAK, A. SAXENA, R. L. MARTIN et A. R. BISHOP : Conformational dynamics of photoexcited conjugated molecules. *Phys. Rev. Lett.*, 89:097402, Aug 2002.
- [104] E.W. KNAPP : Lineshapes of molecular aggregates, exchange narrowing and intersite correlation. *Chemical Physics*, 85(1):73 – 82, 1984.
- [105] Frank C. SPANO, Stefan C. J. MESKERS, Emanuelle HENNEBICQ et David BELJONNE : Probing excitation delocalization in supramolecular chiral stacks by means of circularly polarized light : Experiment and modeling. *Journal of the American Chemical Society*, 129(22):7044–7054, 2007. PMID : 17497856.
- [106] M. DAHLBOM, T. PULLERITS, S. MUKAMEL et V. SUNDSTRÖM : Exciton delocalization in the b850 light-harvesting complex : Comparison of different measures. *The Journal of Physical Chemistry B*, 105(23):5515–5524, 2001.

- [107] T. MEIER, Y. ZHAO, V. CHERNYAK et S. MUKAMEL : Polarons, localization, and excitonic coherence in superradiance of biological antenna complexes. *The Journal of Chemical Physics*, 107(10), 1997.
- [108] R J KLINE, M D McGEHEE, E N KADNIKOVA, J S LIU, J M J FRECHET et M F TONEY : Dependence of regioregular poly(3-hexylthiophene) film morphology and field-effect mobility on molecular weight. *Macromolecules*, 38(8):3312–3319, Jan 2005.
- [109] Loren G. KAAKE, Jacek J. JASIENIAK, Ronald C. BAKUS, Gregory C. WELCH, Daniel MOSES, Guillermo C. BAZAN et Alan J. HEEGER : Photoinduced charge generation in a molecular bulk heterojunction material. *Journal of the American Chemical Society*, 134(48):19828–19838, 2012.
- [110] Wanli MA, Jin Young KIM, Kwanghee LEE et Alan J. HEEGER : Effect of the molecular weight of poly(3-hexylthiophene) on the morphology and performance of polymer bulk heterojunction solar cells. *Macromolecular Rapid Communications*, 28(17):1776–1780, 2007.
- [111] Yongye LIANG, Zheng XU, Jiangbin XIA, Szu-Ting TSAI, Yue WU, Gang LI, Claire RAY et Luping YU : For the bright future : Bulk heterojunction polymer solar cells with power conversion efficiency of 7.4 *Advanced Materials*, 22(20):E135–E138, 2010.
- [112] W. MA, C. YANG, X. GONG, K. LEE et A. J. HEEGER : Thermally stable, efficient polymer solar cells with nanoscale control of the interpenetrating network morphology. *Advanced Functional Materials*, 15(10):1617–1622, 2005.
- [113] Wei ZHANG, Rong HU, Dan LI, Ming-Ming HUO, Xi-Cheng AI et Jian-Ping ZHANG : Primary dynamics of exciton and charge photogeneration in solvent vapor annealed p3ht/pcbm films. *The Journal of Physical Chemistry C*, 116(6):4298–4310, 2012.

- [114] Dirk VELDMAN, Stefan C. J. MESKERS et René A. J. JANSSEN : The energy of charge-transfer states in electron donor-acceptor blends : Insight into the energy losses in organic solar cells. *Advanced Functional Materials*, 19(12): 1939–1948, 2009.
- [115] Jean-Luc BRÉDAS, Jérôme CORNIL et Alan J. HEEGER : The exciton binding energy in luminescent conjugated polymers. *Advanced Materials*, 8(5):447–452, 1996.
- [116] Paul E. SHAW, Arvydas RUSECKAS et Ifor D. W. SAMUEL : Exciton diffusion measurements in poly(3-hexylthiophene). *Advanced Materials*, 20(18):3516–3520, 2008.
- [117] Andrew T. HEALY, Bryan W. BOUDOURIS, C. Daniel FRISBIE, Marc A. HILLMYER et David A. BLANK : Intramolecular exciton diffusion in poly(3-hexylthiophene). *The Journal of Physical Chemistry Letters*, 4(20):3445–3449, 2013.
- [118] Hideo OHKITA, Junya KOSAKA, Jiamo GUO, Hiroaki BENTEN et Shinzaburo ITO : Charge generation dynamics in polymer/polymer solar cells studied by transient absorption spectroscopy. *Journal of Photonics for Energy*, 1(1): 011118–011118–12, 2011.
- [119] Giulia GRANCINI, Dario POLLÌ, Daniele FAZZI, Juan CABANILLAS-GONZALEZ, Giulio CERULLO et Guglielmo LANZANI : Transient absorption imaging of p3ht :pcbm photovoltaic blend : Evidence for interfacial charge transfer state. *The Journal of Physical Chemistry Letters*, 2(9):1099–1105, 2011.
- [120] Katsuichi KANEMOTO, Motoaki YASUI, Daisuke KOSUMI, Akihiko OGATA, Mitsuru SUGISAKI, Tsutomu KARASAWA, Ichiro AKAI et Hideki HASHI-

- MOTO : Morphology-dependent carrier and exciton generations in regioregular poly(3-hexylthiophene) polymer diodes as revealed by bleaching spectroscopy. *Phys. Rev. Lett.*, 103(18):187402, Jan 2009.
- [121] Gabriele D'AVINO, Sébastien MOTHY, Luca MUCCIOLI, Claudio ZANNONI, Linjun WANG, Jérôme CORNIL, David BELJONNE et Frédéric CASTET : Energetics of electron-hole separation at p3ht/pcbm heterojunctions. *The Journal of Physical Chemistry C*, 117(25):12981–12990, 2013.
- [122] Frank C SPANO : Excitons in conjugated oligomer aggregates, films, and crystals. *Annu. Rev. Phys. Chem.*, 57:217–243, Jan 2006.
- [123] Xin AI, Matthew C BEARD, Kelly P KNUTSEN, Sean E SHAHEEN, Garry RUMBLES et Randy J ELLINGSON : Photoinduced charge carrier generation in a poly(3-hexylthiophene) and methanofullerene bulk heterojunction investigated by time-resolved terahertz spectroscopy. *J. Phys. Chem. B*, 110(50):25462–25471, Jan 2006.
- [124] C SHENG, M TONG, S SINGH et Z V VARDENY : Experimental determination of the charge/neutral branching ratio eta in the photoexcitation of pi-conjugated polymers by broadband ultrafast spectroscopy. *Phys. Rev. B*, 75(8):085206, Feb 2007.
- [125] Paul D CUNNINGHAM et L. Michael HAYDEN : Carrier dynamics resulting from above and below gap excitation of P3HT and P3HT/PCBM investigated by optical-pump terahertz-probe spectroscopy. *J. Phys. Chem. C*, 112(21):7928–7935, Jan 2008.
- [126] Jorge PIRIS, Tieneke E DYKSTRA, Artem A BAKULIN, Paul H. M van LOOSDRECHT, Walter KNULST, M. Tuan TRINH, Juleon M SCHINS et Laurens D. A SIEBBELES : Photogeneration and ultrafast dynamics of excitons and

- charges in P3HT/PCBM blends. *J. Phys. Chem. C*, 113(32):14500–14506, Jan 2009.
- [127] Carsten DEIBEL, Daniel MACK, Julien GORENFLOT, Achim SCHOELL, Stefan KRAUSE, Friedrich REINERT, Daniel RAUH et Vladimir DYAKONOV : Energetics of excited states in the conjugated polymer poly(3-hexylthiophene). *Phys. Rev. B*, 81(8):085202, Jan 2010.
- [128] F. C. SPANO : Erratum : Modeling disorder in polymer aggregates : The optical spectroscopy of regioregular poly(3-hexylthiophene) thin films. *J. Chem. Phys.*, 126:159901, 2007.
- [129] Jenny CLARK, Carlos SILVA, Richard H FRIEND et Frank C SPANO : Role of intermolecular coupling in the photophysics of disordered organic semiconductors : Aggregate emission in regioregular polythiophene. *Phys. Rev. Lett.*, 98(20):206406, Jan 2007.
- [130] Jenny CLARK, Jui-Fen CHANG, Frank C SPANO, Richard H FRIEND et Carlos SILVA : Determining exciton bandwidth and film microstructure in polythiophene films using linear absorption spectroscopy. *Appl. Phys. Lett.*, 94(16):163306, Jan 2009.
- [131] M. H CHANG, M. J FRAMPTON, H. L ANDERSON et L. M HERZ : Intermolecular interaction effects on the ultrafast depolarization of the optical emission from conjugated polymers. *Phys. Rev. Lett.*, 98(2):027402, Jan 2007.
- [132] Elisabetta COLLINI et Gregory D SCHOLES : Coherent intrachain energy migration in a conjugated polymer at room temperature. *Science*, 323(5912):369–373, Jan 2009.
- [133] We excite both H aggregates and nonaggregates with similar probability at 2.33 eV, so exciton diffusion would result in a dynamic memory loss of the

ensemble-average transition-dipole-moment orientation. We observe this at 300 K because exciton diffusion is thermally activated, but not at 10K. See D. Beljonne et al., *J. Phys. Chem. B* 109, 10594 (2005) for relevant modeling.

- [134] Patrick PARKINSON, Christian MUELLER, Natalie STINGELIN, Michael B JOHNSTON et Laura M HERZ : Role of ultrafast torsional relaxation in the emission from polythiophene aggregates. *J. Phys. Chem. Lett.*, 1(19):2788–2792, Jan 2010.
- [135] R. KERSTING, U. LEMMER, M. DEUSSEN, H. J. BAKKER, R. F. MAHRT, H. KURZ, V. I. ARKHIPOV, H. BÄSSLER et E. O. GÖBEL : Ultrafast field-induced dissociation of excitons in conjugated polymers. *Phys. Rev. Lett.*, 73(10):1440–1443, Sep 1994.
- [136] B. J. SCHWARTZ : Conjugated polymers as molecular materials : How chain conformation and film morphology influence energy transfer and interchain interactions. *Annu. Rev. Phys. Chem.*, 54:141–172, Jan 2003.
- [137] B SCHWEITZER, V I ARKHIPOV, U SCHERF et H BÄSSLER : Geminate pair recombination in a conjugated polymer. *Chem. Phys. Lett.*, 313(1-2):57–62, Jan 1999.
- [138] A GERHARD et H BASSLER : Delayed fluorescence of a poly (p-phenylenevinylene) derivative : Triplet-triplet annihilation versus geminate pair recombination. *J. Chem. Phys.*, 117(15):7350–7356, Jan 2002.
- [139] C ROTHE et A MONKMAN : Regarding the origin of the delayed fluorescence of conjugated polymers. *J. Chem. Phys.*, 123(24):244904, Jan 2005.
- [140] Colin-N BROSSEAU, Mathieu PERRIN, Carlos SILVA et Richard LEONELLI : Carrier recombination dynamics in  $\text{In}_x\text{Ga}_{1-x}\text{N}/\text{GaN}$  multiple quantum wells. *Phys. Rev. B*, 82(8):085305, Jan 2010.

- [141] G DICKER, M P de HAAS et L D A SIEBBELES : Signature of exciton annihilation in the photoconductance of regioregular poly(3-hexylthiophene). *Phys. Rev. B*, 71(15):155204, Jan 2005.
- [142] Andrew J FERGUSON, Nikos KOPIDAKIS, Sean E SHAHEEN et Garry RUMBLES : Quenching of excitons by holes in poly(3-hexylthiophene) films. *J. Phys. Chem. C*, 112(26):9865–9871, Jan 2008.
- [143] Y. GAO, T. P. MARTIN, A. K. THOMAS et A. K. GREY : Resonance Raman spectroscopic- and photocurrent imaging of polythiophene/fullerene solar cells. *J. Phys. Chem. Lett.*, 1(1):178–182, Jan 2010.
- [144] Semiempirical INDO/SCI excited-state calculations (including 200 molecular orbitals in the active space) have been performed on the basis of snapshot extracted from molecular dynamics simulations of the stack, using a force field parametrized against high-level *ab initio* calculations. Further details will be reported elsewhere.
- [145] Mohammed A. BAKLAR, Felix KOCH, Avinesh KUMAR, Ester Buchaca DOMINGO, Mariano CAMPOY-QUILES, Kirill FELDMAN, Liyang YU, Paul WOBKENBERG, James BALL, Rory M. WILSON, Iain MCCULLOCH, Theo KREOUZIS, Martin HEENEY, Thomas ANTHOPOULOS, Paul SMITH et Natalie STINGLIN : Solid-state processing of organic semiconductors. *Adv. Mater.*, 22(35):3942–3947, 2010.
- [146] Neil D TREAT, Michael A BRADY, Gordon SMITH, Michael F TONEY, Edward J KRAMER, Craig J HAWKER et Michael L CHABINYC : Interdiffusion of PCBM and P3HT Reveals Miscibility in a Photovoltaically Active Blend. *Adv. Energy Mater.*, 1(1):82–89, novembre 2010.
- [147] Brian A. COLLINS, Eliot GANN, Lewis GUIGNARD, Xiaoxi HE, Christopher R

- MCNEILL et Harald ADE : Molecular miscibility of polymer-fullerene blends. *J. Phys. Chem. Lett.*, 1(21):3160–3166, 2010.
- [148] Fiona C JAMIESON, Ester Buchaca DOMINGO, Thomas MCCARTHY-WARD, Martin HEENEY, Natalie STINGELIN et James R DURRANT : Fullerene crystallisation as a key driver of charge separation in polymer/fullerene bulk heterojunction solar cells. *Chem. Sci.*, 3(2):485, 2012.
- [149] Francis PAQUIN, Gianluca LATINI, Maciej SAKOWICZ, Paul-Ludovic KARSENTI, Linjun WANG, David BELJONNE, Natalie STINGELIN et Carlos SILVA : Charge separation in semicrystalline polymeric semiconductors by photoexcitation : Is the mechanism intrinsic or extrinsic ? *Phys. Rev. Lett.*, 106:197401, May 2011.
- [150] Martin BRINKMANN et Patrice RANNOU : Effect of molecular weight on the structure and morphology of oriented thin films of regioregular poly(3-hexylthiophene) grown by directional epitaxial solidification. *Adv. Mater.*, 17(1):101–108, 2007.
- [151] Martin BRINKMANN : Structure and morphology control in thin films of regioregular poly(3-hexylthiophene). *J. Polym. Sci. Part B Polym. Phys.*, 49(17):1218–1233, 2011.
- [152] Felix P.V. KOCH, Jonathan RIVNAY, Sam FOSTER, Christian MÜLLER, Jonathan DOWNING, Ester BUCHACA-DOMINGO, Paul WESTACOTT, Liyang YU, Mingjian YUAN, Mohammed A. BAKLAR, Christine LUSCOMBE, Martyn McLACHLAN, Martin HEENEY, Garry RUMBLES, Carlos SILVA, Alberto SALLEO, Jenny NELSON, Paul SMITH et Natalie STINGELIN : Microstructure development with molecular weight in semicrystalline organic semiconductors and its influence on charge transport. *Prog. Polym. Sci.*, in press, 2013.

- [153] B. WUNDERLICH : *Macromolecular physics, vol. 2 crystal nucleation, growth, annealing.* Academic Press, New York, 1976.
- [154] J. P. JOG : Solid state processing of polymers : A review. *Adv. Polym. Tech.*, 12(3):281–289, 1993.
- [155] Jenny CLARK, Carlos SILVA, Richard H. FRIEND et Frank C. SPANO : Role of intermolecular coupling in the photophysics of disordered organic semiconductors : Aggregate emission in regioregular polythiophene. *Phys. Rev. Lett.*, 98:206406, May 2007.
- [156] Frank C. SPANO, Jenny CLARK, Carlos SILVA et Richard H. FRIEND : Determining exciton coherence from the photoluminescence spectral line shape in poly(3-hexylthiophene) thin films. *J. Chem. Phys.*, 130(7):074904, 2009.
- [157] Obadiah G. REID, Jennifer A. Nekuda MALIK, Gianluca LATINI, Smita DAYAL, Nikos KOPIDAKIS, Carlos SILVA, Natalie STINGELIN et Garry RUMBLES : The influence of solid-state microstructure on the origin and yield of long-lived photogenerated charge in neat semiconducting polymers. *J. Polym. Sci. Part B Polym. Phys.*, 50(1):27–37, 2012.
- [158] M. TACHIYA et Kazuhiko SEKI : Unified explanation of the fluorescence decay and blinking characteristics of semiconductor nanocrystals. *Appl. Phys. Lett.*, 94(8):081104, 2009.
- [159] A. M. HINDELEHT et , R : Paracrystals representing the physical state of matter. *J. Phys. C : Solid State Phys.*, 21:4155–4170, 1988.
- [160] Jonathan RIVNAY, Rodrigo NORIEGA, R. Joseph KLINE, Alberto SALLEO et Michael F. TONEY : Quantitative analysis of lattice disorder and crystallite size in organic semiconductor thin films. *Phys. Rev. B*, 84:045203, Jul 2011.

- [161] B. E. WARREN et B. L. AVERBACH : The effect of cold- $\ddot{\text{R}}$ work distortion on x- $\ddot{\text{R}}$ ay patterns. *Journal of Applied Physics*, 21(6), 1950.
- [162] B. E. WARREN et B. L. AVERBACH : The separation of cold- $\ddot{\text{R}}$ work distortion and particle size broadening in x- $\ddot{\text{R}}$ ay patterns. *Journal of Applied Physics*, 23(4), 1952.
- [163] Rodrigo NORIEGA, Jonathan RIVNAY, Koen VANDEWAL, Felix P.V. KOCH, Natalie STINGELIN, Paul SMITH, Michael F. TONEY et Alberto SALLEO : General relationship between disorder, aggregation, and charge transport in conjugated polymers. *Nat. Mater.*, in press.
- [164] P. F. BARBARA, T. J. MEYER et M. A. RATNER : Contemporary issues in electron transfer research. *J. Phys. Chem.*, 100(31):13148–13168, AUG 1 1996.
- [165] Joelle A. LABASTIDE, Mina BAGHGAR, Irene DUJOVNE, B. Harihara VENKATRAMAN, David C. RAMSDELL, Dhandapani VENKATARAMAN et Michael D. Barnes : Time- and polarization-resolved photoluminescence of individual semicrystalline polythiophene (P3HT) nanoparticles. *The Journal of Physical Chemistry Letters*, 2(17):2089–2093, 2011.
- [166] C.-X. SHENG, M. TONG, S. SINGH et Z. V. VARDENY : Experimental determination of the charge/neutral branching ratio  $\eta$  in the photoexcitation of  $\pi$ -conjugated polymers by broadband ultrafast spectroscopy. *Phys. Rev. B*, 75:085206, Feb 2007.
- [167] Jorge PIRIS, Tieneke E. DYKSTRA, Artem A. BAKULIN, Paul H.M. van LOOSDRECHT, Walter KNULST, M. Tuan TRINH, Juleon M. SCHINS et Laurens D.A. SIEBBELES : Photogeneration and ultrafast dynamics of excitons and charges in P3HT/PCBM blends. *The Journal of Physical Chemistry C*, 113(32):14500–14506, 2009.

- [168] Natalie BANERJI : Sub-picosecond delocalization in the excited state of conjugated homopolymers and donor-acceptor copolymers. *J. Mater. Chem. C*, 1:3052–3066, 2013.
- [169] Natalie BANERJI, Sarah COWAN, Eric VAUTHEY et Alan J. HEEGER : Ultrafast relaxation of the poly(3-hexylthiophene) emission spectrum. *J. Phys. Chem. C*, 115(19):9726–9739, 2011.
- [170] Daniel HERRMANN, Sabrina NIESAR, Christina SCHARSICH, Anna KÖHLER, Martin STUTZMANN et Eberhard RIEDLE : Role of structural order and excess energy on ultrafast free charge generation in hybrid polythiophene/Si photovoltaics probed in real time by near-infrared broadband transient absorption. *J. Am. Chem. Soc.*, 133(45):18220–18233, 2011.
- [171] Loren G. KAAKE, Jacek J. JASIENIAK, Ronald C. BAKUS, Gregory C. WELCH, Daniel MOSES, Guillermo C. BAZAN et Alan J. HEEGER : Photoinduced charge generation in a molecular bulk heterojunction material. *J. Am. Chem. Soc.*, 134(48):19828–19838, 2012.
- [172] Eric R. BITTNER et Carlos SILVA : Noise-induced quantum coherence drives photocarrier generation dynamics at polymeric semiconductor heterojunctions. *Nat. Comm.*, Submitted, 2013.
- [173] Carlo Andrea ROZZI, Sarah Maria FALKE, Nicola SPALLANZANI, Angel RUBIO, Elisa MOLINARI, Daniele BRIDA, Margherita MAIURI, Giulio CERULLO, Heiko SCHRAMM, Jens CHRISTOFFERS et Christoph LIENAU : Quantum coherence controls the charge separation in a prototypical artificial light-harvesting system. *Nat Commun*, 4:1602, 03 2013.
- [174] J. CLARK, J. F. CHANG, F. C. SPANO, R. H. FRIEND et C. SILVA : Determining exciton bandwidth and film microstructure in polythiophene films using linear absorption spectroscopy. *Appl. Phys. Lett.*, 94(16):163306, 2009.

- [175] Patrick PARKINSON, Christian MÜLLER, Natalie STINGELIN, Michael B. JOHNSTON et Laura M. HERZ : Role of ultrafast torsional relaxation in the emission from polythiophene aggregates. *J. Phys. Chem. Lett.*, 1(19):2788–2792, 2010.
- [176] Askat E. JAILAUBEKOV, Adam P. WILLARD, John R. TRITSCH, Wai-Lun CHAN, Na SAI, Raluca GEARBA, Loren G. KAAKE, Kenrick J. WILLIAMS, Kevin LEUNG, Peter J. ROSSKY et X-Y. ZHU : Hot charge-transfer excitons set the time limit for charge separation at donor/acceptor interfaces in organic photovoltaics. *Nat Mater*, 12(1):66–73, 01 2013.
- [177] G. GRANCINI, M. MAIURI, D. FAZZI, A. PETROZZA, H-J. EGELHAAF, D. BRIDA, G. CERULLO et G. LANZANI : Hot exciton dissociation in polymer solar cells. *Nat. Mater.*, 12(1):29–33, 01 2013.
- [178] Elisabetta COLLINI et Gregory D. SCHOLES : Coherent intrachain energy migration in a conjugated polymer at room temperature. *Science*, 323(5912):369–373, 2009.
- [179] L A MAJEWSKI, J W KINGSLEY, C BALOCCO et A M SONG : Influence of processing conditions on the stability of poly(3-hexylthiophene)-based field-effect transistors. *Appl Phys Lett*, 88(22):222108, 2006.
- [180] Two-dimensional electronic excitations in self-assembled conjugated polymer nanocrystals. *Science*, 287(5454):839–842, 2000.
- [181] Carsten DEIBEL, Thomas STROBEL et Vladimir DYAKONOV : Origin of the efficient polaron-pair dissociation in polymer-fullerene blends. *Phys. Rev. Lett.*, 103:036402, Jul 2009.
- [182] F. PAQUIN, J. RIVNAY, A. SALLEO, N. STINGELIN et C. SILVA : Multi-

- phase semicrystalline microstructure drive exciton dissociation in neat plastic semiconductors. *To be submitted to : PNAS*, 2013.
- [183] Joelle A. LABASTIDE, Mina BAGHGOR, Irene DUJOVNE, Yipeng YANG, Anthony D. DINSMORE, Bobby G. SUMPTER, Dhandapani VENKATARAMAN et Michael D. BARNES : Polymer nanoparticle superlattices for organic photovoltaic applications. *The Journal of Physical Chemistry Letters*, 2(24):3085–3091, 2011.
- [184] Steffan COOK, Akihiro FURUBE et Ryuzi KATOH : Analysis of the excited states of regioregular polythiophene p3ht. *Energy Environ. Sci.*, 1:294–299, 2008.
- [185] Sebastian ALBERT-SEIFRIED et Richard H. FRIEND : Measurement of thermal modulation of optical absorption in pump-probe spectroscopy of semiconducting polymers. *Applied Physics Letters*, 98(22):–, 2011.
- [186] Ute B. CAPPEL, Sandra M. FELDT, Jan SCHÖNEBOOM, Anders HAGFELDT et Gerrit BOSCHLOO : The influence of local electric fields on photoinduced absorption in dye-sensitized solar cells. *Journal of the American Chemical Society*, 132(26):9096–9101, 2010.
- [187] O. J. KOROVYANKO, R. ÖSTERBACKA, X. M. JIANG, Z. V. VARDENY et R. A. J. JANSSEN : Photoexcitation dynamics in regioregular and regiorandom polythiophene films. *Phys. Rev. B*, 64:235122, Nov 2001.
- [188] Bing-Rong GAO, Hai-Yu WANG, Hai WANG, Zhi-Yong YANG, Lei WANG, Ying JIANG, Ya-Wei HAO, Qi-Dai CHEN et Hong-Bo SUN : Investigation of polaron pair dynamics in poly(3-hexylthiophene) film by time resolved spectroscopy. *Quantum Electronics, IEEE Journal of*, 48(3):425–432, 2012.

- [189] Ivan G. SCHEBLYKIN, Arkady YARTSEV, Tonu PULLERITS, Vidmantas GULBINAS et Villy SUNDSTROM : Excited state and charge photogeneration dynamics in conjugated polymers. *The Journal of Physical Chemistry B*, 111(23):6303–6321, 2007.
- [190] Hajime YAMAGATA, Chris M. POCHAS et Frank C. SPANO : Designing j- and h-aggregates through wave function overlap engineering : Applications to poly(3-hexylthiophene). *The Journal of Physical Chemistry B*, 116(49):14494–14503, 2012.
- [191] V. I. ARKHIPOV, E. V. EMELIANOVA et H. BÄSSLER : Hot exciton dissociation in a conjugated polymer. *Phys. Rev. Lett.*, 82:1321–1324, Feb 1999.
- [192] S. BARTH, H. BÄSSLER, H. ROST et H. H. HÖRHOLD : Extrinsic and intrinsic dc photoconductivity in a conjugated polymer. *Phys. Rev. B*, 56:3844–3851, Aug 1997.
- [193] Artem A. BAKULIN, Akshay RAO, Vlad G. PAVELYEV, Paul H. M. van LOOSDRECHT, Maxim S. PSHENICHNIKOV, Dorota NIEDZIALEK, Jérôme CORNIL, David BELJONNE et Richard H. FRIEND : The role of driving energy and delocalized states for charge separation in organic semiconductors. *Science*, 335(6074):1340–1344, 2012.
- [194] Tobias Cramer L. Jan Anton Koster Paul W. M. Blom Dago M. de Leeuw KAMAL ASADI, Auke J. Kronemeijer : Polaron hopping mediated by nuclear tunnelling in semiconducting polymers at high carrier density, 2013.
- [195] Gregory D. SCHOLES : Quantum-coherent electronic energy transfer : Did nature think of it first ? *The Journal of Physical Chemistry Letters*, 1(1):2–8, 2010.

- [196] Fabrizia NEGRI et Marek Z. ZGIERSKI : The vibronic structure of the  $s_0 \leftrightarrow s_1$  and  $s_0 \leftrightarrow s_2$  transitions in simple oligomers of thiophene. *J. Chem. Phys.*, 100(4):2571–2587, 1994.
- [197] Erich RUNGE et E. K. U. GROSS : Density-functional theory for time-dependent systems. *Phys. Rev. Lett.*, 52:997–1000, Mar 1984.
- [198] A. RUBIO et M. MARQUES : Time-dependent density-functional theory. *Phys. Chem. Chem. Phys.*, 11:4436–4436, 2009.
- [199] M. J. FRISCH, G. W. TRUCKS, H. B. SCHLEGEL, G. E. SCUSERIA, M. A. ROBB, J. R. CHEESEMAN, G. SCALMANI, V. BARONE, B. MENNUCCI et G. A. PETERSSON : Time-dependent density-functional theory, 2009. Gaussian 09. Gaussian, Inc. : Wallingford, CT.
- [200] Axel D. BECKE : Density functional thermochemistry. iii. the role of exact exchange. *J. Chem. Phys.*, 98:5648–5652, 1993.
- [201] Bryan M. WONG et Timothy H. HSIEH : Optoelectronic and excitonic properties of oligoacenes : Substantial improvements from range-separated time-dependent density functional theory. *J. Chem. Theory Comput.*, 6(12):3704–3712, 2010.

## Annexe I

### Two-dimensional spatial coherence of excitons in semicrystalline polymeric semiconductors : The effect of molecular weight

#### I.1 Determination of $W$ for arbitrary Huang-Rhys parameter obtained from the PL spectrum

The absorption lineshape of P3HT thin films can be understood within the framework of a weakly H-aggregate model. The electronic dispersion of the vibronic molecular levels forms vibronic bands with free-exciton bandwidth  $W = 4J_{\text{inter}}$ . In this paper, we extract the value of  $W$  from the ratio of the absorbance peaks  $A_{0-0}$  and  $A_{0-1}$  with the following analytical expression, assuming a unitary Huang-Rhys factor.

$$\frac{A_{0-0}}{A_{0-1}} \approx \left( \frac{1 - 0.24W/\hbar\omega_0}{1 + 0.073W/\hbar\omega_0} \right)^2. \quad (\text{I.1})$$

By using the previous expression, we assume that the absorbing and emitting species are distinct since the PL spectrum of Fig.2(b) clearly shows that  $\lambda^2$  is not unitary in the low  $M_W$  regime. In fact, the distribution of chromophore configuration is known to be much larger in absorption. After excitation, this distribution narrows down partly due to funneling of the excitation to more ordered domains. Therefore, we can set a higher limit on  $W$  by imposing that  $\lambda^2$  carries the same value in absorption and PL.  $W$  can be found using an expression similar to Eq.I.1 for arbitrary  $\lambda$ . [89]

In Fig.S1, we present  $W$  as a function of the  $M_W$ , using Eq.1 and the full expression from ref. [89]. It is clear that the values of  $W$  are very similar toward high  $M_W$  since  $\lambda^2$  is very close to 1 above  $\sim 50$  kg/mol. As we move toward low  $M_W$ ,  $\lambda^2$  deviates from the value of 1 and can be as high as 1.65 in some films. This

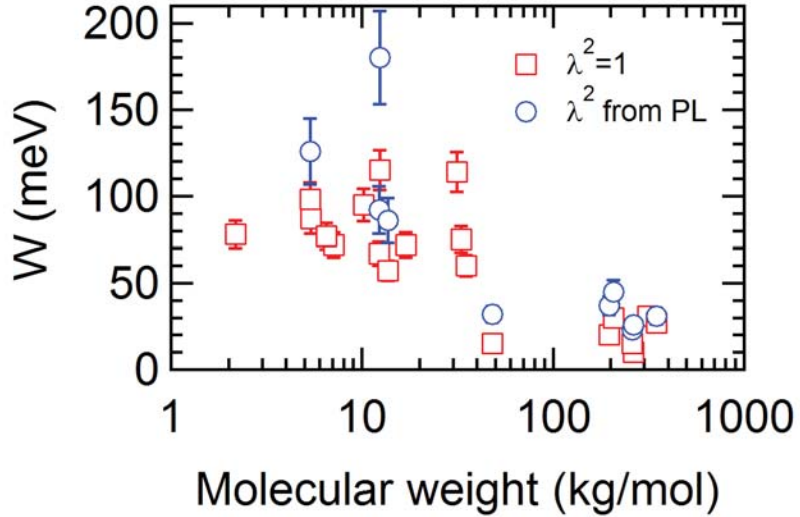


Figure I.1 – Free-exciton bandwidth,  $W$ , extracted from the absorption spectrum using  $\lambda^2 = 1$  (red squares) and arbitrary  $\lambda^2$  obtained from the PL spectra (blue circles) as a function of molecular weight.

causes an apparent increase in  $W$ . Therefore, we can conclude that setting  $\lambda^2=1$  is a good approximation in the high molecular weight regime whereas we expect  $\lambda^2$  to be somewhere between 1 and that measured from the PL for low  $M_W$  films. Nevertheless, the disparity between both methods of calculation is not significant, which explains the use  $\lambda^2=1$  for all films.

## I.2 Huang-Rhys parameter of a single thiophene unit

The Huang-Rhys factor is defined as the ratio of the reorganization energy caused by the displacement of the ions after an excitation, and the zero-point motion energy of the phonon related to this displacement [196]. Therefore, there is one Huang-Rhys factor associated to each phonon. We calculate the reorganization energy via a time-dependant density functional theory optimization [197, 198] as included in the Gaussian 09 package [199]. The first excited state is defined as the root state whose energy is minimized. The reorganization energy is obtained

by subtracting the final and initial configurational energy. A frequency calculation of the Raman spectrum was also made to obtain the vibrational spectrum of the phonons. The 3N-dimensions displacement vector was then expressed as a linear combination of all phonons, in order to calculate the Huang-Rhys factor with :

$$\lambda^2 = \frac{1}{2} \frac{k_i x_i^2}{\hbar \omega_i}, \quad (\text{I.2})$$

where  $x_i$  is the displacement component of a particular phonon  $i$ , and  $k_i$  and  $\omega_i$  are the force constant and the angular frequency of the phonon  $i$  respectively. The isolated thiophene unit is calculated in p-xylene. A modified B3LYP functional using 50 % exact-exchange is used to treat the exchange-correlation energy [200, 201]. It can be justified that a higher percentage of exact-exchange improves the description of the bandgap for the oligothiophene molecules, which should be around 2.3 eV for pentathiophenes [93]. Indeed, upping the percentage from 20 % (in the B3LYP) to 50 % increases the bandgap of tetrathiophenes in chloroform from 2.13 eV to 2.32 eV. We also observe that the bandgap depends only slightly on the exact-exchange percentage, while the Huang-Rhys parameter has a strong dependence on the percentage. It is therefore hard to fit a precise value on the exact-exchange percentage. The value of 50 % is chosen since it has already been used in oligoacenes [93].

The two phonons at 1463 nm and 1512 in Table.I.I arise from C-C oscillations. The sum of their  $\lambda^2$  is 1.81. Two other phonons at 1084 nm and 1152 nm would bring the total Huang-Rhys factor to 2.25, but including them in the total sum is debatable, since the frequency difference is significant. One can also compare those values with the normal B3LYP calculations. The Huang-Rhys factor for the latter would be 1.53 if one does not include the lower frequency phonons, or 1.89 otherwise. Therefore, the choice of 2 for the individual thiophene unit's Huang-Rhys

Tableau I.I – B3LYP-EXX50

Frequency (cm <sup>-1</sup> )	Frequency (eV)	$\lambda^2$
637.4	0.079	2.553
865.9	0.107	0.032
1084.6	0.134	0.019
1152.3	0.143	0.419
1463.0	0.181	0.087
1511.5	0.187	1.726
3317.2	0.411	0.001
3352.3	0.416	0.004

Tableau I.II – B3LYP

Frequency (cm <sup>-1</sup> )	Frequency (eV)	$\lambda^2$
612.6	0.076	2.696
830.0	0.103	0.034
1051.8	0.130	0.001
1107.3	0.137	0.361
1399.2	0.173	0.140
1449.3	0.180	1.392
3209.0	0.398	0.001
3247.1	0.403	0.003

factor is an adequate estimate.

## Annexe II

### Charge separation by photoexcitation in semicrystalline polymeric semiconductors : An intrinsic or extrinsic mechanism ?

#### II.1 Absorption and photoluminescence spectra

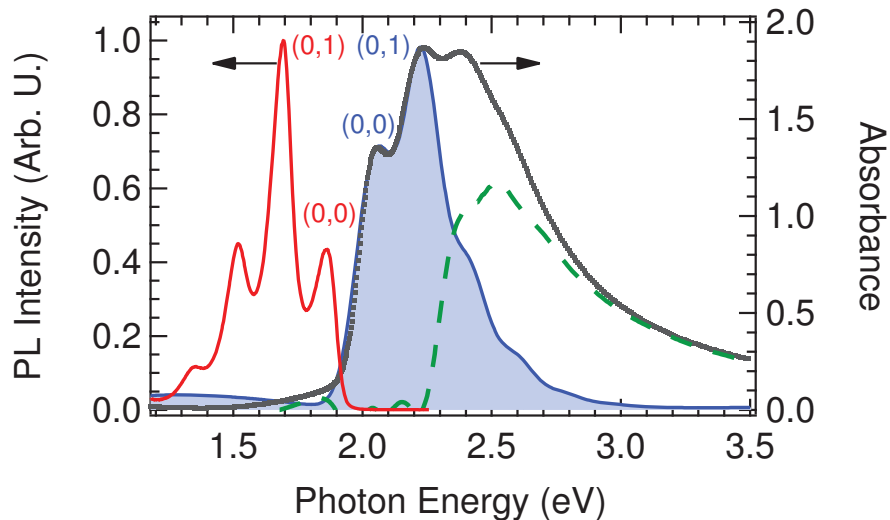


Figure II.1 – Absorption (room-temperature) and PL (10 K) spectra of P3HT. The continuous blue line filled to the baseline displays the absorption spectrum of the H-aggregate obtained via a Franck-Condon model (see ref. 130). The green broken line is the difference between the modelled aggregate spectrum and the measured absorption spectrum.

The absorption and PL spectra of a P3HT film studied in the main article (Merck,  $M_w = 47.8$  kg/mol,  $M_n = 26.2$  kg/mol, polydispersity = 1.83, 150-nm thickness), spun from trichlorobenzene (TCB) solution (6% wt), are displayed in Fig. II.1. We have analyzed the absorption spectrum using a modified Franck-Condon model that takes into account the H-aggregate nature of P3HT lamellar stacks in the weak coupling limit [130]. The blue continuous line filled to the baseline is the fit to this model using the same parameters as in ref. 130, except for

$W = 100 \pm 3$  meV. Following the analysis in ref. 130, we have separated the contribution of non-aggregate regions of the film, shown as a green broken curve. This could be either due to very disordered lamellar stacks in which the electronic coupling is poor, such that absorption resembles that of non-interacting polymer chains, or due to amorphous regions of the film. We estimate a volume fraction  $52 \pm 5\%$  for photophysical aggregates from the modelled contribution of the H-aggregate spectrum. The components of the absorption spectrum due to aggregates and non-aggregates are the two spectral components shown as grey broken lines in Fig. 2(d) of the main article.

## II.2 Time-resolved PL dynamics

### II.2.1 Fluence dependence

We have investigated the fluence dependence of the excitation laser pulse train on the time-resolved and time-integrated PL intensity. Fig. II.2(a) displays the time-resolved PL intensity shown in Fig. 1(a) of the main article, integrated spectrally over the range shown in that figure. Also shown in the figure is a similar measurement carried out with a laser fluence that is a factor of 50 higher. The PL decay dynamics do not depend on fluence over this range. Fig. II.2(b) displays the fluence dependence of the time-integrated PL intensity and the delayed PL intensity over a long temporal gate spanning up to  $500 \mu\text{s}$ . Both PL signals show linear fluence dependence.

### II.2.2 Temperature dependence

In Fig. II.3, we compare the time-resolved PL intensity measured at 10 K with that measured at 293 K. We observe that the initial exponential component decays more rapidly at 293 K, but the slope of the power-law decay component does not show a significant temperature dependence. According to our interpretation in the

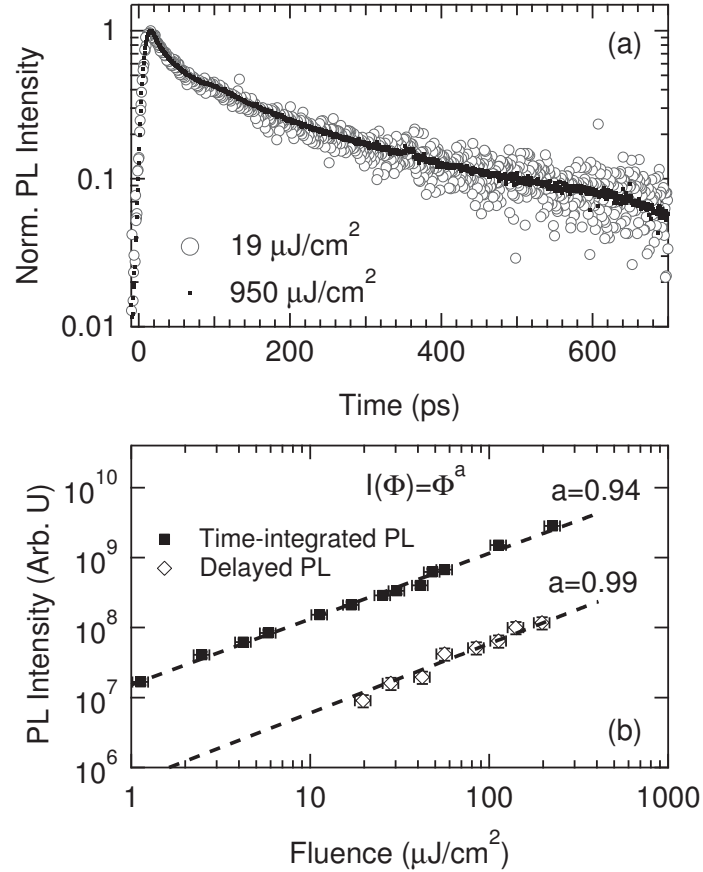


Figure II.2 – (a) Spectrally integrated PL intensity as a function of time following excitation at 2.33 eV, at two different fluences shown in the legend. (b) Fluence dependence of the time-integrated, spectrally-integrated PL intensity, and that of the spectrally-integrated, delayed PL intensity over a temporal gate of 100 ns to 500  $\mu\text{s}$ . All measurements were carried out at 10 K.

main article, this power-law decay is due to recombination of geminate polaron pairs produced on much faster timescales, and the slope of the decay is indicative of the distribution of electron-hole separation compared to the distance dependence of recombination by quantum tunnelling (the parameter  $\mu$  in our model). We invoke the tunnelling mechanism because of the weak temperature dependence of the slow recombination dynamics.

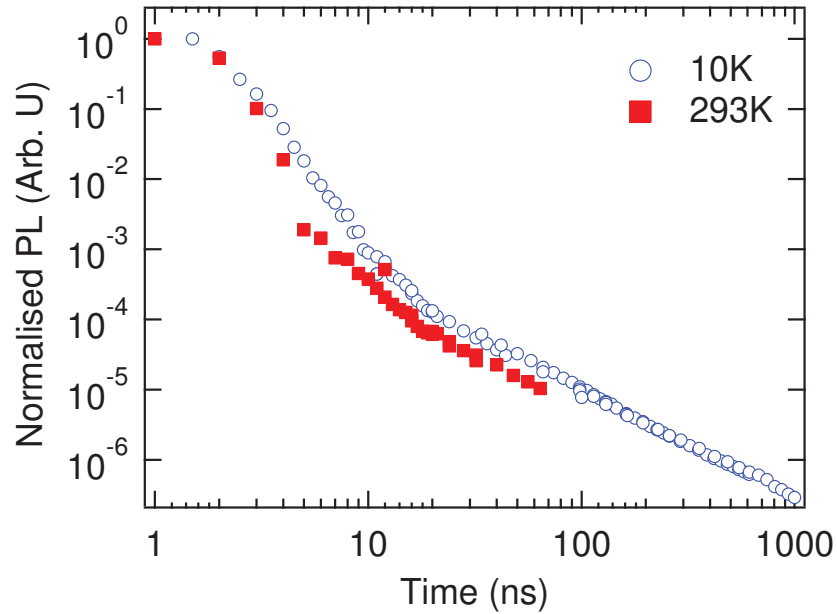


Figure II.3 – Time-resolved PL intensity following 2.33-eV photoexcitation at two temperatures indicated in the legend.

### II.2.3 Delayed PL spectral bandshape

Fig. II.4 displays two time-resolved PL spectra shown in Fig. 2(a) of the main article. In order to demonstrate that the spectra at 10 ns and longer times is a superposition of the aggregate spectrum (still evident after 4 ns) and a broad, less featured component, we have subtracted the 10-ns spectrum, normalized arbitrarily, from the 4-ns spectrum. The arbitrary normalization was chosen such that the vibronic structure of the aggregate is subtracted (note that the residual structure around 1.8 eV is probably due to unequal (0,0) intensity of the two spectra). We base our conjecture that the delayed PL spectrum is a superposition of the spectrum of the H aggregate and a featureless ‘non-aggregate’ component, as discussed in the main article, on this procedure. This emission has not been reported in steady-state or time-resolved PL spectra of P3HT, in any solid-state microstructure. It is a product of delayed charge recombination, and it decays with the same power-law

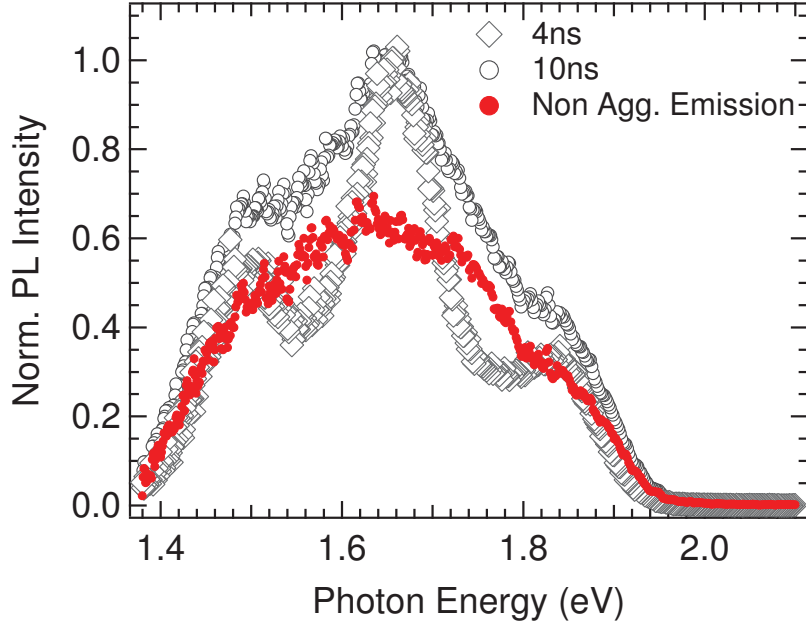


Figure II.4 – PL spectra at two temporal gates, taken from Fig. 2(a) of the main article. The red solid circles are the difference of the spectrum at 10 ns and 0.38 times its peak intensity at 4 ns.

dynamics as the regenerated H-aggregate.

### II.3 Phase-sensitive photomodulation

In order to measure the delayed PL spectrum displayed in Fig. 2(d) of the main article, we have carried out photomodulation PL measurements by continuous-wave photoexcitation implementing phase-sensitive detection with a dual-phase digital lockin amplifier (SRS SR830). Fig. II.5 displays the in-phase ( $X$ ) and  $\pi/2$  out of phase ( $Y$ ) spectra with respect to the modulated 2.33-eV continuous-wave excitation laser. In Fig. 2(d) of the article, we have quantified the PL intensity in quadrature ( $Y$ ) as a fraction of the total intensity  $R = \sqrt{X^2 + Y^2}$ , exciting with the output of a Hg-Xe lamp coupled to a monochromator to select the excitation wavelength, normalized to the fractional signal in quadrature at 2.33-eV excitation

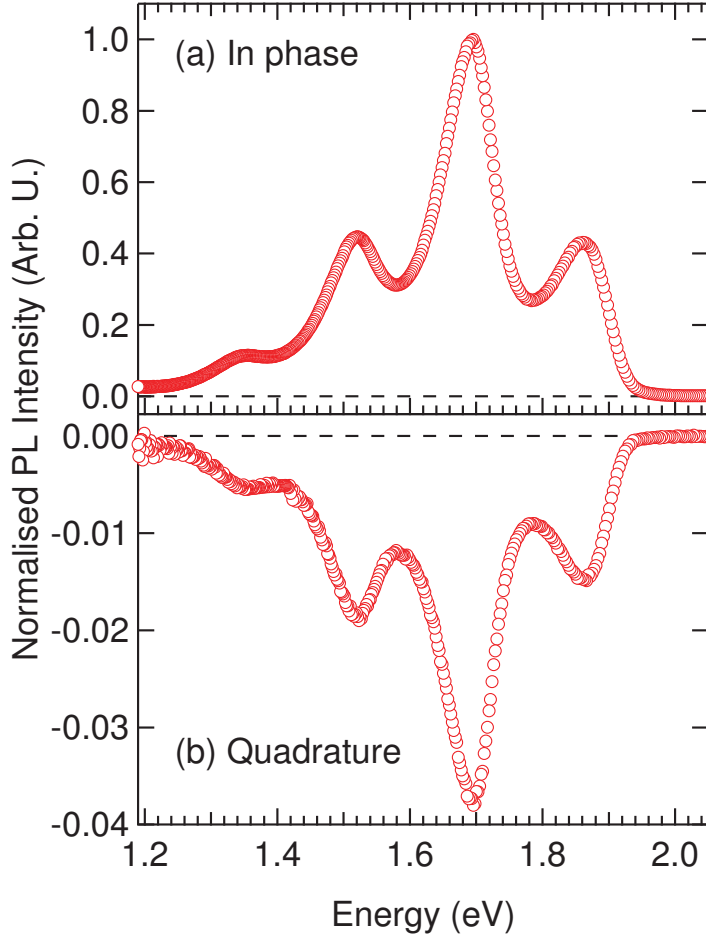


Figure II.5 – PL spectrum measured at 10 K by phase-sensitive detection upon modulated excitation at 2.33 eV. (a) In-phase (X-channel) PL spectrum measured at a modulation frequency of 50 Hz. (b) Corresponding PL spectrum measured in quadrature (Y-channel). The two spectra have the same normalization (note the large difference in intensity scale).

photon energy. We used a modulation frequency of 100 Hz, achieved with an optical chopper. The phase of the lockin amplifier was set such that all of the scattered excitation light was contained in the in-phase (X) channel. We have normalized the Y-channel fractional spectrally-integrated intensity to the value measured at 2.33 eV in Fig. 2(d) of the main article.

## II.4 Transient absorption Dynamics

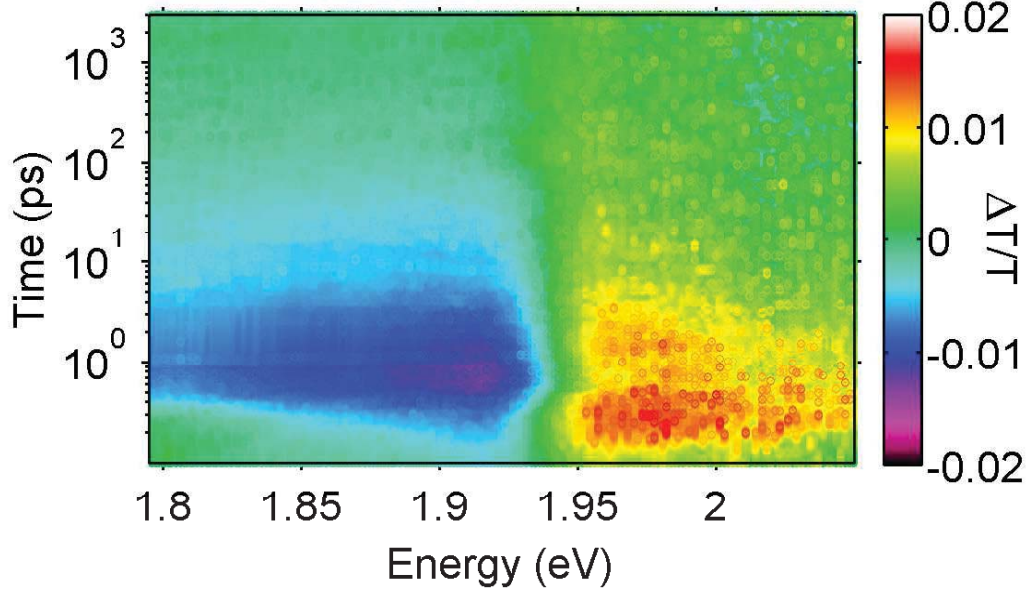


Figure II.6 – (a) Transient absorption spectrum measured at 10 K, with a pump photon energy of 2.33 eV and fluence of  $3.6 \mu\text{J cm}^{-2}$ . (b) Transients at two probe photon energies, indicated in the legend.

We have carried out transient absorption (TA) measurements using the same femtosecond laser pulse train as we used in the time-resolved PL studies, and probing with a single-filament white-light continuum generated with the fundamental of the Ti :sapphire laser (780 nm) in a sapphire window. Fig. II.6(a) displays the TA spectrum. We observe a broad photoinduced absorption to lower energies than 1.93 eV, and a ground-state bleach signal at higher energies. Two absorption transients derived by taking temporal cuts of this spectrum in the photoinduced absorption region are displayed in Fig. II.6(b). Piris et al. assign the photoinduced absorption in this region to a contribution of excitons and polarons [126]. Our TA data demonstrates that polaron absorption is generated promptly after the femtosecond laser pulse, in agreement with Piris et al. and others as described in the main article.

### II.4.1 Comparison of TA and PL dynamics

In order to compare the dynamics probed by TA and time-resolved PL, we display the spectrally-integrated PL dynamics at lower fluence in Fig. II.2(a) with the photoinduced dynamics at 1.88 eV probe photon energy in Fig. II.6(b), shown in Fig. II.7. At this probe photon energy, we expect combined signal due to polarons and to excitons, while the PL decay only probes excitons. Fig. II.7 shows that after  $\sim 20$  ps, the decay of the TA and PL data is similar up to  $\sim 500$  ps, after which the TA signal appears to persist for longer times. Differences in the early-time decayed can be partially ascribed to the different time resolution in the two experiments. The PL measurements were carried out with a streak camera with resolution of  $\sim 6$  ps, while the TA measurements have a resolution of  $\sim 100$  fs. Convolution of the PL decay with such a slow instrument response compared to the TA data leads to an apparent suppression of the time-resolved PL decay during the instrument response. In addition, Piris et al. suggested that recombination of polaron pairs at early timescales is a significant decay mechanism [126], which results in a rapid decay in TA that would not be present in PL. We ascribe the slower decay at longer times in TA to longer-lived polarons.

Fig. II.7 demonstrates that excitons probed by time-resolved PL and TA spectroscopies display similar dynamics under similar photoexcitation conditions, which justifies using time-resolved PL spectroscopy as a probe of exciton evolution. Furthermore, the PL spectral bandshape contains intricate details of the local disordered energy landscape, due to the weakly-coupled H-aggregate nature of excitons in P3HT (see ref. 60 for an extensive discussion). We exploit this property of the PL spectrum in the main article.



### Annexe III

#### Influence of microstructure on geminate polaron spatial distribution in semicrystalline polymeric semiconductors.

##### III.1 Continuous-wave photoinduced absorption spectroscopy

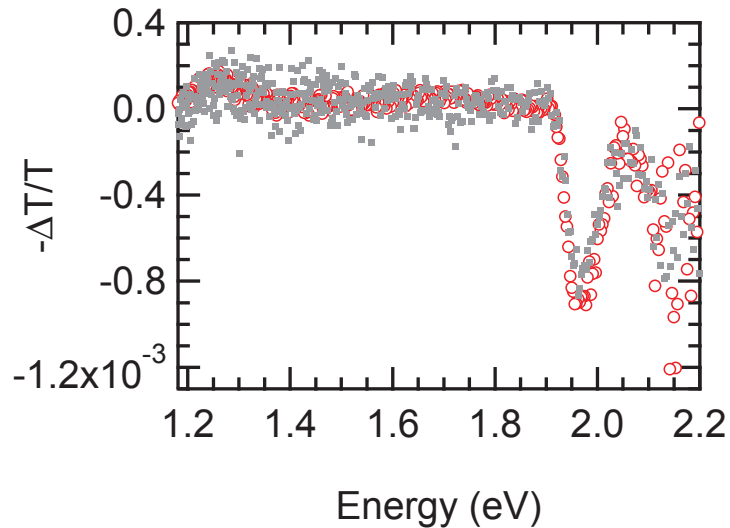


Figure III.1 – (a) Quasi-steady-state photoinduced absorption spectra at  $T=10\text{ K}$  in thin films of neat P3HT on spectrosil substrate (open circles) and ITO substrates (black dots).

In Fig.III.1, we show the cw-PIA spectrum of a thin P3HT film of  $M_w = 48\text{ kg/mol}$  at  $T=10\text{ K}$ , processed on spectrosil and ITO substrates, the latter having a much higher thermal conductivity. We observe no change in the spectral lineshape and yield of photoabsorbing species, ruling out the contribution of a thermal effect to the specific signature of the GSB as was observed in Ref. [185]



## **Annexe IV**

### **Articles publiés ou en attente de publication**

#### **IV.1 Articles publiés**

1. Francis Paquin, Hajime Yamagata, Nicholas J. Hestand, Maciej Sakowicz, Nicolas Bérubé, Michel Côté, Luke X. Reynolds, Saif A. Haque, Natalie Stingelin, Frank C. Spano, and Carlos Silva. Two-Dimensional Spatial coherence of excitons in semicrystalline polymeric semiconductors : Effect of molecular weight. *Phys. Rev. B*, 88 :155202 (2013)
2. Christoph Hellman, Francis Paquin, Neil D. Treat, Annalisa Bruno, Luke X. Reynolds, Saif A. Haque, Paul N. Stavrinou, Carlos Silva, and Natalie Stingelin. Controlling the interaction of light with polymer semiconductors. *Adv. Mater.* 2013, 25, 4906-4911
3. Francis Paquin, Maciej Sakowicz, Natalie Stingelin, and Carlos Silva. Optical signatures of the interplay between intermolecular and intramolecular coupling in plastic semiconductors. *Proc. SPIE* 8459, Physical Chemistry of interfaces and Nanomaterials XI, 845904 (2012).
4. Francis paquin, Gianluca Latini, Maciej Sakowicz, Paul-Ludovic Karsenti, Linjun Wang, David Beljonne, Natalie Stingelin, and Carlos Silva. Charge Separation in Semicrystalline Polymeric Semiconductors by Photoexcitation : Is the Mechanism Intrinsic or Extrinsic ? *Phys. Rev. Lett*, 106 :197401 (2011)

## IV.2 Autres

Les travaux de l'article paru dans Physical Review Letters ont fait l'objet du chapitre 11, intitulé : Electronic Processes at Organic Semiconductor Heterojunctions : The Mechanism of Exciton Dissociation in Semicrystalline Solid-State Microstructure, dans le livre suivant :

5. Wolfgang Brügel (Editor), Chihaya Adachi (Editor), Russell J. Holmes (Consultant). Physics of Organic Semiconductors, 2nd, Completely New Revised Edition. Wiley-VCH. ISBN : 978-3-527-41053-8, December 2012.

## IV.3 Articles soumis ou en préparation

6. Francis Paquin, Paul-Ludovic Karsenti, Natalie Stingelin, and Carlos Silva. Influence of microstructure on geminate polaron spatial distribution in semicrystalline polymeric semiconductors. To be submitted to Journal of Polymer Science B.
7. Francis Paquin, Jonathan Rivnay, Alberto Salleo, Natalie Stingelin, and Carlos Silva. Multi-phase semicrystalline microstructure drive exciton dissociation in neat plastic semiconductors. To be submitted to PNAS.
8. Houssem Kallel, Gianluca Latini, Francis Paquin, Robert Rinfret, Natalie Stingelin, and Carlos Silva. Background-free quasi-steady-state photoinduced absorption spectroscopy by dual optical modulation. Submitted to Rev. Sci. Instrum.